A vertically-integrated approach to climate science: from measurements and machine learning to models and policy

by

Sarvesh Garimella

B.S., California Institute of Technology (2011)
S.M., Massachusetts Institute of Technology (2014)

Submitted to the Department of Earth, Atmospheric and Planetary Sciences
in partial fulfillment of the requirements for the degree of
Doctor of Philosophy in Climate Physics and Chemistry
at the
MASSACHUSETTS INSTITUTE OF TECHNOLOGY
September 2016

Signature redacted

Author .....
Department of Earth, Atmospheric and Planetary Sciences
July 26, 2016

Certified by . Signature redacted .....
Daniel J. Cziczo
Victor P. Starr Associate Professor of Atmospheric Chemistry
Thesis Supervisor

Accepted by . Signature redacted .....
Robert D. van der Hilst
Schlumberger Professor of Earth and Planetary Sciences
Head, Department of Earth, Atmospheric and Planetary Sciences

A vertically-integrated approach to climate science: from measurements and machine learning to models and policy

by

Sarvesh Garimella

Submitted to the Department of Earth, Atmospheric and Planetary Sciences
on July 26, 2016, in partial fulfillment of the
requirements for the degree of
Doctor of Philosophy in Climate Physics and Chemistry

Abstract

The role anthropogenic aerosol particles play in the formation and persistence of ice clouds remains one of the most uncertain aspects of understanding past, present, and future climate. Studying how these particles influence ice cloud formation requires careful measurement of their ice nucleating ability as well as robust uncertainty quantification of experimental results. These measurements and their corresponding uncertainties form the basis for parameterizations used in climate models to probe how anthropogenic particle emissions affect climate through ice cloud formation. This type of investigation can help to inform policy decisions about controls on anthropogenic particle emissions. This study aims to clarify the human role in the climate system by 1) developing instrumentation to perform ice nucleation measurements, 2) quantifying the uncertainty associated with these measurements using machine learning algorithms, 3) incorporating measurements and uncertainty quantification in climate model simulations, and 4) using the modeled climate response to help inform policy decisions for anthropogenic particle emissions.

Thesis Supervisor: Daniel J. Cziczo
Title: Victor P. Starr Associate Professor of Atmospheric Chemistry

Acknowledgments

I would first like to acknowledge my family for all of their love and support over the years, without which I would not have the opportunities I have today. I would like to thank my advisor, Daniel Cziczo, for his guidance throughout my graduate career. Thank you as well to the Cziczo Group and all of the friends I made in Cambridge and at MIT during the past few years. Finally, I would like to say thank you to Dana Mastropole, my best friend and confidant whose thoughtfulness, kindness, and support have helped me immensely along the way.

Contents

List of Tables

List of Figures

Chapter 1

Introduction

1.1 Background

Atmospheric aerosols play an integral role in the climate system because they fundamentally affect clouds, precipitation, and the atmosphere's radiative budget (Pruppacher and Klett, 1997; Seinfeld and Pandis, 2006; Boucher et al., 2013; Stocker et al., 2013). Aerosol particles scatter and absorb atmospheric radiation at both visible (short wave) and infrared (long wave) wavelengths. This direct radiative forcing depends on the optical properties of the particular aerosol and on environmental factors such as the wavelength of incoming radiation, relative humidity, aerosol concentration, spatial distribution, and atmospheric dynamics (Seinfeld and Pandis, 2006). Aerosol particles also influence the formation and persistence of various types of clouds in the atmosphere. Through a process called nucleation, particles provide a surface upon which water can condense or freeze to form clouds in the atmosphere. A particle that has induced water condensation is called a cloud condensation nucleus (CCN), and one that has induced freezing is called an ice nucleating particle (INP). CCN and INP impacts on climate are a strong function of their microphysical properties in clouds: because an aerosol particle's effectiveness as a CCN or as an INP directly influences the formation, persistence, and radiative properties of clouds, it is important to characterize the conditions under which it can nucleate water or ice. Overall, an aerosol particle's nucleation efficiency depends on physical properties like size, chemical com-

position, and mixing state, and on the ambient environment (Pruppacher and Klett, 1997; Dusek et al., 2006; Seinfeld and Pandis, 2006; Petters and Kreidenweis, 2007; Hoose and Möhler 2012).

According to the Intergovernmental Panel on Climate Change 5th Assessment Report (IPCC AR5), the level of confidence for understanding cloud responses due to aerosols remains low (Stocker et al., 2013). As seen in Figure B-1 this lack of understanding is the most significant contributor of uncertainty for radiative forcing in the climate system. In particular, the glaciation and thermodynamic cloud effects (described below), which pertain in particular to the formation and persistence of ice and mixed-phase clouds in the atmosphere, remain among the most uncertain (Boucher et al., 2013).

Increasing the number of INP in a supercooled liquid water cloud causes it to glaciate very rapidly due to the difference in the vapor pressures over ice and water. Unlike the supercooled droplets they replaced, the ice crystals are growing in an environment that is highly supersaturated with respect to ice, via what is called the Bergeron-Wegner-Findeisen process (Pruppacher and Klett, 1997). Therefore, they can reach the critical size required for them to precipitate. This phenomenon is referred to as the cloud glaciation effect and can effectively convert a non-precipitating cloud into a precipitating cloud due to increased INP concentrations (Boucher et al., 2013). However, with higher particle concentrations, supercooled liquid clouds can exist at colder temperatures: since a given amount of water is spread among more numerous (but smaller) droplets and since nucleation rates scale with droplet volume, the decreased droplet sizes can lead to delayed cloud glaciation (Pruppacher and Klett, 1997). It remains uncertain whether increasing the number of INP in ice and mixed-phase clouds would increase or decrease precipitation because of these competing effects.

In addition, more particles in a mixed-phase cloud may instead cause cloud water to be spread among more droplets or ice crystals, and the resulting decrease in hydrometeor size would tend to decrease precipitation. However, since smaller droplets would convectively rise and freeze at higher altitude, this effect could also lead to

increased latent heat release and result in more vigorous convection and more precipitation. The magnitudes of these effects and the resulting radiative forcing due to these cloud responses remain uncertain (Boucher et al., 2013).

Cirrus clouds, which contain only the ice phase, also exhibit a complex dependence of cloud properties on INP concentrations. In these clouds, the sensitivity to INP concentration exhibits a nonlinearity due to a transition from the homogeneous (unaided by INP) to heterogeneous (facilitated by INP) nucleation regimes (see below). Therefore, the responses due to aerosols for these clouds also contribute to the significant uncertainty in understanding cloud radiative forcing (Boucher et al., 2013; Storelvmo et al., 2013).

Overall, the cold cloud responses to aerosols are among the most challenging cloud effects to measure. Some of this difficulty arises because cold clouds occur either high in the atmosphere or near the poles and are very difficult to access. However, since cold clouds cover between 1/3 and 1/2 of Earth's surface area at a given time, they are a very important factor in understanding the Earth's climate system (Lynch et al., 2002). Adding to this difficulty, prediction of ice formation is challenging since it occurs via several known processes (Pruppacher and Klett, 1997). Depending on the specific process involved in nucleating ice on a given particle under given conditions, different model parameterizations of ice formation give vastly different results for cloud particle concentrations (Eidhammer et al., 2009; Storelvmo et al., 2011; Gettelman et al., 2012). Overall, without further study of the conditions required for ice nucleation by different pathways in various regimes, it will remain difficult to model aerosol-cloud interactions and clarify their role in the climate system.

1.2 State of the field

There are several known mechanisms by which aerosols form ice crystals. Homogenous freezing can occur at the coldest temperatures, where aqueous droplets spontaneously freeze in the atmosphere to form ice crystals. Empirical observations have demonstrated that homogenous freezing does not occur above $-38°C$ (Pruppacher

and Klett, 1997; Koop et al., 2000). Above this temperature, an INP is required for ice formation to occur. The most common mechanisms by which INP-assisted ice formation occurs are depicted in Figure B-2. 1) Deposition nucleation occurs when an INP and water vapor are present below 0°C and the environment is supersaturated with respect to ice; in this mode of nucleation, the vapor directly adheres to the INP and begins growing an ice crystal. 2) Condensation freezing occurs when an aerosol particle acts as a CCN at supercooled conditions and forms a droplet that freezes during the process of condensing. 3) Immersion freezing occurs when an INP acts as a CCN to form a droplet that subsequently freezes at a temperature below 0°C. 4) Contact nucleation occurs when an INP collides with a supercooled droplet, which then immediately begins to freeze. Different types of aerosols initiate freezing in different ways and can therefore be classified accordingly (Pruppacher and Klett, 1997; Hoose and Möhler, 2012).

Field studies have indicated that INP are relatively rare in the free troposphere, with an abundance of $\sim$ 10 L^{-1} at temperatures above -40°C (e.g. DeMott et al., 2003a; DeMott et al., 2010; Ebert et al., 2011; Cziczo et al., 2013a). Historical studies of INP show that most are lithogenic and insoluble, but more recently, sea salt, heavy metals, sulfates, organics, and various other particle types have been found to nucleate ice in the atmosphere (DeMott et al., 2003; Cziczo et al., 2009b; Knopf et al., 2010; Cziczo et al., 2013a; Knopf et al., 2014). The conditions required for ice formation have been determined in laboratory studies for many representative upper tropospheric aerosol types, including mineral dust. The size and type of mineral influence the ice nucleation conditions (Archuleta et al., 2005; Gallavardin et al., 2008; Welti et al., 2009; Hoose and Möhler, 2012). Overall, mineral material has been measured as an effective ice nucleus, with deposition nucleation occurring at ice saturation ratios of $1.1-1.3$ at temperatures below -25°C (Möhler et al., 2006; Welti et al., 2009; Hoose and Möhler, 2012).

Ice nucleation experiments have utilized many different techniques (Hoose and Möhler, 2012), including flow tubes to grow droplets (e.g. Cziczo and Abbatt, 1999; Prenni et al., 2001; Hung et al., 2002; Hung et al., 2003), optical and electron mi-

croscopy to characterize field samples (e.g. Zimmerman et al., 2007; Zimmerman et al., 2008; Knopf et al., 2010; Wang et al., 2012; Knopf et al., 2014), differential scanning calorimetry to measure freezing points (e.g. Zobrist et al., 2006; Ahern et al., 2007; Koop and Zobrist, 2009), and large chambers to study nucleation at larger length scales and longer time scales (e.g. Möhler et al., 2006; Crawford et al., 2011; Kanji et al., 2011; Cziczo et al., 2013b; Amato et al., 2015). There are several significant results from these and other experimental studies. For example, variations exist in the $-38°C$ homogenous freezing level. Organic-rich aerosols may not to freeze at all, since their nucleation is delayed due to the particles' atypical viscosity and water uptake at lower temperatures (e.g. Kärcher et al., 2005; Murray et al., 2008; Prenni et al., 2009). Also, the coating state of particles significantly affect their ability to nucleate ice: sulfates and organics that coat even an excellent INP significantly reduce its ability to nucleate ice (e.g. Zuberi et al., 2002; Zobrist et al., 2008; Cziczo et al., 2009a; Chernoff and Bertram, 2010). Each of these ice nucleation measurement techniques has its particular advantages and disadvantages. For example, the larger cloud chambers can investigate cloud-scale processes but are not suitable for field measurements, and offline techniques allow for more flexible field data collection but may not replicate atmospheric conditions. Portable cloud chambers offer a means to bridge the gap between these two types of techniques but such measurements can be difficult to make.

An area of interest in the field of ice nucleation has been examining the role of black carbon (BC) as an INP. Multiple laboratory studies of BC have occurred because of is its presence in the upper troposphere as commercial airplane exhaust and its potential contribution to the climatic effect of contrails (e.g. Kärcher et al., 2007; Demirdjian et al., 2009; Koehler et al., 2009; Crawford et al., 2011; Tishkova et al., 2011; Boucher et al., 2013). Much of this work shows that BC does not significantly enhance ice nucleation (e.g. Möhler et al., 2005; Dymarska et al., 2006; Tishkova et al., 2011). Also, despite the significant release of BC in the upper troposphere, observations suggest that it is not an important INP because it is not abundant as ice residuals in cirrus clouds or contrails (Chen et al., 2000; Froyd et al., 2010; Cziczo et al., 2013a).

Overall, both field and laboratory studies indicate that mineral-rich and metal-rich particles, not BC, are the most important type of particle serving as INP, especially at colder temperatures (Cziczo et al., 2009b; Hoose and Möhler, 2012; Cziczo et al., 2013a). However, sources of BC that emit mineral-rich and metal-rich particles could play a major (and hitherto poorly characterized) role in the climate system via serving as INP. Since such particles are likely to be anthropogenic in origin (Reff et al., 2009), they may play an important role in how humans are modifying the climate system. Fly ash particles, the unburnt refractory residuals from coal combustion, may fall into this category of particle: a significant fraction of BC emissions from coal combustion exhibit mineral and metallic compositions (Davison et al., 1974; Block et al., 1976; Damle et al., 1981) and have been observed to nucleate ice in the immersion mode (Umo et al., 2015).

Cziczo et al. (2009b) show that particles laden with anthropogenic lead nucleate ice efficiently and may have offset a significant amount of warming associated with greenhouse gases. Though the long wave cloud forcing from cirrus clouds tends to exert a net warming effect, shifting ice nucleation to lower altitudes with the higher abundance of lead-bearing particles is reported to be responsible for this cooling offset (Cziczo et al., 2009b). Also, Cziczo et al. (2013a) highlight that mineral and metallic particles are important in ice nucleation. Therefore, since particles containing heavy metals are likely to have anthropogenic origins (Reff et al., 2009; Cziczo et al. 2009b), are known to act as efficient INP (Cziczo et al. 2009b; Umo et al., 2015), and are observed to be present in atmospheric ice clouds (Froyd et al., 2010; Cziczo et al., 2013a), it is important to consider their effects on cloud formation and ultimately the climate system.

1.3 Research motivation

Despite the significant amount of work to understand the role of INP in the climate system, there remain many uncertain aspects of ice nucleation that make it difficult for climate models to effectively simulate cloud responses to aerosols (Stocker et al.,

2013). Various studies have constructed model parameterizations to study the effect of aerosols on cloud formation in a computationally feasible manner (Meyers et al., 1992, Liu and Penner, 2005; DeMott et al., 2010; Niemand et al., 2012, DeMott et al., 2015). The earlier studies attempted to use only humidity to determine INP concentrations, but more recent parameterizations have also used particle size, composition, and ambient temperature. However, such treatments often do not capture the full variability in INP and cloud particle concentrations (Eidhammer et al., 2009, DeMott et al., 2010; DeMott et al., 2015).

In order to make more reliable model parameterizations, variability in nucleation conditions and mechanisms requires more careful study. Laboratory work is required to constrain nucleation conditions of INP and the dependence on freezing mechanisms. Also, further field observations are required, especially outside of the US and Europe, to constrain global INP concentrations and chemistry. A continuous flow diffusion chamber (CFDC) instrument is well suited for this kind of work because it controls aerosol temperature and supersaturation conditions and can measure ice nucleation in both the laboratory and field (Rogers et al., 1988; DeMott et al., 2003; Stetzer et al., 2008). Using this kind of instrument, it is possible to examine how nucleation conditions depend on thermodynamic conditions and particle properties. These measurements can then be used in parameterizations that better constrain the uncertainty of the role of INP in the climate system.

This high level of uncertainty in the field of ice nucleation motivates careful uncertainty quantification, especially as errors propagate from observations and measurements into model estimates of the role of INP in climate. Machine learning algorithms and other statistical techniques therefore provide a useful way to constrain how these uncertainties affect the laboratory measurements, field observations, and model results. Such techniques provide a way to process a large amount of data with many variables and provide insight into the relative importance of these variables. They also allow for fewer assumptions to be made about data and more flexible experimental methodology, since they readily endogenize multiple sources of uncertainty. Overall, combining CFDC-type measurements with robust uncertainty quantification

with machine learning will allow for better representation of measurements in climate models and provide the tools required to clarify the role of natural and anthropogenic INP in the climate system.

Anthropogenic particles are generated from a variety of sources and exhibit large variability in their physical and chemical makeup (Reff et al., 2009), so it is useful to focus on ones that are rich in heavy metals and have the potential to nucleate clouds in the atmosphere. To this end, fly ash particles released from coal combustion are of particular interest. Despite removal from smoke stacks using electrostatic precipitators (Lee et al., 1999), these particles are released in excess of 1000-10000 tons per year from the US alone (Reff et al., 2009). They contain significant amounts of trace elements such as lead, barium, chromium, strontium, arsenic, and zinc that are found to increase dramatically in abundance with decreasing particle size (Davison et al., 1974; Smith et al. 1979). However, their effects on climate have yet to be quantified despite significant emissions and compositional potential for forming clouds. Therefore, understanding the role fly ash plays in the climate system requires laboratory experiments that measure its ability to interact with water and subsequent modeling efforts to understand how this behavior can affect the climate.

1.4 This study

This dissertation presents recent efforts to clarify the role of anthropogenic INP emissions in the climate system. It first discusses the SPectrometer for Ice Nuclei (SPIN), a new commercially-available INP counter, which is intended to lower the entry barrier for making ice nucleation measurements, that was developed as a part of this thesis research (Chapter 2). The introduction of SPIN as a commercially available ice chamber facilitates ice nucleation measurements to be made with higher temporal and spatial coverage, because it will allow many more research groups to perform online ice nucleation measurements. Next, this dissertation presents a novel implementation of uncertainty quantification methodology for ice nucleation measurements that captures biases in past field observations with CFDC-style instruments and prop-

agates these biases into a global climate model (Chapter 3). It then shows for the first time how these experimental, data analysis, and modeling techniques can be used to understand how fly ash particles released from coal combustion affect the climate system via nucleating ice clouds (Chapter 4). It concludes by discussing the policy implications of these climate effects in the context of the recent Paris Agreement (Chapter 4) and by motivating future work to improve the understanding of anthropogenic INP and climate (Chapter 5).

Chapter 2

The SPectrometer for Ice Nuclei (SPIN): An instrument to investigate ice nucleation

This chapter is adapted from a journal article with the same title that has been accepted for publication in Atmospheric Measurement Techniques.

Abstract

The SPectrometer for Ice Nuclei (SPIN) is the first commercially available ice nucleating particle (INP) counter. Arising from a partnership between researchers at the Massachusetts Institute of Technology and engineers at Droplet Measurement Technologies, SPIN is a continuous flow diffusion chamber with parallel plate geometry based on the Zurich Ice Nucleation Chamber and the Portable Ice Nucleation Chamber. This study presents a standard description for using the SPIN instrument and also highlights methods to analyze measurements in more advanced ways. It characterizes and describes the behavior of the SPIN chamber, reports data from laboratory measurements, and quantifies uncertainties associated with the measurements. Experiments with ammonium sulfate are used to investigate homogeneous freezing of deliquesced haze droplets and droplet breakthrough. Experiments with kaolinite, NX

illite, and silver iodide are used to investigate heterogeneous ice nucleation. SPIN nucleation results are compared to those from the literature. Also presented is a machine learning approach for analyzing depolarization data from the SPIN Optical Particle Counter. Overall, we report that the SPIN is able to reproduce previous INP counter measurements. In addition, the introduction of a commercially available INP counter lowers the barrier for entry into making online ice nucleating measurements, which will facilitate the proliferation of ice nucleation research.

2.1 Introduction

Aerosol particles facilitate the nucleation of cloud droplets and ice crystals in Earth's atmosphere (Pruppacher and Klett, 1997). Ice nucleating particles (INP) enable the formation of ice crystals via several possible mechanisms, including deposition nucleation, immersion freezing, and contact freezing (Rogers, 1989; Pruppacher and Klett, 1997). Droplets freeze homogeneously below temperatures of $\sim -38°C$, including deliquesced haze droplets which do so below water saturation at such cold temperatures (Koop et al., 2000). Because of the complexity of the ice nucleation process, understanding INP interactions with water has been difficult (Hoose and Möhler, 2012; Boucher et al., 2013; Stocker et al., 2013). Despite this difficulty, the significant influence that mixed-phase clouds and ice clouds have on the Earth's radiative budget and hydrologic cycle makes understanding the microphysics of cloud formation an important step in quantifying their influence on climate (e.g. Storelvmo et al., 2011; Hoose and Möhler, 2012; Tao et al., 2012; Gettelman et al., 2013).

Laboratory measurements allow for the investigation of ice nucleation at specific conditions with controlled aerosol properties and provide insight into ice formation as it occurs in the atmosphere. Several types of instruments have been developed to measure the efficiency of heterogeneous nucleation of cloud droplets and ice crystals. Many of these have applicability for measurements in the laboratory, as well as intended application for field observations. Among these instruments, the Continuous Flow Diffusion Chamber (CFDC) (Rogers, 1988) has proven a useful tool to mea-

sure the conditions required to nucleate ice crystals on various INPs. Studies have been conducted on different nucleation and freezing mechanisms using many types of aerosol particles under a wide range of temperatures and relative humidities (RHs) (Rogers, 1988; Salam et al., 2006; Stetzer et al., 2008). Improved versions of the original cylindrical chamber described by Rogers (1988) have been successfully deployed in ground and aircraft based field campaigns (Chen et al., 1998; DeMott et al., 2003a; DeMott et al., 2003b). One contemporary (parallel plate) design is the Zurich Ice Nucleation Chamber (ZINC) (Stetzer et al., 2008), which has been used for several laboratory studies (e.g., Welti et al., 2009; Welti et al., 2014). The Portable Ice Nucleation Chamber (PINC), designed as a field-deployable version of the ZINC, has since been used to conduct several laboratory and field studies (Chou et al., 2011; Chou et al., 2013; Kanji et al., 2013). In addition, other research groups have also developed similar chambers (Kanji et al., 2009; Kulkarni et al., 2009; Friedman et al., 2011; Jones et al. 2011; Saito et al., 2011). Adapting the parallel plate design and other features from the ZINC and PINC chambers, the SPectrometer for Ice Nuclei (SPIN) is a commercially available ice nuclei counter manufactured by Droplet Measurement Technologies (DMT) in Boulder, CO. This study characterizes the behavior of the SPIN chamber and reports data that characterize the general instrument design and performance.

2.2 Instrument theory and design

2.2.1 Operating principles

CFDCs, such as the SPIN, are used for ice nucleation measurements by exposing aerosol particles to controlled temperature and RH conditions. The chamber walls (which are parallel plates in the SPIN chamber) are coated with a thin layer of ice ($\sim$1 mm thickness in the SPIN chamber, as inferred from the volume depleted from the water reservoir after icing). The water vapor partial pressure directly adjacent to the ice wall is the saturation vapor pressure over ice at the given ice wall temper-

ature. A laminar air stream flows between the plates, and if the plate temperatures are different, water vapor and heat diffuse from the warmer to the colder wall. This idealized setup leads to linear profiles of water vapor partial pressure and temperature between the two walls. The exponential dependence of saturation vapor pressure on temperature, according to the Clausius-Clapeyron relation, leads to supersaturated conditions with respect to ice between the two walls, with a maximum close to the position of the aerosol lamina (Rogers, 1988; Stetzer et al., 2008). Aerosol particles are constrained within this lamina and surrounded by two sheath flows passed along each wall. This restricts the aerosol to a narrow range of temperature and supersaturation at which ice nucleation can take place. An example of the chamber flow and thermodynamic profile is shown in Figure B-3.

A sufficient temperature gradient between the walls results in the water vapor partial pressure in the aerosol lamina exceeding the saturation vapor pressure over liquid water. In this case droplets, in addition to ice, can nucleate on the aerosol particles. Though droplets can be identified using a depolarization optical particle counter (OPC) (such as the SPIN detector described in Section 2.2.2), increasing the size difference between droplets and ice helps in distinguishing the two phases. To accomplish this, CFDC chambers employ an evaporation section after the main chamber (Figure B-4) to shrink or eliminate droplets while retaining ice crystals. The ice walls in the evaporation section of the chamber are isothermal so the water vapor partial pressure is equal to the saturation vapor pressure over ice. Droplets are therefore unstable and shrink in a manner akin to the Bergeron-Wegner-Findeisen process (Rogers, 1988; Pruppacher and Klett, 1997). Depending on their residence time in the evaporation section, droplets over a critical size will not evaporate completely and are large enough to be detected by the OPC. The main chamber conditions that generate droplets over this critical size are termed droplet breakthrough. These conditions are quantified for the SPIN chamber in experiments described in Section 2.2.4 and represent an upper RH limit for ice nucleation experiments if droplets and ice crystals are indistinguishable.

2.2.2 SPIN chamber design

Figure B-5 shows a diagram of the SPIN system, illustrating the refrigeration, air flow control, and water flow control components. The temperatures of the two chamber walls and the evaporation section are controlled using compressor-driven refrigeration systems and heater strips affixed to the walls. The warm wall and evaporation section are cooled using a single-stage (with R404A refrigerant) refrigeration loop, while the cold wall is cooled using a two-stage (with R404A first stage refrigerant and R508B second stage refrigerant) refrigeration loop. Ten solenoid valves (four for the warm wall, four for the cold wall, and two for the evaporation section) with proportional-integral-derivative (PID) control are used to regulate refrigeration. Thirty 30 W heater strips (twelve on the warm wall, twelve on the cold wall, and six on the evaporation section) are used to minimize deviations of temperature from the set point by applying heating via twenty-six independent PID controllers (twelve for each of the warm and cold walls and two for the evaporation section). T-type thermocouples that are inserted into the walls and affixed with thermal epoxy are positioned at sixteen locations on each chamber wall and two locations on the evaporation section to map variability in temperature (Figure B-4). The chamber itself is machined from aluminum components, with the inner chamber walls sandblasted for wettability, and junctions are sealed with rubber gaskets. The plate-to-plate distance in the un-iced chamber is 1 cm, which is reduced on average to $\sim$8 mm with the ice layer. Qualitative inspection with an endoscope camera indicates that the ice layer is thicker towards the bottom of the chamber and thinner towards the top. The ratio of the main chamber length to the evaporation section length is 4:1.

A hepa-filtered and dried (using molecular sieve desiccant) sheath flow along each wall is circulated through the chamber using a pump and mass flow controller (MFC). Sample air is drawn into the system by an additional pump. The incoming sample air is drawn into the sheath flow using a knife-edge inlet similar to the one used in the ZINC (Stetzer et al., 2008), which splits the sheath into two flows that move along each wall. The knife-edge also focuses the particle flow to the center of the chamber,

which in laminar flow conditions, limit the temperature and supersaturation range experienced by the particles. Figure B-4 shows the dimensions of the main chamber and evaporation section.

After passing through the main chamber and evaporation section, the air stream flows through a linear depolarization OPC that uses four optical detectors for counting, sizing, and differentiating unactivated aerosol particles, droplets, and ice crystals in the 0.4 - 15 μm size range. Figure B-6 shows the optical diagram of the OPC. The side scatter detector is used for particle sizing by total scattering intensity, and the backscatter detectors are used to measure P (parallel to the incident laser light) and S (perpendicular to the incident laser light) polarization for phase discrimination: ice crystals depolarize more light than water droplets because of anisotropy of ice compared to liquid water (e.g. Wettlaufer et al., 1999; Thomson et al., 2009), and this change in depolarization signal is used to differentiate the two phases (Liou and Lahore, 1974; Nicolet et al., 2010; Clauss et al., 2013; Nichman et al., 2016). The OPC laser (Osela ILS-640-250-FTH-1.5MM-100uM) is a continuous wave 500 mW 670 nm laser with a top-hat beam profile. One of two sets of backscatter optics has a polarizing beam splitter and measures backscattered light in both P and S polarizations (P1 and S1, respectively). The second set of backscatter optics measures only the P polarization (P2). The detection angle of both sets of backscatter optics is centered at 135° and has a half angle of 20°.

LabVIEW software is used for instrument control and data acquisition. The SPIN software program consists of several different loops and sub-programs and allows for significant automation during operation. User control of the various SPIN components, including the compressors, valves, and detector is also performed and automated through the LabVIEW interface. Individual actions, such as toggling valves, as well as sequences, such as icing the chamber walls, are controllable through software. The software also includes functionality to create custom sequences, allowing for the majority of operations (including system and compressor startup, cooling the chamber, icing the walls, and running the activation experiments described in Section 2.3.1) to be automated for increased experimental reproducibility. High data

load corresponding to large OPC concentrations will cause a drop counting efficiency: for 1 Lpm sample flow, this corresponds to particle counts higher than $\sim$3900 cm^{-3}, above which additional particles are not recorded. In addition to the foreground sequences initiated by the user, background sequences can also be run to monitor instrument performance. With remote access enabled through virtual network computing (VNC) software (separate from the LabVIEW software), much of the chamber operation can be performed remotely. In particular, starting the compressors, cooling the chamber, icing the chamber, switching the chamber inlet and outlet valves, and controlling chamber conditions can be preformed remotely through VNC, but refilling the water reservoir, installing/removing the OPC, and switching other valves must be performed on site.

2.3 Methodology

2.3.1 Experimental methods

Before beginning experiments, the chamber is dried, cooled, and the walls are coated with ice. This is accomplished by first flowing dry nitrogen through the chamber via the sample and sheath flow inlets to remove residual moisture; the flow exiting the chamber outlet is routed through a dew point sensor (Vaisala DMT152 dewpoint transmitter), so the moisture content of the chamber can be directly measured to ensure the dew point is below -40°C. The compressor system is then activated to cool the chamber (both walls of the main chamber and evaporation section) to the icing temperature of -25°C. Before icing, the double distilled deionized 18.2 MΩ Millipore (DDI) water in the reservoir is cooled to $\sim$ 2°C to reduce strain on the refrigeration system during icing and to ensure that the wall temperatures do not exceed 0°C over the course of the icing process. With the water reservoir attached to the two-way water pump, the icing sequence is activated in the software. This sequence controls the filling and emptying of the chamber with DDI water to form the ice layers. The ice dwell counter in the software specifies the amount of time the

chamber is filled with water and is typically set to 5 s. During and after the icing sequence it is critical to prevent moist room air from entering the chamber, which can cause non-uniform ice on the chamber walls via the formation of frost. This is accomplished by flowing dry air or nitrogen through the sample and sheath flow inlets while allowing the excess flow pressure to be released into the room upstream of the chamber inlets. The entire filling sequence typically lasts $\sim$ 5 min. The difference in the volume of water in the reservoir before and after the icing process is used to infer the amount of ice formed, and this difference is typically $\sim$ 1.25 L. After the ice layer has been formed, the dry nitrogen flow through the chamber is continued to ensure that no frost accumulates in the chamber. Subsequent installation of the detector and activation of the sheath pump allows for assessment of background frost counts that may bias the reported INP concentrations. This background concentration (typically between a few counts to several 10s of counts L^{-1}) influences the lower detection limit of INP.

Once the chamber is iced and has a sufficiently low background, it is ready to perform INP activation experiments. This is accomplished in one of two main ways: (1) ramping the wall temperatures to determine the temperature and/or supersaturation dependent ice crystal concentration or (2) keeping the walls at different but constant temperatures to measure the temporal variability of ice crystal concentration at desired temperature and supersaturation conditions. For the former, increasing the temperature gradient between the walls increases the chamber supersaturation, and decreasing the gradient decreases chamber supersaturation. Ramping both wall temperatures allows for temperature scans at the same supersaturation. For experiments in this study, the evaporation section temperature is set to be the same as the average aerosol lamina temperature. Also, in all cases the OPC reports side scatter (sizing) and backscatter (depolarization) spectra to infer size, concentration, and phase of counted particles.

Frost backgrounds are typically higher in the SPIN chamber at higher supersaturations, and the presence of frost in the chamber can lead to data artifacts. Therefore, periodically measuring the background frost counts with no particles in the chamber

(by setting the inlet valve to the filter position for 3-5 minutes) is an important procedure during activation experiments (described below). For converging and diverging wall temperature ramps (with typical ramp rates of dRH/dt at 2% min^{-1}), this check is performed at the beginning and end of each ramp. For constant supersaturation experiments, this check is performed at fixed time intervals, typically twice per hour. Experiments are automatable using sequences in the SPIN software. These sequences automate the periodic background checks as well as controlling the wall temperature set points. The background concentration increases over time as vapor is transferred from the warm wall to the cold wall, leading to irregularities in the ice layers: as a result, the experiment must be ended once it no longer meets the background levels required for the particular experiment. The exact time this occurs depends on the particular operating conditions for an experiment but is typically after 2-5 hours of operation. For example, if a laboratory experiment with 10 INP cm^{-3} were to report activated fractions at the 1% level, it would require a background of no more than 100 counts L^{-1}. If the temperature gradient between the warm and cold walls is large (e.g. larger than $\sim$ 10-15°C, depending on the actual temperatures) the buoyancy of the air adjacent to the warm wall is expected to overcome the mean flow and causes (upward) flow reversal along the warm wall (Rogers, 1988). The dashed line in the top panel of Figure B-7 shows the ice saturation ratio (S_{ice}) above which flow reversal is possible according to the calculations from Rogers (1988), and the bottom panels show two examples of normal and reversed flow profiles. If flow reversal interferes with the aerosol lamina, the chamber behavior may deviate from ideality (Rogers, 1988; Stetzer et al., 2008). Increasing the sheath flow combats flow reversal, but it decreases the residence time of particles in the chamber, which reduces nucleation and crystal growth efficiencies (Rogers, 1988).

2.3.2 Data processing methods

Standard use

The temperature and supersaturation conditions in the chamber are calculated assuming a linear temperature and water vapor partial pressure gradient between the walls. The width and location of the aerosol lamina (and therefore the range of temperatures and supersaturations experienced by the aerosols) is calculated extending the method from Rogers (1988) using the reported values for wall temperatures (at all thermocouple locations), sheath flow rate, and sample flow rate. The thickness of the ice layer where particles nucleate is assumed to be negligible in the calculations, since the nucleation region (at the top of the chamber) has a much thinner ice layer than the chamber average. This approach provides a basis for calculating chamber conditions at each pair of thermocouples (on the warm and cold wall, respectively, at a given location). The flow rates and temperature conditions are used to calculate the velocity profile, and the ratio of the sample flow rate to the total flow rate is used to determine the width of the aerosol lamina (Rogers, 1988; Kulkarni and Kok, 2012). Since a velocity profile calculation is part of this procedure, the fraction of reversed flow is known.

The above calculations provide temperatures and supersaturations as a time series along with the size distributions and depolarization signals measured by the OPC, which provides four values (one from each of the detectors) on a single particle basis. The number of aerosol particles that have activated into ice crystals or droplets in the standard use case is based on a size threshold, typically 3-5 μm, above which only particles that have nucleated into droplets or crystals exist. Droplet breakthrough conditions represent an upper RH limit for the standard use case because nucleated droplets and ice crystals may be indistinguishable based on size alone. Experimentally determined droplet breakthrough thresholds are presented in Section 2.2.4. A condensation particle counter (CPC) is typically used in parallel to SPIN to measure the concentration of particles entering the chamber, so the estimate of the number of ice crystals from above is used to infer activated fractions by dividing the ice crystal

concentration by the total particle concentration entering the chamber.

Advanced use

In the advanced use case, the number of aerosol particles that have activated into ice crystals or droplets is inferred in post-processing from classification of the particle-by-particle (PbP) data in the four-dimensional OPC parameter space via supervised machine learning (ML) (Mohri et al., 2012). This process is described below and illustrated in Figure B-8 for an example freezing experiment. Please note that the ML procedure described in this section is not an out-of-the-box functionality of the SPIN software but rather a method developed by the authors to utilize the instrument in more advanced ways.

CFDC OPC data has historically been analyzed using post-evaporation section particle size as the sole determiner of activation into ice or droplets, since ice crystals grow to be much larger than the seed particles (e.g. Rogers et al., 2001; DeMott et al., 2010; Chou et al., 2011). If particles larger than a certain size are assumed to be ice crystals, then it must either be assumed or imposed that all aerosol particles are smaller than the ice size and that droplets above that size do not survive the evaporation section. In order to meet this constraint, particle impactors are often used to prevent the largest (and potentially most ice active) particles from entering the CFDC (e.g. Rogers et al., 2001; DeMott et al., 2010; DeMott et al., 2015). Also, if the main chamber is supersaturated with respect to water, the aerosol particles may activate into droplets. The evaporation section is designed to avoid counting these droplets in the OPC, but it will cease to evaporate droplets completely above a threshold (temperature-dependent) supersaturation level. This droplet breakthrough threshold typically provides an upper limit for measurable supersaturation, above which droplets must be differentiated from ice crystals, and it marks the upper RH limit for traditional CFDC operation and data analysis. However, the addition of depolarization data and analysis using supervised ML algorithms allow for this size assumption to be relaxed, since all detected particles are classified by phase and the uncertainty associated with this classifi-

cation is quantified (see below). In general, this ML approach provides accurate, reproducible, and uncertainty-quantifying analysis of the OPC data using preexisting MATLAB libraries (http://www.mathworks.com/help/stats/classification.html; http://www.mathworks.com/matlabcentral/fileexchange/41187-fast-kernel-density-estimator--multivariate-). It also requires fewer assumptions to be made about particle classification and allows more flexibility in experimental design.

Supervised ML algorithms for classification are used to assign new data to predetermined classes based on the similarity of the new data to each of these classes (Mohri et al., 2012). The different output classes in the SPIN OPC data are aerosol particles, water droplets, and ice crystals. These classes must have training data that correspond to a known class (Mohri et al., 2012). However, the SPIN OPC data from an activation experiment typically contains mixtures of these classes rather than the pure end members, so choosing the data that correspond to a class is performed statistically. In particular, training data is sampled from a subset of the data that represents the different classes.

In order to inform this sampling, Kernel Density Estimation (KDE) (Rosenblatt, 1956; Parzen, 1962) is used to create probability density functions (PDFs) of the data in various time intervals. Using the KDE approach to sample training data factors in the relative likelihood that a given class of particle (aerosol, droplet, or ice) will appear in an area of the parameter space. This approach takes into account the structure of the underlying PDFs of the training data to incorporate training data uncertainty into estimates of classification uncertainties.

The SPIN OPC reports four intensity count values (size, S1, P1, and P2) in the PbP data, and KDE with automatic bandwidth estimation is used to create a four dimensional Gaussian mixture model (GMM) (McLachlan and Peel, 2000) of the PDFs (one dimension corresponding to each of the intensity count values from the SPIN OPC) in this particle data following the method of Kristan et al. (2011). Figure B-8 shows data from an illite NX freezing experiment at $-40°C$ with ramping supersaturation. Specifically, Figure B-8a shows PbP data from the beginning of the experiment during an aerosol only time interval (time 1, when only aerosol particles

are present in the chamber). It also shows the corresponding KDE: for ease of visualization the 2D GMM-KDE in S1/P1 vs. size parameter space shown in lieu of the full 4D GMM-KDE used in the analysis. Figure B-8b similarly shows data and the GMM-KDE during an aerosol + ice time interval (time 2, at a supersaturation higher than that required for the onset of ice formation where both particles and ice are present). The PDF in Figure B-8a is deconvolved from the one in Figure B-8b and is used to create a residual PDF, which is then used to inform the weighted sampling of data from time 2 to create training data for the ice only output class (corresponding to the region of the parameter space only ice crystals occupy, Figure B-8c). The data corresponding to the aerosol only (Figure B-8a) and ice only (Figure B-8c) classes are then used to train a supervised ML algorithm. In this example, a Gaussian kernel support vector machine (SVM) (Mohri et al., 2012) is used, and classification uncertainties are quantified via 5-fold cross validation of the training data (Figure B-8d). Once trained, the SVM classifies the OPC data from an experiment with a known missed classification percentage (Figure B-8e).

As in the standard use case, a CPC is used in parallel to SPIN to measure the concentration of particles entering the chamber, so the estimate of the number of ice crystals from above is used to infer activated fractions by again dividing the ice crystal concentration by the total particle concentration entering the chamber.

Figure B-9 shows an extension of this approach to discriminate aerosol particles, water droplets and ice crystals using an application of 3-class supervised ML (Mohri et al., 2012). Bootstrap aggregated decision trees (Breiman, 1996) are used for the classification instead of SVM in this case, because this classification algorithm outperforms SVM in terms of classification error in the 3-class case: both algorithms are operationally interchangeable, so the better performing one with respect to classification error was chosen. This example shows a (dry-generated, polydisperse) silver iodide (AgI) activation experiment at $-17°C$ where the chamber RH is increased. Though a 4D parameter space is again used for this classification, Figure B-9a shows only three of the PbP data dimensions along with 2D projections at the axes limits to illustrate the portions of the parameter space occupied by each class. With this

approach, the concentrations (Figure B-9b) and fractions (Figure B-9c) of ice crystals and water droplets along with classification uncertainty is reported as a function of chamber conditions (note that evaporation section reduces droplet fractions, even above the droplet breakthrough point). The time series data are corrected for background frost by quantifying the frost counts that are classified as ice crystals by the algorithm. At the subsaturated RH conditions in Figure B-9c, data with lower error bars that are not greater than zero show activated fractions that are statistically indistinguishable from zero. Overall, with the large datasets (up to thousands of data points per second) generated by the SPIN OPC, particle classification is performed in a reproducible manner with classification accuracies of 95.0-99.9%.

Once similarly large datasets are generated for field measurements in future studies, ML classifiers can be used for distinguishing frost from real ice in the field. Also, the general ML approach can be used for other instruments with size-only data: for example, an SVM that uses size only would find the optimal size (by maximizing the margin between ice and aerosol training data) to distinguish the two classes and quantify the uncertainty associated with choosing this size via cross-validation.

2.4 Results and comparisons to literature

To evaluate the performance of the SPIN OPC, sizing and detection experiments are performed with different sizes of monodisperse spheres. Glass beads, polystyrene latex spheres, and melamine resin spheres are used for the characterizations. The results from these calibrations are shown in Figure B-10, and illustrate how the SPIN OPC sizes particles (Figure B-10a). The sizing behavior follows a power law fit for particle sizing between 0.5 and 11 μm. Smaller particles scatter the laser light less efficiently, and rapidly decreasing detection efficiency with decreasing size is observed for submicrometer particles (Figure B-10b). In the super-micrometer size range (where ice crystals are expected to be present) the counting efficiency is very close to 1.

To evaluate the behavior of the SPIN chamber, several types of freezing experiments are reported. Specifically, 200 nm (nebulized, dried, and mobility selected)

ammonium sulfate (AS) aerosol is used to determine the droplet breakthrough line and to compare the deliquesced haze droplet homogeneous freezing points reported by SPIN to literature values. Also, polydisperse, dry-generated NX illite and AgI (Sigma Aldrich $>$ 99%, with a narrow mobility size distribution between 200-300 nm) particles are used to investigate the heterogeneous ice activation for comparison to literature (note that the purity levels of AgI in previous studies is unknown). The homogeneous freezing results shown in Figure B-11 suggest that the temperatures and supersaturations reported by SPIN are indicative of the real conditions in the chamber. Similarly, the results from the heterogeneous freezing experiments are shown in Figure B-12 and indicate freezing occurs in the expected regions of phase space for the different seed particles.

AS data is used to characterize SPIN's behavior in humid (near or above water saturation) conditions across a wide range of temperatures. AS freezing experiments at colder temperatures compare the chamber performance to the well-characterized homogeneous freezing behavior of deliquesced haze droplets. Though solid AS has been observed to nucleate in the deposition mode (Abbatt et al., 2006), this effect is negligible for the temperatures and activated fractions considered in this study. The data in Figure B-11 show that this behavior is captured in both temperature and RH ramps and occurs in the expected region of phase space. They demonstrate that droplets in SPIN begin to freeze when the chamber temperature falls below $\sim -38°C$ and that homogeneously frozen ice crystals begin to disappear above this temperature. Similarly, the RH ramp data show that supercooled aqueous AS haze droplets freeze at RH levels similar to those predicted by the Koop et al. (2000) line for a homogeneous nucleation rate coefficient $J = 10^{11}$ cm^{-3} s^{-1}. The effects of multiply charged particles is also negligible because the uncertainty contributed by these particles on expected homogenous freezing supersaturation ($\pm \sim 1\%$ RH using the relevant values from Koop et al. (2000)) is smaller than the other measurement uncertainties of these experiments ($\pm \sim 5\%$ RH).

At warmer temperatures, homogeneous freezing does not occur, so AS is used to measure SPIN's droplet breakthrough threshold. Though post processing of the PbP

detector data can distinguish droplets from ice (Section 2.3.2), droplet breakthrough is quantified using AS (which is much more hygroscopic than many INPs) and provides a conservative (lower RH) estimate for where this occurs. The measured droplet breakthrough line indicates that SPIN's evaporation section extends (a few percent above water saturation) the region of phase space where experiments can be performed without needing to differentiate droplets from ice crystals.

AgI, despite not being found in the atmosphere, nucleates very efficiently in the deposition mode across a range of temperatures and provides a benchmark to assess chamber performance (e.g. Detwiler and Vonnegut, 1981; Stetzer et al., 2008). The SPIN results shown in Figure B-12 match literature data across a wide temperature range and demonstrate that SPIN accurately captures ice nucleation at warmer temperatures where there are many atmospherically relevant INP that activate into ice crystals. In addition to AgI results, heterogeneous freezing results for NX illite and kaolinite are also included, because they are commonly used surrogates for atmospheric dust, which is important for ice nucleation at colder temperatures (DeMott et al., 2003b; Welti et al., 2009; Cziczo et al., 2013a). Unlike AgI, NX illite and kaolinite show a strong temperature dependence in freezing behavior and nucleate ice much less efficiently at temperatures warmer than $\sim -35°C$. Previous investigation of these materials has shown this transition (e.g., Welti et al., 2009), and the SPIN data in this study also capture this temperature dependence. Additionally, the coldest illite data points demonstrate that SPIN can access temperatures in the cirrus cloud regime.

Figure B-13 shows SPIN performance during an exemplary ambient measurement taken in Cambridge, MA on April 14th, 2016 with an aerosol temperature of $\sim -30°C$ and water saturation ratio (S_{liq}) of 1.05 (reported lamina temperature was $-30.7°C \pm 0.2°C$ and lamina S_{liq} was 1.05 ± 0.01 over the measurement period). Polydisperse ambient aerosol was sampled through an inline molecular sieve dryer with no upstream impaction. The SPIN sheath flow was provided from a dry nitrogen cylinder (instead of recirculating flow through a dryer) to minimize frost. Assuming a 5 μm threshold for ice yields 13-40 INP L^{-1} in the measurement periods and 3-9 frost counts L^{-1} during the filter periods: the INP concentration adjusted for frost was then 9-36 INP

L^{-1} over the entire measurement period.

2.5 Measurement uncertainty

With a CFDC instrument, there are various sources of uncertainty that influence experimental results (e.g. Rogers, 1988; Stetezer et al., 2008). Uncertainties in wall temperatures, flows, numbers of counted ice crystals, flow reversal, and other deviations from ideality must be considered when interpreting results from a CFDC chamber. In SPIN, wall temperatures are recorded at sixteen locations on each wall. The aerosol lamina temperature and supersaturation conditions are calculated based on the measurements at these locations, providing a way to infer the variations in thermodynamic conditions experienced by the aerosol. Since the three bottommost thermocouples are strongly coupled to the evaporation section and occupy the transition region between the moist main chamber and dry evaporation section, only the top thirteen thermocouples are used for reporting average chamber conditions. Therefore, uncertainty in chamber conditions is reported as the standard deviation of the lamina temperature and RH at these thirteen locations. Variability in the wall temperatures depends on operating conditions (but typically has a standard deviation of 0.5-2°C), and these variations must be included in uncertainty estimates. Along with these temperature gradients, variations in temperature and supersaturation across the width of the aerosol lamina are sources of uncertainty in SPIN measurements. The width of the aerosol lamina itself can be a source of uncertainty (Garimella et al., 2015), and merits investigation in future work. For the purposes of this study, misclassification error from the ML approach is used for reporting uncertainties in ice crystal concentrations and activated fractions.

Computational fluid dynamics (CFD) calculations in this section are used to explore how closely simulated chamber conditions match ideality. Figure B-14 shows results from ANSYS Fluent CFD modeling (Fluent, 2015) of the SPIN chamber. Several simulations were performed and results from two of these are shown. Specifically, the left column in Figure B-14 shows results for nominal lamina temperature of -40°C

and lamina S_{ice} at 1.3, and the right column shows results for nominal lamina temperature of $-30°C$ and lamina S_{ice} at 1.1. Overall, simulated chamber temperature, RH, and flow velocity match the ideal case predicted by Rogers (1988) for these and other Fluent experiments. Flow reversal along the warm wall (Figure B-7) is also observed in high RH simulations, but as with the physical experiments, this effect does not appear to have an appreciable influence on the aerosol lamina conditions beyond that which is predicted by Rogers (1988) model. Since the analytical and CFD models show qualitatively similar flow reversal, this effect is accounted for when reporting chamber conditions with the analytical model. Furthermore, agreement between the homogeneous freezing data and expected homogeneous freezing conditions provides evidence, similar to that shown by Richardson (2009), that this effect does not bias results since these experiments are performed where the largest degree of flow reversal is expected.

2.6 Conclusions

This study outlines the operating principles, chamber design, and experimental results from the SPIN chamber, a commercially available CFDC chamber manufactured by DMT. The results from this study evaluate the SPIN chamber performance using a variety of experimental tests and CFD modeling.

The introduction of SPIN as a commercially available ice chamber is similar to the introduction of the DMT Cloud Condensation Nuclei Counter (Roberts and Nenes, 2005; Lance et al., 2006), potentially allowing these measurements to be made with higher temporal and spatial coverage. In addition, the methodologies highlighted in this study facilitate performing INP measurements with increased experimental flexibility and reproducibility and also with fewer assumptions in the analysis. In particular, the addition of a depolarization detector coupled with supervised ML algorithms for data analysis allows for robust determination of particle phase with uncertainty quantification. These results motivate future work to extend the ML approach to field data analysis and to intercompare the SPIN chamber performance with other

INP counters in the laboratory and in the field. The experiments presented in this study illustrate SPIN's measurements of freezing behavior of both the heterogeneous and homogeneous regimes and demonstrate that the SPIN chamber reproduces freezing data measured in previous studies. The AgI measurements span a wide range of temperatures, extending to regions where the more efficient atmospheric INP would activate into crystals. The NX illite and kaolinite measurements demonstrate that SPIN measures into the heterogeneous freezing portion of the cirrus cloud regime and also captures the temperature dependence of mineral dust ice activity. The AS experiments provide an estimate of the droplet breakthrough level of the SPIN chamber at warmer temperatures, and at colder temperatures shows that homogeneous freezing of deliquesced haze droplets occurs in agreement with previous experiments and theory. By using an uncertainty quantifying OPC analysis technique, recording high spatial resolution temperature measurements along the chamber walls, and investigating the chamber conditions using CFD modeling, the main sources of uncertainty in SPIN measurements have also been studied.

Overall, the SPIN chamber reproduces laboratory data measured by previous CFDC chambers, and the uncertainties in the measurements have been investigated. The commercial availability of such an instrument may allow for increased coverage of INP measurements that will help constrain the influence of ice nucleation on the atmospheric radiation budget and the initiation of precipitation, thereby leading to a better understanding of the impact of ice formation on the Earth's climate and water budget.

Chapter 3

How uncertainty in field measurements of ice nucleating particles influences modeled cloud forcing

Abstract

This study investigates the systematic low bias in field measurements of ice nucleating particles using continuous flow diffusion chambers. Such instruments have been deployed in the field for decades to measure the formation of ice crystals using ambient aerosol populations. These measurements have, in turn, been used to construct parameterizations for use in global climate models by relating the formation of ice crystals to temperature and aerosol particle number. Non-ideal instrument behavior, which exposes particles to lower humidities than reported, has resulted in a systematic underestimation of the number of ice nucleating particles, and variability in this bias affects the model response to these parameterizations. We show that a machine learning approach can be used to minimize this uncertainty. In addition, we find that the simulated long wave cloud forcing in a global climate model simulation can vary up to

0.8 W m^{-2} and can change sign from positive to negative depending on the treatment of this uncertainty. Based on these results, more careful treatment is required at both the experimental and modeling stages of parameterization development in order to account for such biases.

3.1 Introduction

Ice nucleating particles (INPs) play an important role in the climate system by influencing clouds, precipitation, and radiative transfer. Despite their importance, there are significant uncertainties in field measurements of INP concentrations because of the complexities of atmospheric ice nucleation processes (Boucher et al., 2013). Field measurements over the last few decades with Continuous Flow Diffusion Chamber (CFDC) INP counters (e.g DeMott et al., 2003a; DeMott et al., 2003b; Chou et al., 2011; Boose et al., 2016) have been used to constrain INP concentrations in climate models: they have led to various parameterizations of INP concentration (and therefore ice crystal concentration) as a function of temperature and particle concentration (DeMott et al., 2010; Tobo et al, 2013; DeMott et al., 2015). Such parameterizations are used in both weather prediction models (e.g. Fan et al., 2014; Hande et al, 2015) and global climate models (e.g. Storelvmo et al., 2011; Xie et al., 2013; Tan and Storelvmo, 2016), where the results are sensitive to the modeled cloud microphysical processes and thus cloud radiation.

CFDC instruments count INPs by drawing in aerosol particles, controlling the temperature and relative humidity to which they are exposed, and counting the number that activate into ice crystals (Rogers, 1988; Stetzer et al., 2008; Chapter 2). Particles are drawn through an inlet between two sheath flows, so they pass between two ice-coated walls which are held at different temperatures below 0°C (Figure B-15). Water vapor and heat diffuse from the warm wall to the cold wall, such that approximately linear gradients of both quantities exist across the width of the chamber. Because the saturation vapor pressure exhibits nonlinear temperature dependence, the chamber is everywhere supersaturated with respect to ice, with a maximum su-

persaturation near the center of the chamber (Rogers, 1988). With sufficiently large temperature gradients between the walls, the chamber can also be supersaturated with respect to liquid water. In the ideal configuration, the particles occupy only a small fraction of the width of the chamber, termed the aerosol lamina, whose fractional width is taken to be the ratio of the incoming sample flow rate to the total (sample + sheath) flow through the chamber (Rogers, 1988).

Because of non-idealities in their behavior, CFDC instruments exhibit a systematic low bias in number of INP measured due to the spreading of aerosol outside the lamina predicted by the analytical model (DeMott et al., 2015). This spreading effect was first reported by DeMott et al. (2015), despite many decades of such measurements being made with CFDC instruments, but no comprehensive or quantitative analysis of this effect has so far been conducted. However, the introduction of the SPectrometer for Ice Nucleation (SPIN), the first commercially available CFDC chamber (Chapter 2), provides a means to conduct a comprehensive analysis of the spreading effect: because of the automation of instrument operation and large amount of output data to characterize instrument behavior, the SPIN chamber is well suited to explore this artifact. Furthermore, using machine learning algorithms for analysis provides a method to process the large amount of output data and generate statistical inferences to constrain the spreading effect.

This spreading artifact may be related to deviations from laminar flow and non-isokinetic injection as the particles are drawn into the chamber. The rapid change in thermodynamic environment near the chamber inlet (Chapter 2) and possible flow shear may cause turbulent mixing between sheath flow and aerosol lamina. The reported variables that are most correlated with this spreading are discussed in Section 3.2.2. However, the exact mechanisms contributing to this effect are unknown, and this aerosol spreading leads to greater uncertainty than has been previously assumed. In this study, the variability of this bias is examined using the SPIN chamber, and constrained using a machine learning approach informed by experimental results. The effect of this bias on simulated cloud radiative forcing is also investigated using the National Center for Atmospheric Research Community Earth System Model version

1.2.2 with the Community Atmosphere Model version 5.3 (CAM5.3). The model is an updated version of the CAM5.0 model described by Neale et al. (2010), including a newer cloud microphysics scheme (Gettelman et al, 2015), which is coupled with a detailed aerosol model, the multimode, two-moment, mixing-state-resolving Model of Aerosols for Research of Climate (MARC) (Kim et al., 2008; Kim et al., 2014).

3.2 Methodology

3.2.1 Particle timing tests

To measure the degree of particle spreading outside the lamina, a precise 1-second particle pulse is introduced into the SPIN chamber inlet using an automated solenoid valve. As particles spread across the width of the chamber, they traverse its length at different speeds following the velocity profile of the flow at given chamber conditions (DeMott et al., 2015). The arrival of particles is measured at the chamber outlet with a Condensation Particle Counter. A wider particle pulse (in time) measured at the outlet indicates more spreading of the particles (in space) across the width of the chamber, with the fastest particles traveling closer to the center of the chamber. The shape of the arrival pulse is combined with the shape of the calculated velocity profile to infer the distribution of particles across the width of the chamber (Figure B-16).

Particle distributions were measured with 30 pulse measurements at constant conditions (room temperature, constant flow set points) with 100 nm (mobility diameter) ammonium sulfate particles. In addition, to assess the variability in a variety of conditions and with ambient aerosol, this procedure was also repeated across the entire range of accessible thermodynamic conditions to measure the variability in particle spreading with a total of 267 pulse measurements. Ambient aerosol particles sampled at Storm Peak Laboratory in Steamboat Springs, Colorado were used for these experiments in order to capture the variability of particles in an environment similar to one where an INP field measurement campaign would occur.

3.2.2 Machine learning prediction

Random forest regression (RFR) (Breiman, 2001) is used to predict the fraction of particles that remain in the aerosol lamina (f_{lam}). In this application, RFR is similar to a multiple linear regression, except it grows a forest of bootstrap aggregated (bagged) decision trees to fit the data instead of using a linear model. Using this machine learning approach avoids overfitting the data by using bootstrap aggregation (bagging), provides uncertainty quantification for each prediction using the out-of-bag (oob) prediction error, ranks the variables by their importance by comparing oob prediction errors, and does not assume linear relationships between variables (Breiman, 2001). First, a comprehensive RFR is built using all variables reported by the SPIN software, and used to identify the most import predictors for f_{lam}. This subset included wall temperature variability, flows, and thermodynamic variables in the middle-top of the SPIN chamber, where chamber conditions relax to their nominal values (Chapter 2). Since feature importance falls off exponentially, features within the first two e-folding lengths of importance are used in the reduced RFR model.

3.2.3 CAM5-MARC and the RFP method

The effect of CFDC measurement bias on climate-model-simulated cloud radiative forcing is investigated using the CAM5-MARC. By default, MARC utilizes the ice nucleation scheme of Liu and Penner (2005), which includes a parameterization by Meyers et al. (1992) (hereafter mey) to compute the heterogeneous ice nucleation in mixed phase clouds (Het Ice) between $-40°C$ and $0°C$. In this study, the mey parameterization is replaced by various versions of the parameterization by DeMott et al. (2010) (hereafter D10). The base case (hereafter case B) is the D10 parameterization tuned to match satellite observations of long wave cloud forcing from year 2000 from the Clouds and Earth's Radiant Energy Systems - Energy Balanced and Filled (CERES-EBAF) level 3B dataset (Loeb et al., 2009). Also considered are cases with fixed correction factors (cf), as defined by DeMott et al. (2015), with respect to case B of $cf = 0.1$, 3, 4, 5, and 10 (cases 0.1B, 3B, 4B, 5B, and 10B respectively),

and a case with stochastic cfs sampled from the particle timing test results from this study (stoch case). (Note that the fixed $cf = 3$ (case 3B) suggested by DeMott et al. (2015) is one of the cases considered).

Total aerosol indirect effects in the global climate model are diagnosed using the radiative flux perturbation (RFP) method (Haywood et al., 2009; Lohman et al., 2010; Gettelman et al., 2012). The top of atmosphere radiative flux (R) is computed using two six-year simulations, one with present-day (year 2000, hereafter PD) aerosol and precursor emissions and another with pre-industrial (1850, hereafter PI) emissions, and the RFP is then given by $RFP = R_{2000} - R_{1850}$. Both PD and PI runs have the same prescribed greenhouse gas and climatological sea surface temperature derived from the years 1980-2000. The changes in cloud forcing are decomposed into the changes in the short wave cloud radiative forcing ($SWCF$) and long wave cloud radiative forcing ($LWCF$): $dSWCF = SWCF_{2000} - SWCF_{1850}$ and $dLWCF = LWCF_{2000} - LWCF_{1850}$. Additionally, the "clear-sky" diagnostics recommended by Ghan (2013) are used to calculate cloud forcing correcting for the potential bias in "all-sky vs. clear-sky" metrics that neglect the influence of above-cloud absorbing aerosol and below-cloud scattering ones.

Since the only modification between the cases is the parameterization for Het Ice, this approach diagnoses changes in cloud forcing variables as they relate to changes in cloud microphysical variables due to changing the Het Ice parameterization. All other model configuration parameters are set to their default values (Kim et al., 2008; Kim et al., 2014), so differences in results are attributed to how the variability of the low bias in the D10 parameterization affects simulated cloud forcing.

3.3 Results

3.3.1 Timing test and RFR results

Figure B-17 shows the results from the 30 particle timing tests at constant conditions. The fraction of particles that remain in the aerosol lamina, f_{lam} varies significantly

despite constant flow set points, aerosol properties, and temperature. Figure B-18 shows the results from the 267 particle timing test experiments. f_{lam} is plotted against the reported lamina temperature and ice saturation ratio (S_{ice}), which are the actively controlled variables in CFDC chambers, but the data show no correlations with respect to either variable. The mean and standard deviation values of f_{lam} are 0.25 ± 0.14, and the distribution exhibits values that vary between 0.03 and 0.73 depending on the specific conditions. This distribution corresponds to a distribution of cf with a mean of 4 (and $cf = 2.6$ and $cf = 9.5$ at $\pm$ 1 standard deviations). This variability in measurements suggests that the single value of $cf = 3$ reported by DeMott et al. (2015) does not describe the actual variability in f_{lam}, though their value does fall within the measured range in this study. Also, since the differences in lamina temperature and S_{ice} do not explain this variability, more information than the reported chamber thermodynamic conditions is required to reduce uncertainty in estimating f_{lam}.

The reduced RFR described in Section 3.2.2 provides mean values and standard deviations of predicted f_{lam} based on the ensemble of predictions from the trees in the random forest, using the 65 most important SPIN variables. The oob mean squared prediction error for the forest of trees is 0.008. Simply selecting the mean value for f_{lam} from the distribution in Figure B-18, results in a mean squared error for predicting f_{lam} of ~ 0.02, so the RFR approach reduces the uncertainty from this fixed estimate by $\sim 60\%$.

Figure B-19 shows idealized activation curves and illustrates the spreading effect at various f_{lam} values. Given a population of "perfect" immersion mode INP that form ice crystals exactly at water saturation, Figure B-19a shows the activated fractions of such particles as a function of nominal water saturation ratio (S_{liq}). Since only a fraction of particles actually experience the reported humidity level, nominal S_{liq} values larger than 1 are required to activate these "perfect" INP. The insets to the left of Figure B-19 show the distribution of actual S_{liq} experience by particles at a nominal $S_{liq} = 1.05$. Since these distributions span a continuous range of humidities, there is not a clear representative S_{liq} value that could be reported instead. Figure B-19b and

Figure B-19c show activation curves where only 10% of the particles are "perfect" immersion mode INP, and the rest are cloud condensation nuclei (CCN) that survive the droplet evaporation region (Chapter 2) at a values of nominal $S_{liq} > 1.07$. The shape of the idealized activation curve in Figure B-19c resembles that of experimental CFDC activation curves (DeMott et al., 2015) and both exhibit strong dependence of activated fraction on S_{liq} because of the particle spreading effect. Overall, the particle spreading effect also explains why CFDC chambers must operate at unphysically large S_{liq} values to measure concentrations of immersion mode INP and why reported immersion mode INP concentrations are strongly dependent on S_{liq}.

3.3.2 Climate model results

Figure B-20 shows the PD $LWCF$ and $SWCF$ from all of the cases as well as CERES-EBAF satellite observations. The cases with $cf > 1$ match globally-averaged satellite values for PD $LWCF$ more closely than the B or mey cases, but there is large sensitivity of radiative and cloud properties on the version of the parameterization used (Figure B-20; Table A.1). Table A.1 shows globally averaged radiative and cloud properties in PD and PI runs as well as the PD − PI differences in these values. In particular, it shows $LWCF$, $SWCF$, ice water path (IWP), cloud top ice number concentration (INC), cloud-top ice effective radius (REI), and the PD − PI differences in these variables ($dLWCF$, $dSWCF$, $dIWP$, $dINC$, and $dREI$ respectively). PD $LWCF$, IWP, INC, and REI increase as a function of fixed cf, while PD $SWCF$ decreases as a function of fixed cf. For the mey case, PD and PI values are similar to those in the 0.1B and B cases. Different sensitivities to changing cf in the PD cases vs. in the PI cases lead to decreasing $dIWP$, decreasing $dINC$, and increasing $dREI$ with increasing fixed cf. $dLWCF$ is positive in the mey case and cases with smaller fixed cf, but becomes negative at larger cf values. $dSWCF$ increases as a function of fixed cf.

The values for radiative and cloud properties for the stoch case fall within the range of values from the largest fixed cf cases. However, the changes in cloud properties and corresponding responses in radiative properties in the stoch case are significantly

different than those from the 3B and 4B cases, despite all three of these cases having a similar mean values of cf (Table A.1). This difference is also apparent when comparing $dLWCF$ to $dIWP$ (Figure B-21). In particular, the stoch case exhibits more negative $dIWP$ than the 3B and 4B cases and is one of the cases that exhibit a negative $dLWCF$. The differences between the stoch case and the 3B and 4B cases is also apparent in a zonally averaged comparisons of $dINC$, $dIWP$, $dLWCF$, and $dSWCF$ (Figure B-22), especially in the Northern Hemisphere. Overall, these results indicate that the choice of cf dramatically affects the estimated $dLWCF$, which ranges 0.8 W m^{-2} in the considered cases and changes sign from positive to negative in some instances.

3.4 Discussion and conclusions

The results from the previous section indicate that neither the reported thermodynamic conditions nor results from a single timing test capture the variability of f_{lam} in the SPIN chamber. With many such tests, it is possible to map this variability, and using machine learning to utilize information from additional variables reduces uncertainty in estimating how this variability affects reported INP concentrations from CFDC chambers. In addition, this particle spreading effect also explains why CFDC chambers must operate at unphysically large S_{liq} values to measure immersion mode INP and why the reported numbers are strongly dependent on S_{liq}. The laboratory work in this study exploring the extent of spreading variability motivates future work to minimize both this bias and its variability. Such work would explore which operational considerations (such as flow rates, inlet pressure drop, etc.) maximize probability of isokinetic injection of particles into the chamber. This work would also explore how experimental and chamber design influence the spreading effect, drawing comparisons to computational fluid dynamics simulations to complement the RFR statistical modeling.

The climate model results show that $dLWCF$ spans a range of 0.8 W m^{-2} in the considered cases and changes sign from positive to negative in the larger cf cases

(Table A.1; Figure B-21). The PD value for $LWCF$ increases with increasing fixed cf. There is similar behavior in PI $LWCF$ values, but these exhibit more sensitivity to cf than the PD values, resulting in a negative $dLWCF$ in the larger cf cases. This cloud forcing behavior coincides with changes in IWP. Both the PD and PI IWP values increase with increasing fixed cf. The sensitivity of IWP to cf is larger in the PI cases than in the PD cases, resulting in a decreasing $dIWP$ as a function of fixed cf. Overall, the increased sensitivity of cloud ice to the aerosol fields in larger cf cases results in a relatively smaller amount of cloud ice in the PD cases compared to the PI cases for a given cf, which coincides with decreasing $dLWCF$ as a function of increasing fixed cf.

The model results also suggest that there is a significant change in simulated cloud forcing when cf values are drawn from the distribution of measured values instead of being fixed. The cloud forcing response is associated with changes in $dINC$, $dREI$, and $dIWP$. The relationship between cloud property changes and radiative changes is similar to those reported in previous studies (e.g. Cziczo et al., 2009b; Gettelman et al., 2012; Storelvmo et al., 2011; Xie, et al., 2013): in particular, $dINC$ and $dIWP$ are positively correlated with $dLWCF$, but the exact relationship depends on the parameterization used. Furthermore, these results indicate that selecting the mean cf from a measured distribution does not produce the model response in $dINC$ and $dIWP$ and the corresponding changes in $dLWCF$ that is produced from stochastic cfs, suggesting an influence of the tails of the cf distribution on model results.

Given these results, if heterogeneous ice nucleation parameterizations based on CFDC measurements are to be used extensively in the global modeling community, it is critical to account for both (a) for the under-prediction of INP in these observations, and (b) for the variability (especially in the tails of the distribution) of INP measured with this technique. Small changes in these details, as shown here, can lead to divergent estimates of the magnitude of aerosol impact on ice clouds within the same modeling framework. These results also suggest that minimizing the uncertainty in estimates of this bias, e.g. with the machine learning techniques used in this study, is an important step in constructing heterogeneous ice nucleation pa-

rameterizations based on CFDC measurements. Ideally, cfs would be inferred on a measurement-by-measurement basis and included when fitting parameterization constants: the sensitivity of the parameterization constants to uncertainty in the cfs could then also be quantified. Overall, in order to incorporate CFDC measurements in global models as a means of reducing the uncertainty that INP contribute to the climate system, both experimental and modeling efforts must carefully account for the variability in instrument bias and consider the uncertainty associated with it.

Chapter 4

Mitigating additional climate warming from coal combustion

This chapter is intended to satisfy the capstone project requirement for the Certificate in Science, Technology and Policy.

Abstract

This study investigates the impact fly ash particles have on cloud formation and climate. It examines the physical and chemical properties of several types of fly ash particles and the efficiency with which they form cloud droplets and ice crystals in the laboratory. Fly ash particles are found to be moderately hygroscopic and are found to form ice in the deposition mode at temperatures colder than $\sim -30°C$ and in the immersion mode at temperatures colder than $\sim -20°C$. The laboratory results are used to investigate the impacts of fly ash emissions on the properties of cirrus clouds and climate in a global climate model. Single particle mass spectrometry data from aircraft campaigns are used to estimate the abundance of fly ash in the atmosphere and constrain the sensitivity of the cloud forcing response to fly ash emissions. Overall, current levels of fly ash emissions are estimated to contribute $\sim$ 0.1-0.6 W m^{-2} of extra warming through their role in cirrus cloud formation. Based on these results, international transfer of electrostatic precipitator technology can be

priced at $\sim$ 6800 Certified Emission Reduction (CER) credits per ton of fly ash under the Paris Agreement.

4.1 Introduction

4.1.1 Background

Human activities, especially fossil fuel combustion, release large amounts of particulate matter into the atmosphere (Reff et al., 2009; Lamarque et al., 2010; JRC, 2011; Xing et al., 2013). These anthropogenic particles may scatter and absorb incoming solar radiation and provide a surface on which water can condense or freeze to form clouds (Seinfeld and Pandis, 2006). Through their interaction with radiation and water in the atmosphere, these particles alter the atmospheric energy budget and ultimately the climate (Seinfeld and Pandis, 2006). Since the concentrations of these particles are spatially and temporally variable (Lamarque et al., 2010), it is difficult to quantify their role in a changing climate. Overall, the effect of anthropogenic particles on the climate system is highly uncertain, especially via their role in cloud formation (Charlson et al., 1992; Lohmann and Feichter, 2005; Boucher et al., 2013; Stocker et al., 2013).

There are many different types of anthropogenic particles, which are generated from a variety of sources and exhibit large variability in their physical and chemical makeup (Reff et al., 2009). Black carbon (BC) particles are released from incomplete combustion and arise from biomass burning and anthropogenic sources including, domestic/residential combustion, transportation, industry, and energy production (Seinfeld and Pandis, 2006; Lamarque et al., 2010). The energy sector emits $\sim$ 1% of the total BC (Lamarque et al., 2010), but likely a much larger fraction of many heavy metals (Reff et al., 2009).

Particles that contain soluble material or are rich in heavy metals have an increased potential to form clouds in the atmosphere: particles containing soluble material are known to be efficient cloud condensation nuclei (CCN) (e.g. Petters and Kreidenweis,

2007), and particles laden with anthropogenic lead nucleate ice efficiently (Cziczo et al., 2009b). Furthermore, particles containing heavy metals are likely to have anthropogenic origins (Cziczo et al., 2009b; Reff et al., 2009) and are observed to be present in atmospheric ice clouds (Ebert et al., 2011; Cziczo et al., 2013a). Since the dominant mechanism for ice formation in the cirrus regime is likely heterogeneous nucleation (Cziczo et al., 2013a), particles that nucleate ice efficiently at cold temperatures may play a disproportionately large role in the climate system compared to their abundance in the atmosphere.

In particular, fly ash particles released from coal combustion may be particularly important in cloud formation because they are rich in both organics and heavy metals (Davison et al., 1974; Smith et al., 1979; Lee et al., 1999, Reff et al., 2009), their spherical morphology resembles that of observed cirrus ice residuals (Figure B-23), and previous laboratory measurements show that they nucleate ice (Umo et al., 2015). Despite removal from smoke stacks using electrostatic precipitators (ESPs) (Lee et al., 1999), coal particles are released in excess of 1000-10000 tons per year from the US alone (Reff et al., 2009): in the US, they also constitute a large mass fraction of the gallium, selenium, strontium, silver, and barium in PM 2.5 emissions (Figure B-24). Previous laboratory studies indicate that they contain significant amounts of trace elements such as lead, barium, chromium, strontium, arsenic, and zinc that are found to increase in abundance with decreasing particle size (Davison et al., 1974; Smith et al., 1979). In this study, the physical and chemical properties of several types of fly ash particles are investigated, the efficiency with which these particles form cloud droplets and ice crystals is measured in the laboratory, and the effects of fly ash emissions on the climate system via cirrus cloud formation are investigated using a global climate model.

4.1.2 Comparing emissions

Comparing the climate effects of different climate pollutants is difficult due in part to the different lifetimes of species in the atmosphere. CO_2 is relatively permanent on human timescales in the atmosphere compared to the much shorter lifetime of partic-

ulate matter, which is on the order of days to weeks (Seinfeld and Pandis, 2006). A common metric to compare the climate impacts of substances with different lifetimes is the Global Warming Potential (GWP) (Myhre et al., 2013). GWP is defined as the radiative forcing (RF) from an emission pulse of a species integrated over time, relative to an emission of an equal mass of CO_2. In practice, it is approximately equivalent to the integrated RF response for an emission pulse of a species or the equilibrium RF response from sustained emissions, relative to that for CO_2 (Prather, 2002; Peters et al., 2011; Azar and Johansson, 2012; Myhre et al., 2013).

Based on the definitions above, the effect of a mitigation strategy on the climate system can be expressed as the positive RF avoided by implementing the strategy. Using the GWP metric, this avoided RF can be expressed in units of equivalent CO_2 mass, which can be used for pricing of Certified Emissions Reductions (CER) credits (Kyoto Protocol, 1999; Olsen, 2007; Sutter and Parreño, 2007; Wara, 2008; Paris Agreement, 2015). In this framework, pricing the CER credits for a species is directly tied to its GWP and assumes a given price for CO_2 mass. Section 4.5 discusses a policy mechanism to mitigate additional warming from coal combustion based on this GWP framework.

4.2 Methodology

4.2.1 Fly ash samples

The samples investigated in this study are provided by a commercial fly ash vendor, Fly Ash Direct, and are extracted directly from ESPs in four coal-fired power plants in the United States. The two main types of fly ash are class C, which is produced from lignite or sub-bituminous coal, and class F, which is produced from anthracite or bituminous coal (Ahmaruzzaman, 2009). The samples in this study are class C fly ash from the J. Robert Welsh Power Plant in Titus County, Texas (hereafter Welsh C); class C fly ash from the Joppa Generating Station in Joppa, Illinois (hereafter Joppa C); class F fly ash from the Miami Fort Generating Station in Miami Township,

Ohio (hereafter Miami F); and class F fly ash from the Clifty Creek Power Plant in Madison, Indiana (hereafter Clifty F). In all experiments in this study, particles are generated using the dry flask generation method discussed in Garimella et al. (2014). The use of impactors to eliminate larger particles is discussed below.

4.2.2 Particle characteristics

Particle size distributions, measured with respect to mobility diameter and optical diameter are shown in Figure B-25. Scanning Mobility Particle Sizing (SMPS) distributions are measured using a Brechtel Manufacturing Inc. (BMI) Model 2002 Scanning Electrical Mobility System (SEMS), which draws 0.36 Lpm through the flask generator. Optical size distributions are measured using a TSI Model 3330 Optical Particle Sizer (OPS), which draws 1 Lpm through the flask generator. The OPS distributions are shown with and without the upstream 650 nm cut size traditional impactor, which is always used with the SEMS. These size distributions show a peak in concentration in sub-micrometer size range, with a long super-micrometer tail corresponding to larger particles. Along with this tail of larger particles, peaks at larger sizes correspond to aggregates of the smaller-sized particles.

Particle Analysis by Laser Mass Spectrometry (PALMS) (Murphy and Thompson, 1995; Cziczo et al., 2006) is used to characterize the chemical composition of the four types of fly ash particles on a particle-by-particle basis. $\sim$1000 positive and $\sim$1000 negative spectra are collected for each sample to characterize the heterogeneity in particle chemistry. Typical positive and negative mass spectra are shown in Figure B-26. In general, fly ash spectra resemble those of mineral dust or metallic particles and exhibit peaks corresponding to sulfates, phosphates, metals, and metal oxides. In particular, they show barium and lead peaks that are indicative of an anthropogenic source, with barium appearing in 98% of the spectra.

4.2.3 Droplet and ice experiments

The nucleation of cloud droplets on fly ash particles is measured using a Droplet Measurement Technologies (DMT) Model CCN-200 Cloud Condensation Nuclei Counter (CCNC) (Roberts and Nenes, 2005; Lance et al., 2006). The flask-generated particles are mobility size-selected using a BMI Model 2002 Differential Mobility Analyzer (DMA) with its included 650 nm traditional impactor. The resulting monodisperse flow is split with a laminar flow splitter and is drawn into the CCNC and a BMI 1700 Mixing Condensation Particle Counter (MCPC). The total flow through the system is 1.36 Lpm and is provided by the two CCNC columns drawing 0.5 Lpm each and the MCPC drawing 0.36 Lpm. Particle are exposed to supersaturations (SS) from 0.07% to 0.71% with respect to liquid water in the CCNC chambers: chamber A scans over SS = 0.07%, 0.1%, 0.2%, 0.3% and 0.4%, while chamber B scans over SS = 0.71%, 0.7%, 0.6%, 0.5%, and 0.4%. Each SS step lasts for six minutes, and the each of the last three minutes at a given SS is taken as a single data point, providing three measurements per SS. The number of particles activating into droplets is compared to the total number of particles counted by the MCPC to calculate an activated fraction at each SS. The critical SS (where 50% of the particles activate into droplets) is found by fitting a sigmoid curve to the SS-dependent activated fractions. Both chambers simultaneously measure at SS = 0.4% to verify that results are comparable between the chambers.

The formation of ice crystals via deposition nucleation and immersion freezing is measured using a DMT Spectrometer for Ice Nuclei (SPIN) (Chapter 2). The flask-generated particles are either polydisperse (through the 650 nm traditional impactor) or DMA size-selected as with the CCNC experiments. After impaction and/or size selection the particle-laden flow is split with a laminar flow splitter and is drawn into the both the SPIN and MCPC. The total flow through the system is 1.36 Lpm, 1 Lpm drawn by the SPIN chamber and 0.36 Lpm drawn by the MCPC. Particles are exposed to desired temperature (from −42°C to −15°C) and SS (from $S_{ice} = 1.0$ to $S_{ice} = 1.6$) conditions using SS scans at a given temperature. The number of particles activating

into ice crystals is determined in post processing via the machine learning technique described in Chapter 2 and is compared to the total number of particles counted by the MCPC to calculate activated fractions. Filter measurements of particle-free air are collected before and after each SS scan to determine the background frost concentrations, which are subtracted from the calculated ice crystal concentrations.

4.2.4 Observations from aircraft campaigns

Single particle mass spectra collected by the flight PALMS instrument during four aircraft campaigns over North America provide a means to estimate ambient fly ash concentrations. Specifically, data from the Deep Convective Clouds and Chemistry (DC3) field campaign in 2012 (Barth et al., 2015), the Mid-latitude Airborne Cirrus Properties Experiment (MACPEX) in 2011 (Cziczo et al., 2013a), the New England Air Quality Study (NEAQS) in 2004 (Peltier et al., 2007), and the Studies of Emissions, Atmospheric Composition, Clouds and Climate Coupling by Regional Surveys (SEAC4RS) in 2013 (Toon et al., 2016) are used. PALMS spectra of fly ash particles collected in the laboratory are used to create a filter for finding fly ash in field spectra using barium and other chemical markers for fly ash (Zawadowicz et al., 2016). The conditional probabilities of this filter correctly flagging a fly ash particle and incorrectly flagging a non- fly ash particle in the historical PALMS laboratory dataset are then calculated, providing a Bayesian estimate of the concentration of fly ash particles measured in the field campaigns.

4.2.5 Global climate modeling

The radiative responses to fly ash emissions are investigated using the National Center for Atmospheric Research Community Atmosphere Model version 5.3 (CAM5.3). The model is an updated version of the CAM5.0 model described by Neale et al. (2010), including a newer cloud microphysics scheme (Gettelman et al, 2015). This scheme is coupled with a detailed aerosol model called the multimode, two-moment, mixing-state-resolving Model of Aerosols for Research of Climate (MARC) (Kim et al., 2008;

Kim et al., 2014). The CAM5-MARC utilizes the ice nucleation scheme of Liu and Penner (2005) with a stochastic parameterization for the heterogeneous ice nucleation in mixed phase clouds (Chapter 3). Based on the similarity of fly ash sources to BC sources in the model, fly ash concentrations are diagnosed using a tunable scale factor (sf) on BC concentration. The nominal $sf = 1$ derived from the estimate by Lamarque et al. (2010) that 0.7% of global BC emissions are from the energy sector, and cases with $sf = 0$, 0.1, 0.5, 1, 5 10, 50, and 100 (corresponding to multiplicative factors of the 0.7%) are considered. This range of sf is also compared to the aircraft data to constrain the model results (Section 4.3.3).

The laboratory cloud chamber results indicate that fly ash is most efficient at cloud formation in the deposition mode at cirrus temperatures ($< -35°C$) and less efficient in the warm cloud (Section 4.3.1) and mixed phase (Section 4.3.2) regimes. Based on similar nucleation efficiency to dust at cirrus temperatures (Welti et al., 2009; Chapter 2), the diagnosed fly ash concentration is included in the dust concentration used by the CAM5-MARC heterogeneous nucleation scheme to calculate ice crystal number at cirrus temperatures. Observations of fly ash abundance in the atmosphere (Section 4.3.3) suggest that fly ash particle concentrations are low enough to have a negligible direct radiative effect. Therefore, the modeling component of this study isolates the effects of fly ash particles on cirrus cloud nucleation: the diagnostic fly ash is not allowed to contribute to the direct radiative forcing and is not used in calculations for mixed phase or warm cloud nucleation. Though the droplet uptake and wet deposition is not explicitly computed for fly ash separately from the BC loss processes, these and other loss processes are implicitly accounted for when comparing the upper atmospheric concentrations with observations as a function of sf: the observed concentrations are subject to all atmospheric loss processes, so observations provide a constraint on which range of sf captures realistic atmospheric fly ash burdens. In addition, the sulfur emissions from coal combustion and the associated cooling are equivalent between cases, so this treatment isolates the responses associated with changing fly ash emissions.

Total aerosol indirect effects in the CAM5-MARC are diagnosed using the radia-

tive flux perturbation method (Haywood et al., 2009; Lohman et al., 2010; Gettelman et al., 2012; Chapter 3). Top of atmosphere (TOA) radiative fluxes are computed using two six-year simulations, one with present-day (year 2000, hereafter PD) aerosol and precursor emissions and another with pre-industrial (1850, hereafter PI) emissions, and the perturbation is calculated as the difference between PD and PI averages of the variables of interest. TOA fluxes are used instead of fluxes at the tropopause to avoid aliasing associated with changes in cirrus clouds that occur near the tropopause. All simulations have prescribed greenhouse gas emissions and climatological sea surface temperatures derived from the years 1980-2000. The dust emissions are also held constant between the PD and PI runs. The total cloud forcing (dCF) is the sum of the changes in the short wave cloud radiative forcing ($SWCF$) and long wave cloud radiative forcing ($LWCF$): $dCF = (SWCF_{2000} - SWCF_{1850}) + (LWCF_{2000} - LWCF_{1850}) = dSWCF + dLWCF$. Also, the "clear-sky" diagnostics recommended by Ghan (2013) are used to calculate cloud forcing to correct for the "all-sky vs. clear-sky" biases that neglect above-cloud aerosol absorption and below-cloud scattering.

4.3 Results

4.3.1 Droplet activation results

Figure B-27 shows results from cloud droplet nucleation experiments described in Section 4.2.4. Measurements are taken for 200, 300, and 400 nm mobility-sized particles. After validating the CCNC using ammonium sulfate activation as a control experiment, size-dependent critical supersaturations are used to find κ values to represent particle hygroscopicity following the methodology of Petters and Kreidenweis (2007). κ values for the fly ash particles are found to be between 0.04 and 0.32 and fall into the "moderately hygroscopic" range (Petters and Kreidenweis, 2007).

4.3.2 Ice activation results

Figure B-28 shows results from the ice nucleation and droplet freezing experiments described in Section 4.2.3. Measurements are made using 300 and 700 nm mobility sized particles (corresponding to the peaks observed in the mobility distributions in Figure B-25) as well as polydisperse particles (using the 650 nm traditional impactor, with size distributions shown in the middle row of Figure B-25). Figure B-28a shows a phase diagram with 1% activated fraction data. The x and y error bars correspond to uncertainties in temperature and S_{ice} conditions reported by the SPIN chamber. Immersion freezing at the 1% level is observed at temperatures colder than $\sim -20°C$, and deposition freezing at the 1% level is observed at temperatures colder than $\sim -30°C$. Figure B-28a also shows a classical nucleation theory (CNT) parameterization to fit the deposition nucleation data following the formulation outlined by Detwiler and Vonnegut (1981) for silver iodide ice nucleation. The functional form of this parameterization is:

$$S_{T1} = S_{T0}{}^{(T0/T1)^{3/2}}$$

where $T0$ is the warmest temperature where deposition nucleation is observed ($\sim -30°C$ for these data), S_{T0} is the water saturation level corresponding to $T0$, and S_{T1} is the predicted saturation level for activation at some $T1$ that is colder than $T0$. Figure B-28b shows ice nucleation active site density, n_s, as a function of temperature for the immersion mode freezing data. n_s is the number of ice nucleation active sites per aerosol surface area as a function of temperature:

$$n_s(T) = -\frac{log(1 - f_{IN}(T))}{A_{aer}}$$

where T is temperature, $f_{IN}(T)$ is the fraction of activated particles at a given temperature (at water saturation), and A_{aer} is the total surface area of the aerosol particle population (Connolly et al. 2009). Using n_s normalizes measured values by surface area and allows for comparison of freezing results of different particle sizes. The error

bars indicate the uncertainty in n_s due to the classification error in the machine learning technique used to determine ice fractions, and the data at warmer temperatures have larger error bars because they are near the uncertainty threshold. Since the particle morphologies are observed to be spherical (Figure B-23), the area of a sphere of a given mobility size is used for n_s calculations. Also shown in Figure B-28b is the empirical fit to immersion freezing data reported by Umo et al. (2015).

4.3.3 Observational constraints

Figure B-29 shows vertical profiles of fly ash from aircraft campaign estimates as well as profiles of fly ash concentrations diagnosed from BC in CAM5-MARC with $sf = 0.1$ and 1. The aircraft data are binned in 1000-700, 700-500, and 500-0 hPa pressure bins. The model profiles are annual mean fields that are collocated with the mean location of the aircraft data, and the error bars show spatial variability in fly ash concentration in the model across the latitudinal and longitudinal extent of the aircraft data. There is more spatial variability in fly ash concentrations at the surface, but there is less spread at higher (and more cirrus-relevant) altitudes. In general, the $sf = 0.1$ and 1 model profiles bracket the field data.

The fly ash concentrations diagnosed from BC are only used by the cirrus ice nucleation component of the model. These calculations occur primarily in higher altitude grid cells that experience the requisite lower temperatures, and there is the best agreement aloft where the concentrations are used by the model. The observational data also suggest that the relevant loss processes that affect fly ash concentrations are adequately accounted for when comparing the upper atmospheric concentrations with observations. In particular, sf values between 0.1 and 1 capture the realistic range in atmospheric fly ash burdens.

4.3.4 Modeling results

Figure B-30 shows globally averaged dCF responses to changes between globally averaged PD and PI cloud top ice crystal number concentration ($dINC$) and cloud top

ice crystal effective radius ($dREI$) for all cases. Less negative values for dCF are associated with larger values of $dINC$ and more negative values of $dREI$. dCF saturates at larger sf values with a marked decrease at $sf = 100$, suggesting nonlinearity in model behavior for more extreme sf cases. dCF is the balance of the long wave (warming) and short wave (cooling) cloud forcing components: $dLWCF$ responses are more sensitive to increasing sf until the largest sf values, where $dSWCF$ responses become more sensitive. For these highest emissions cases, the amount of fly ash rivals the amount of total BC in the atmosphere, and the model is unlikely to capture a realistic climate response, since the influence of fly ash on radiation and other types of cloud formation can no longer be assumed to be small compared to its affects on cirrus.

The spatial variability in dCF responses is shown in Figure B-31 for all cases. dCF is negative in a global average but has considerable spatial heterogeneity. This heterogeneity increases with increasing sf, with larger extremes of dCF with larger sf. There is overall increased high cloud ice crystal number and ice crystal mass with increasing sf on a global average, but the increasing sf amplifies the existing regional differences in cloud response. Since fly ash concentrations are uniformly diagnosed from BC despite emission source heterogeneity, the actual variations in regional response are unlikely to be captured with the present treatment and are subject to larger uncertainty than the global estimates.

Figure B-32 shows the globally averaged response of dCF (Figure B-30a) to different amounts of fly ash emissions and the sensitivity of changes in dCF to changes in fly ash emissions. There is a positive trend in dCF as a function of sf for observationally constrained values ($0.1 \leq sf \leq 1$). This trend suggests that due to cirrus cloud responses, the aerosol indirect effect becomes less negative with increasing fly ash emissions near current levels. The difference in dCF between the $sf = 0.1$, 0.5, and 1 cases and the $sf = 0$ case is between $\sim$ 0.1 and 0.6 W m^{-2}, which provides an estimate of the influence that fly ash emissions have on the climate system via modification of cirrus clouds. Therefore, based on the observational bounds of atmospheric fly ash burden, there is between $\sim$ 5×10^{-9} and $\sim$ 2×10^{-8} W m^{-2} climate

warming per kg of fly ash emitted in addition to the associated CO_2 release from coal combustion.

4.4 Discussion

Despite the similarities between mass spectra from fly ash particles and mass spectra from mineral dust particles, there are differences in their efficiency as CCN. While mineral dust particles have relatively low hygroscopicity, between 10^{-3} and 10^{-2} (Herich et al., 2009; Garimella et al., 2014), the results from this study indicate that fly ash particles are moderately hygroscopic. This relatively larger hygroscopicity is likely associated with the larger abundance of soluble sulfates and phosphates in fly ash than in mineral dust (Figure B-26). This larger hygroscopicity may increase the probability that fly ash will be wet deposited before reaching cirrus altitudes. However, combining emissions inventory estimates and aircraft observations indicate that these particles are present at cirrus levels concentrations of $\sim 0.1-1\ \mathrm{L}^{-1}$ (Figure B-29).

Figure B-27b shows that 300 nm particles exhibit higher n_s values than the 700 nm particles. These results indicate that the ice nucleation efficiency per unit surface area of the particles in this study does not scale with particle size, but instead that the smaller particles are more efficient INP per unit surface area. Since these particles are increasingly enriched in heavy metals with decreasing particle size (Davison et al., 1974; Smith et al., 1979), and heavy metals are known to contribute INP efficiency, this size-dependent enrichment can explain this measured size dependent n_s. Furthermore, the mode size of the fly ash particles considered by Umo et al. (2015) is ~ 10 μm, so the size-dependent heavy metal content can also explain the lower reported n_s for the larger particles previously considered. Since particles with the sizes considered in this study have longer lifetimes in the atmosphere (Seinfeld and Pandis, 2006), the larger n_s reported in the present study are likely to be more applicable to particles found in the atmosphere.

The aircraft data in this study constrain the atmospheric burden of fly ash: they

suggest that near current levels of emissions, fly ash contributes between $\sim$ 0.1 and 0.6 W m^{-2} of warming via perturbations to cirrus clouds. In these emissions cases, a less negative dCF is associated with larger values of $dINC$ and more negative values of $dREI$. For cirrus clouds that are primarily formed via heterogenous nucleation, an increase in ice crystal number contributes a net warming effect (Cziczo et al., 2013a; Storelvmo et al., 2013). Also, the long wave emissivitity of optically thin clouds increases with decreasing effective radius (Garrett et al., 2002), and this phenomenon is often associated with the influx of anthropogenic aerosols (Lubin and Vogelmann, 2005; Garrett and Zhao, 2006). Fly ash perturbations to cloud top ice crystal number and ice effective radius lead to an increased ability for cirrus clouds to emit outgoing long wave radiation: since they do so at higher altitudes (i.e. emitting long wave radiation at colder emission temperatures than those found at lower altitudes), fly ash emissions are found to increase the ability of cirrus clouds to warm the climate system.

Overall, particles with spherical morphologies similar to that of fly ash are observed in cirrus cloud residuals, and the laboratory results from this study suggest that fly ash nucleates ice crystals efficiently at cirrus-relevant temperatures. The aircraft observation constraints on the modeling results suggest that these particles have the potential to contribute a large additional warming to the climate system in addition to the CO_2 released from coal combustion. Therefore, anthropogenic emissions of these particles could play a significant role in how humans are perturbing the climate system via effects on the formation and persistence cirrus clouds. In addition, this study motivates future work to assess how uncertainties associated with the treatment of fly ash nucleation and emissions affect model results: in particular a more explicit treatment of fly ash as prognostic variable would likely narrow the range of possible amounts of extra warming from coal combustion.

4.5 Policy implications

As discussed above, particulate matter emissions from coal combustion pollute the environment from both an air quality and climate change perspective. The heavy metal enrichment of fly ash particles also causes them to pose a significant health risk when inhaled (e.g., Smith et al., 2006). The laboratory and modeling work in this study indicate that this heavy metal content, along with other chemical properties, also allows these particles to efficiently seed cirrus clouds in the atmosphere. Overall, in the relatively polluted atmosphere (which describes the current state of Earth's atmosphere), emitting more fly ash particles is found to modify cirrus clouds and will result in a correspondingly warmer climate.

Despite projected decreases in coal combustion for energy production in developed countries over the next several decades, global electricity production from coal is projected to remain steady through 2050 due to the increases in coal use in developing countries (Reilly et al., 2015). In developed countries like the USA, regulations mandate that coal particle emissions are scrubbed using ESPs (Jaworek et al., 2007). Modern ESPs are able to remove $\sim$ 99% of fly ash from coal stacks, but they contribute an extra cost of several millions of dollars to coal plant construction or retrofitting (Mussatti et al., 2002). With the projected expanse in coal use in the developing world and uncertain levels of adoption of ESP technology due to this extra cost, a mechanism that would decrease the amount of fly ash released would help mitigate the corresponding negative human health and climate effects.

Article 12 of the Kyoto Protocol defined the Clean Development Mechanism (CDM) to allow an Annex B countries (ones with an emission-reduction or emission-limitation commitment) to implement an emission-reduction project in developing countries to earn CER credits to be counted towards meeting Kyoto targets (Kyoto Protocol, 1999). The aim of the CDM was to stimulate sustainable development and emission reductions and provide developed countries flexibility in meeting targets, but the CDM expired along with the Kyoto Protocol in 2012. The Paris Agreement, which comes into effect in 2020, provides for a new "mechanism to contribute to the

mitigation of greenhouse gas emissions and support sustainable development" in Article 6 (Paris Agreement, 2015). Since the details and implementation of this new mechanism are yet to be decided, it provides an ideal opportunity to mitigate the negative effects of fly ash emissions.

The UNFCCC Secretariat is currently tasked with creating and managing this mechanism, and it has the opportunity facilitate the transfer of ESP technology between countries by allowing such a transfer to qualify to earn CER credits towards meeting Paris Agreement targets. In such a transfer, CER credits would apply only for currently operating power plants or ones already under construction so as not to incentivize building new coal plants. With this scheme, any climate cooling from power plant sulfur emissions would be equivalent with or without an ESP, so the pricing can be determined based on additional warming from fly ash alone. An ESP would reduce the extra climate impact from fly ash over the entire life of a power plant, which on average is 42 years in the US (EPA, 2016): therefore, the relevant time horizon for this comparison is $\sim$ 40 years.

Based on the modeling results, the range estimated extra warming per kg of fly ash is between $\sim$ 5×10^{-9} and $\sim$ 2×10^{-8} W m^{-2}. Using the IPCC values for the absolute GWP of CO_2 from Myhre et al. (2013), each kg of fly ash that is (not) emitted is equivalent to between $\sim$ 2700 and 11000 kg of CO_2 over this 40 year timeframe with a mean value of $\sim$ 6800 kg CO_2 / kg fly ash (Figure B-33). This equivalency can be used to set the value of CER credits earned for ESP technology transfer. Since fly ash GWP decreases with time, there is also an incentive for the transferring country to specify that the receiving country shorten the operating life of coal plants in order to maximize the CER credits earned, helping meet both the emissions reductions and sustainable development goals of the mechanism (Sutter and Parreño, 2007). Overall, such efforts would ultimately minimize both the negative health and climate impacts (both from CO_2 and fly ash) from coal fired power plants.

In summary, because of the additional warming and health risks associated with the emissions of fly ash particles from coal combustion, the UNFCCC Secretariat is encouraged to consider ESP technology transfer (for existing and already-planned coal

plants) between countries as a way to earn CER credits as part of the "mechanism to contribute to the mitigation of greenhouse gas emissions and support sustainable development" described in Article 6 of the Paris Agreement.

Chapter 5

Conclusions

5.1 More ice nucleation measurements

Chapter 2 presents the performance of a new ice nucleation chamber and new methods to analyze ice counter data. The introduction of SPectrometer for Ice Nucleation (SPIN) as a commercially available ice chamber is similar to the introduction of the Cloud Condensation Nuclei Counter (CCNC) (Roberts and Nenes, 2005; Lance et al., 2006) in that it will allow ice nucleation measurements to be made with higher temporal and spatial coverage. Figure B-34 illustrates how the introduction of a commercial cloud chamber can affect the amount of research being conducted on experimental cloud nucleation, using topic data from the ISI Web of Science Database (Thompson Reuters, 2016). It shows time series of publication rates for papers using a CCNC (top) or a continuous flow diffusion chamber (CFDC) (bottom). The commercial CCNC was introduced in 2005 and precedes a $\sim$ doubling in publication rate. This rapid increase can be contrasted with the much slower growth in publication rate for CFDCs, where only a few additional research groups entered the field in the late 2000s with custom-built chambers. With the introduction of the SPIN chamber, which will allow many more research groups to perform online ice nucleation measurements, the amount of research being conducted on ice nucleation is expected to increase.

The methodologies highlighted in Chapter 2 allow ice nucleation measurements to be made with increased experimental flexibility and reproducibility than previ-

ously possible and also with fewer assumptions in the analysis. The addition of a depolarization detector and data analysis using supervised machine learning (ML) algorithms allow for robust determination of particle phase with uncertainty quantification. Overall, the SPIN chamber reproduces laboratory data measured by previous CFDCs, and the analysis in Chapter 2 quantifies uncertainties in the measurements. Through lowering the barrier for entry in performing ice nucleation measurements, the SPIN instrument will help constrain the influence of ice nucleation on the atmospheric radiation budget and the initiation of precipitation, thereby leading to a better understanding of the impact of ice formation on the Earth's climate and water budget.

5.2 Uncertainty in ice cloud parameterizations

The research presented in Chapter 3 explores the systematic low bias in field measurements of ice nucleating particles using CFDCs. It investigates an artifact that has been present in CFDC data for decades, and presents the first quantification of its effects. It highlights how CFDC measurements have (also for decades) been conducted at unphysical conditions to measure immersion freezing and that accounting for this artifact explains the unphysical supersaturation dependence of immersion freezing results. Overall, if heterogeneous ice nucleation parameterizations based on CFDC measurements are to be used extensively in the global modeling community, it is critical to account for both (a) for the under-prediction of ice nucleating particles (INP) in these observations, and (b) for the variability (especially in the tails of the distribution) of INP measured with this technique. Small changes in these details, as shown in Chapter 3, can lead to divergent estimates of the magnitude of aerosol impact on ice clouds within the same modeling framework. This thesis research also suggests that minimizing the uncertainty in estimates of this bias, e.g. with the ML techniques presented in Chapter 3, is an prudent step in developing heterogeneous ice nucleation parameterizations based on CFDC measurements.

In order to incorporate CFDC measurements in global models as a means of re-

ducing the uncertainty that INP contribute to the climate system, both experimental and modeling efforts must carefully account for the variability in instrument bias and consider the uncertainty associated with it. This research provides a novel approach to endogenize the variability of the low bias using the stochastic parameterization framework for data from other CFDC instruments. Using the approaches highlighted in Chapter 3 will help minimize the measurement uncertainty associated with historical and future data and also properly propagate measurement uncertainty into model estimates.

5.3 Fly ash and climate

Chapter 4 uses the new experimental and analytical capabilities developed in the previous two chapters to investigate the impacts fly ash particles on cloud formation and climate. It examines the physical and chemical properties of several types of fly ash particles and the efficiency with which they form cloud droplets and ice crystals in the laboratory. It discusses how particles with spherical morphologies similar to that of fly ash are observed in cirrus cloud residuals, and the laboratory results with fly ash suggest that it nucleates ice crystals most efficiently at cirrus-relevant temperatures. This chapter also uses aircraft observations to constrain the amount of fly ash to be used in a global climate model. The modeling results in Chapter 4 suggest that these particles have the potential to contribute a large additional warming to the climate system in addition to the CO_2 released from coal combustion, motivating the policy discussion. Since anthropogenic emissions of fly ash particles could play a significant role in how humans are perturbing the climate system via effects on the formation and persistence cirrus clouds, it is prudent to consider the effects of these emissions in existing policy frameworks intended to minimize the negative impacts of climate change.

5.4 Future work

The research presented this thesis also paves the way for additional work to explore the topics considered. In particular, it motivates research on improving the SPIN chamber capabilities, continuing the assessment of CFDC uncertainty, and reducing the uncertainty associated with fly ash radiative forcing.

The work presented in Chapter 2 motivates future work to extend the ML approach to analyzing field data and to compare the SPIN chamber performance with other ice counters both in the laboratory and in the field. Once large enough datasets are generated for field measurements, ML classifiers can be used for distinguishing frost from real ice in the field. Also, the general ML approach can be used for other instruments with size-only data: for example, an SVM that uses size only would find the optimal size (by maximizing the margin between ice and aerosol training data) to distinguish the two classes and quantify the uncertainty associated with choosing this size via cross-validation. Future SPIN designs should also consider several hardware and software changes that would improve data quality and automation. For example, minimizing chamber leak rates and 3D printing components from less thermally-conductive material would improve field measurement quality by reducing the frost background. Also measuring the spatial and temporal variability of the ice layer thickness could improve the accuracy of reported thermodynamic conditions.

The research presented in Chapter 3 motivates future work to apply a ML approach to quantify and minimize uncertainty in historical CFDC data. Ideally, all CFDC-type chambers should perform similar analysis as part of instrument characterization. This way, the variability of cf for a particular instrument would be inferred on a measurement-by-measurement basis to correct laboratory and field data. The variability in cf would then also be included when fitting parameterization constants. After exploring the experimental uncertainty, the sensitivity of the parameterization constants to variability in the cfs could then also be quantified. Furthermore, the research in this chapter motivates experimental and computational fluid dynamics (CFD) investigation to minimize lamina spreading, e.g. by exploring which flow con-

ditions minimize lamina spreading via more isokinetic injection of aerosol. This type of investigation could yield further reductions in experimental uncertainty, especially if paired with an ML approach to provide statistical corrections of any biases in the CFD-derived response surface for lamina thickness.

The research presented in Chapter 4 motivates future work to study the types of fly ash emitted in developing countries to characterize potential variability in cloud formation potential. It motivates comparing how different laboratory instruments characterize fly ash particles, i.e. as BC, mineral dust, or some other particle type. It also motivates field measurements of aerosol composition to provide a more complete picture of the spatial and temporal variability of concentrations of potential INP. From a modeling perspective, it calls for a more explicit treatment of fly ash in a both a global and cloud-resolving modeling framework to narrow the range of possible amounts of extra warming. For the former, fly ash concentrations should be treated prognostically in the model, and emissions should incorporate the spatial differences between fly ash and BC sources. Such an effort could also explicitly model the CCN behavior of fly ash the a warm cloud activation scheme. Overall, a more careful treatment of fly ash in a global model would help reduce the uncertainty in the radiative forcing effect per emitted ton of fly ash and would also improve the efficacy of policy mechanisms to curb the extra warming. Also, additional policy analysis should be conducted that investigates how to maximize the efficacy of the proposed approach and considers how to formulate the specifics in the context of the Paris Agreement stocktakes.

5.5 Concluding remarks

In conclusion, the research presented in this thesis investigates anthropogenic aerosol particles and clouds in a changing climate. The role these particles play in the formation and persistence of ice clouds remains one of the most uncertain aspects of understanding past, present, and future climate. These studies highlights that studying ice nucleation requires careful measurement of particle ice nucleating ability as well as

robust uncertainty quantification of experimental results. Laboratory measurements and their corresponding uncertainties are extended for use in climate models to probe how anthropogenic particle emissions affect climate through ice cloud formation. This type of investigation is then used to motivate policy decisions about controls on anthropogenic particle emissions. Overall, this thesis presents a vertically-integrated approach to clarifying the human role in the climate system by 1) developing instrumentation to perform ice nucleation measurements, 2) quantifying the uncertainty associated with these measurements using ML algorithms, 3) incorporating measurements and uncertainty quantification in climate model simulations, and 4) using the modeled climate response to motivate policy decisions for anthropogenic particle emissions.

Appendix A

Tables

		mey	0.1B	B	3B	4B	5B	10B	stoch
$LWCF$	PD	22.44	22.43	23.34	25.64	26.63	27.46	30.71	27.70
(W m^{-2})	PI	21.91	21.74	22.94	25.62	26.63	27.60	31.07	27.92
	Δ	0.53	0.70	0.40	0.02	0.00	-0.14	-0.36	-0.22
$SWCF$	PD	-55.37	-55.29	-56.41	-58.71	-59.83	-60.61	-63.72	-60.86
(W m^{-2})	PI	-53.21	-52.94	-54.17	-57.00	-57.91	-59.03	-62.30	-59.30
	Δ	-2.16	-2.35	-2.24	-1.71	-1.91	-1.59	-1.42	-1.56
IWP	PD	10.57	9.89	11.04	13.47	14.57	15.52	19.59	16.03
(g m^{-2})	PI	10.62	9.89	11.19	13.84	14.99	16.01	20.29	16.60
	Δ	-0.05	-0.01	-0.15	-0.36	-0.42	-0.49	-0.70	-0.57
INC	PD	12.28	11.86	12.80	16.00	17.61	19.26	29.07	20.62
(L^{-1})	PI	11.11	10.78	11.90	14.83	16.62	18.66	28.59	20.07
	Δ	1.17	1.09	0.90	1.16	0.99	0.60	0.49	0.55
REI	PD	13.98	13.84	14.05	14.07	14.13	14.21	14.37	14.19
(μm)	PI	14.33	14.17	14.34	14.37	14.41	14.37	14.49	14.38
	Δ	-0.34	-0.33	-0.29	-0.30	-0.29	-0.16	-0.12	-0.19

Table A.1: Radiative and cloud properties for each case in PD runs (top row in each set), in PI runs (middle row in each set), and differences between PD and PI runs (bottom row in each set). For reference, the globally averaged $LWCF$ and $SWCF$ from the year 2000 CERES-EBAF observations are 26.0 and -47.1 W m^{-2}, respectively.

Appendix B

Figures

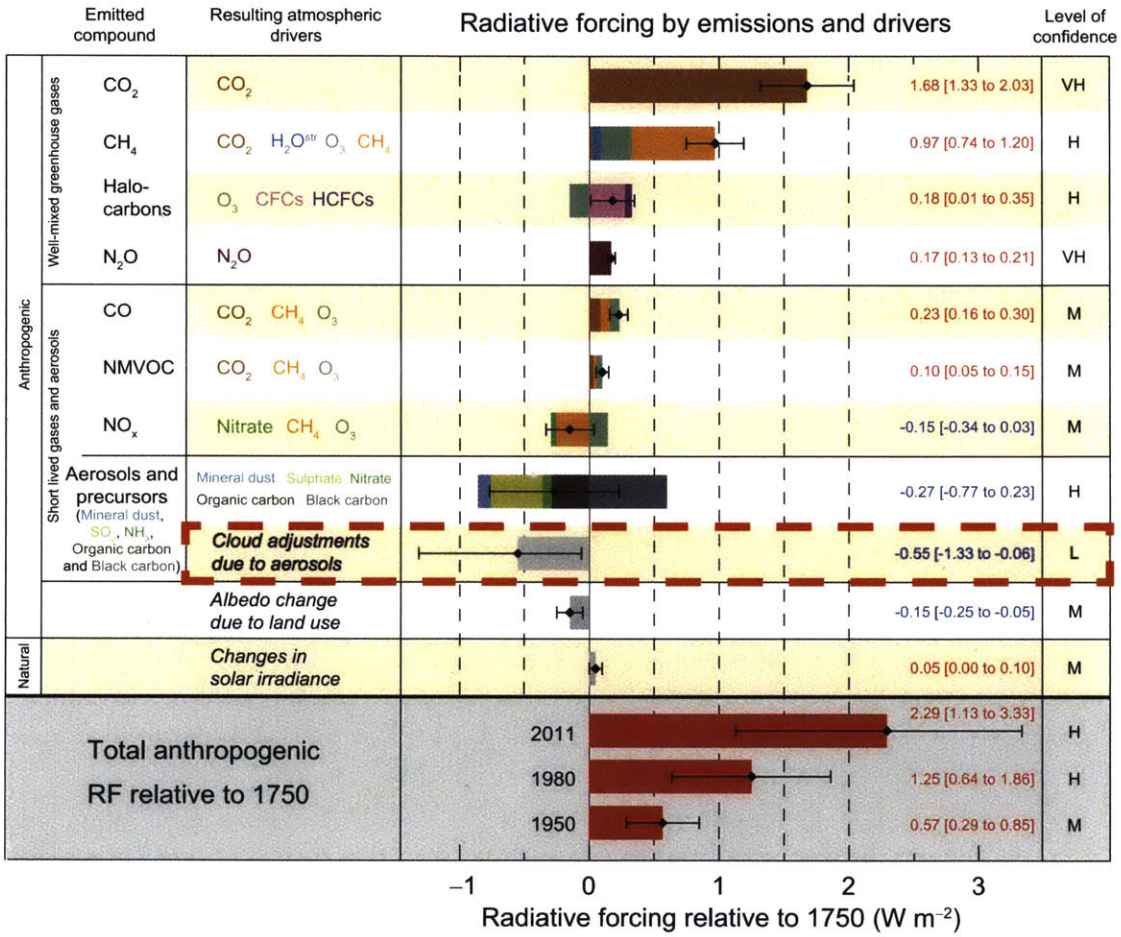

Figure B-1: Radiative forcing estimates in 2011 relative to 1750 and corresponding uncertainties for the main drivers of climate change, adapted from Stocker et al. (2013). The radiative forcing from cloud adjustments due to aerosols is highlighted to emphasize that these effects contribute the largest uncertainties in these estimates.

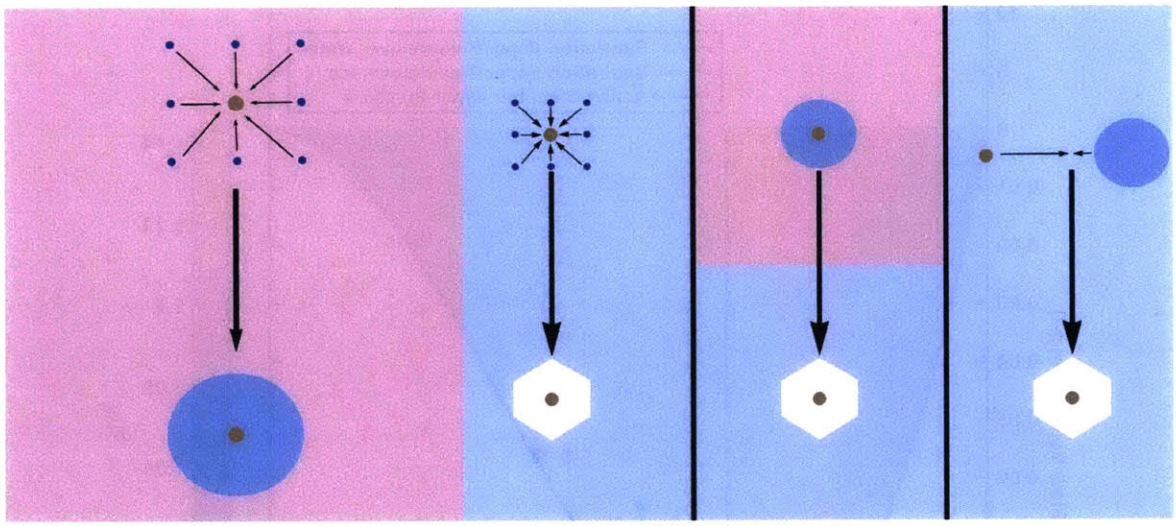

Figure B-2: Schematic representation of the main nucleation mechanisms in Earth's atmosphere. (From left to right) Droplet nucleation on a cloud condensation nucleus, deposition nucleation on a dry particle, immersion/condensation freezing of a preexisting droplet, and contact nucleation. See Section 1.2 for details.

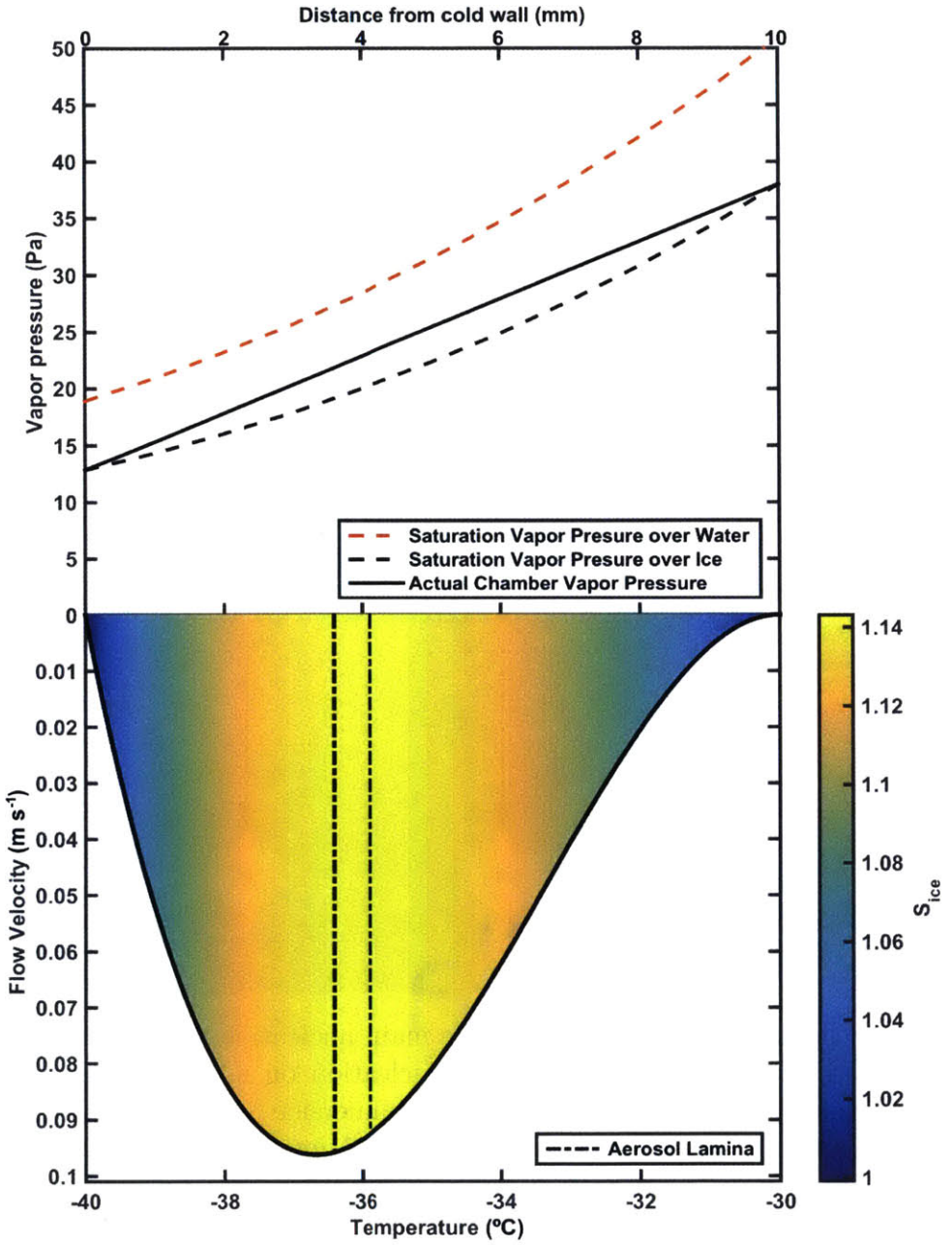

Figure B-3: Representation of idealized chamber thermodynamic and flow conditions with chamber width of 1 cm. The chamber cold wall (left) temperature is $-40°C$ and chamber warm wall (right) is $-30°C$. The top half of the figure shows the saturation vapor pressures over ice (black dashed line), over water (red dashed line), and chamber vapor pressure (solid black line) for 10 Lpm sheath + 1 Lpm sample flow. Note the chamber is supersaturated everywhere with respect to ice but subsaturated with respect to water. The bottom half of the figure shows the flow velocity profile with the aerosol lamina given by the black dash-dotted lines. The colors show the horizontal variation in the ice saturation ratio across the width of the chamber. The asymmetry in the flow profile is a result of the buoyant displacement of the flow towards the cold wall.

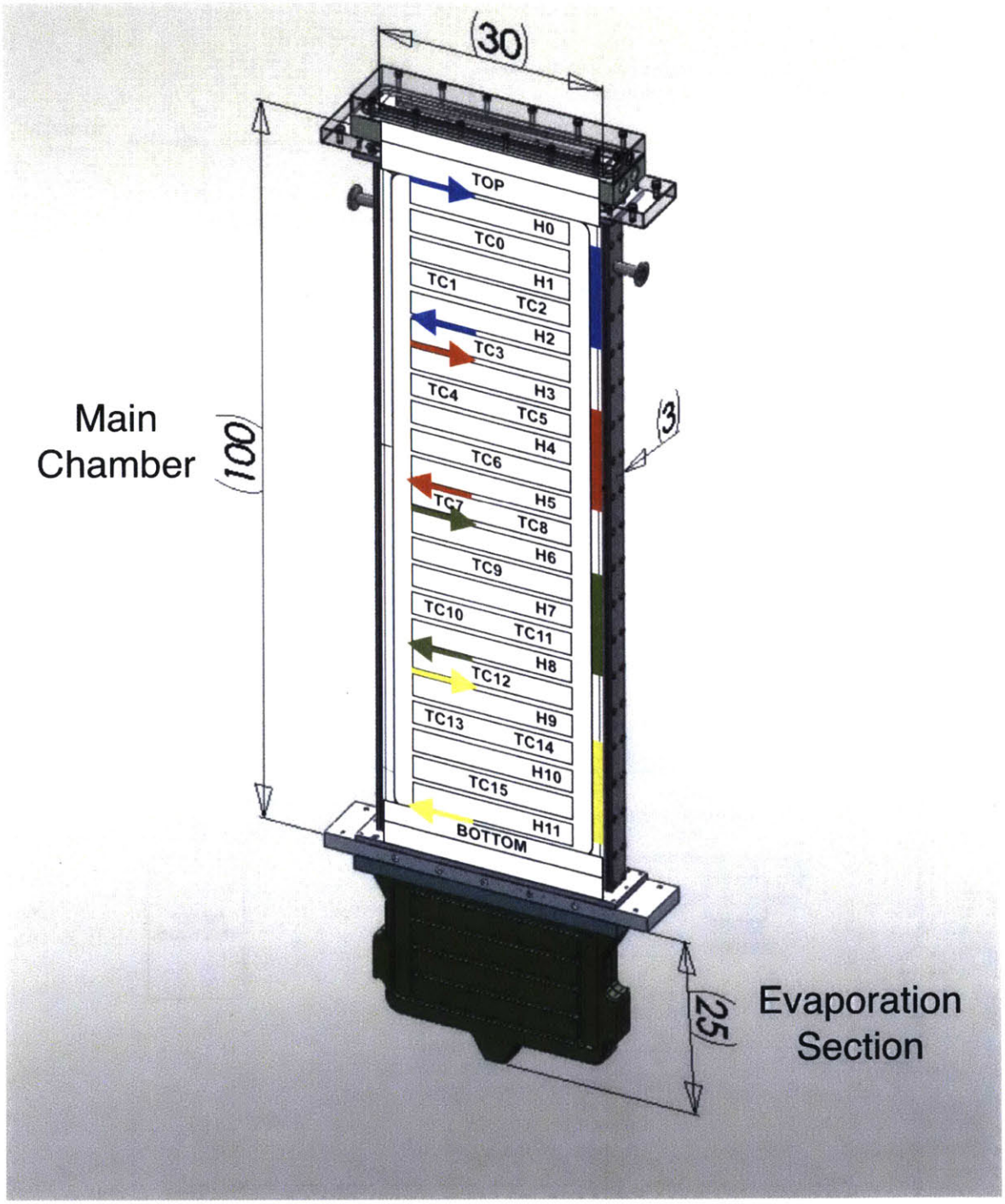

Figure B-4: SPIN chamber schematic showing dimensions of the chamber with overlaid thermocouple (TC0-TC15), heater (H0-H11), and refrigeration zone (colored arrows and blocks) locations on the main chamber. Heater strips span the length of the chamber wall at each indicated location. The different colored arrows represent different refrigerant paths depending on which of the four refrigeration solenoid valves are open. All dimensions are in cm.

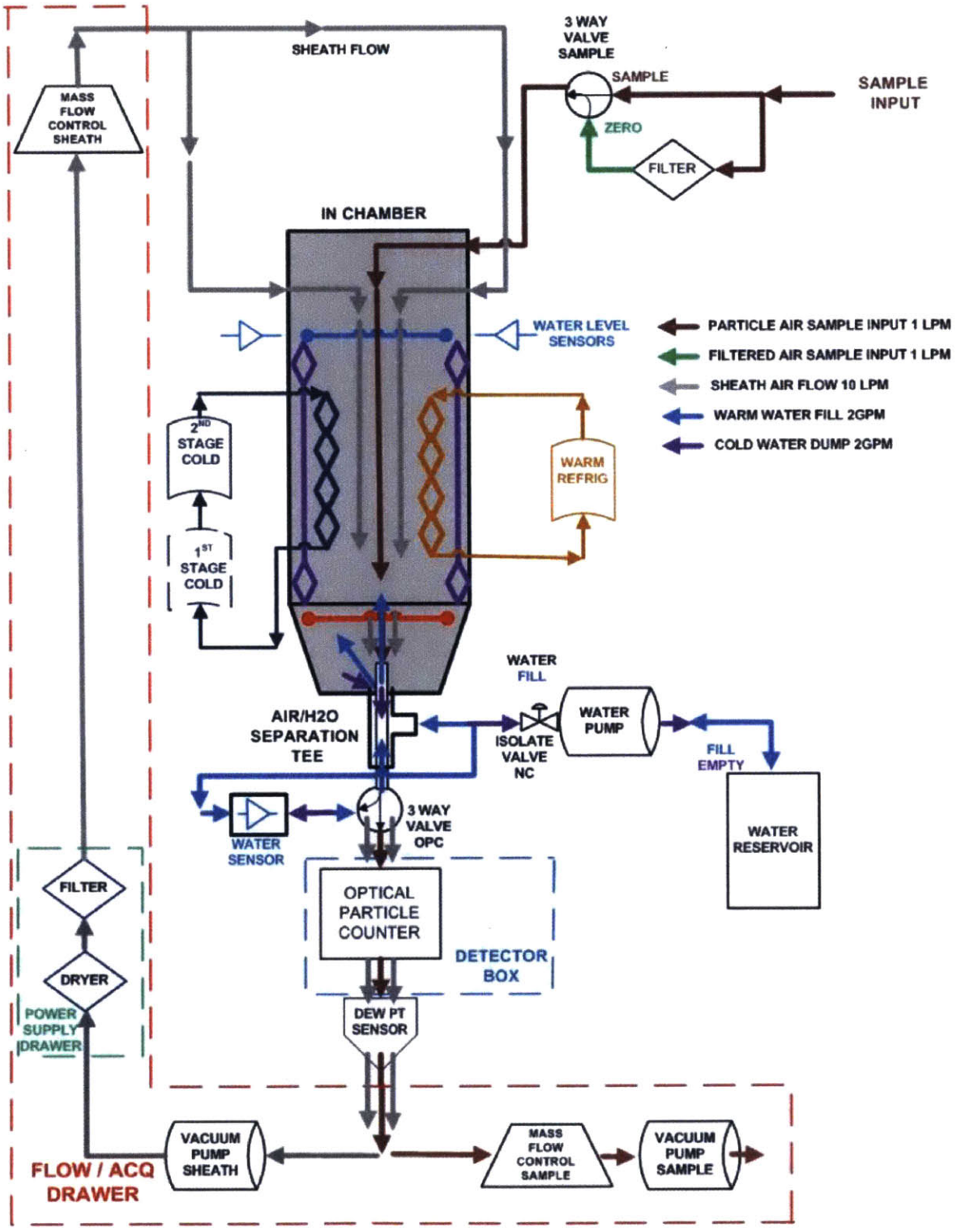

Figure B-5: Air and water flow diagram for the SPIN chamber.

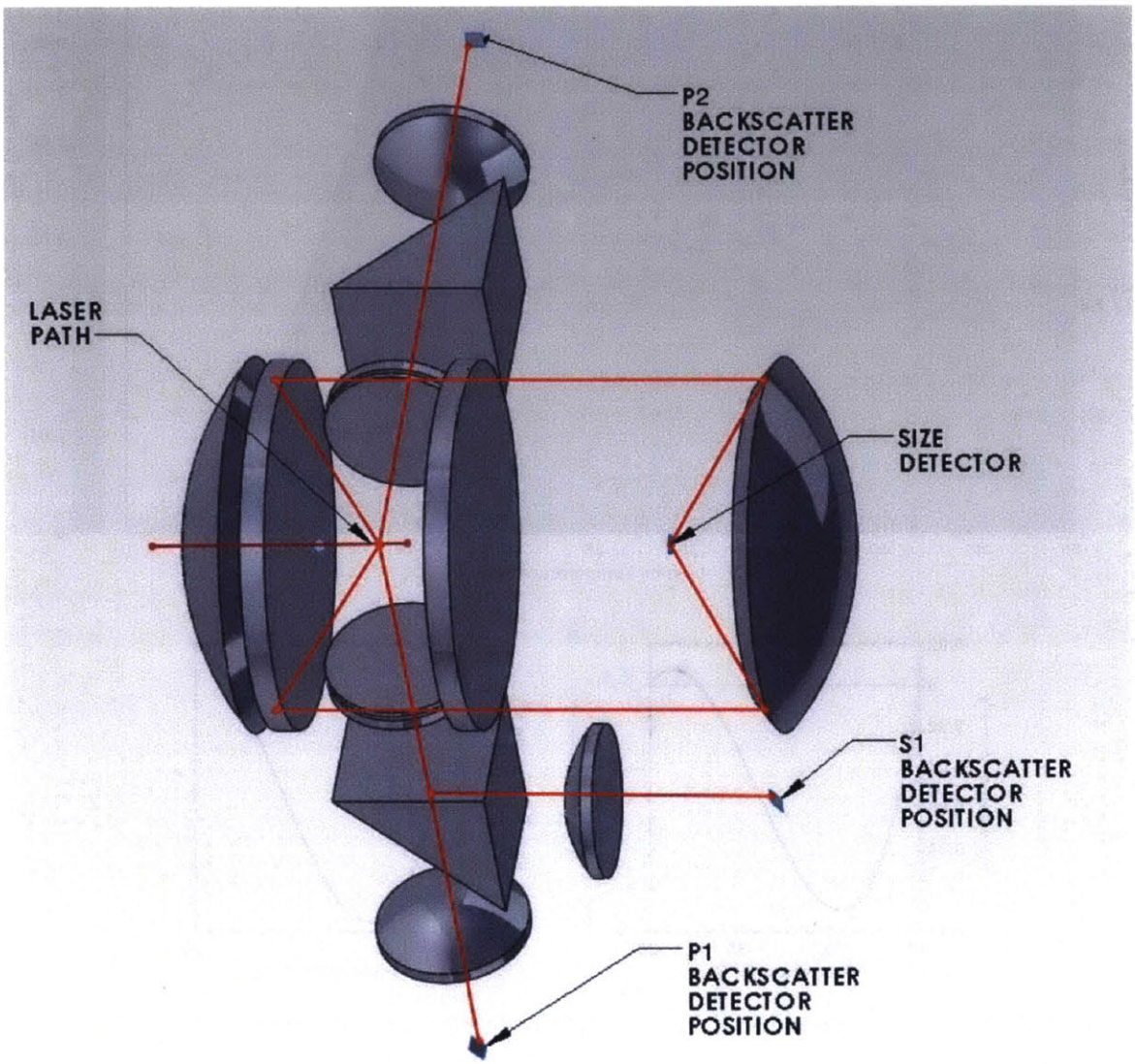

Figure B-6: Schematic optical setup of the SPIN OPC. The laser light is shown entering the sampling region, with side scatter rays traveling to the sizing detector, and the backscatter rays traveling to the depolarization detectors. See Section 2.2.2 for details.

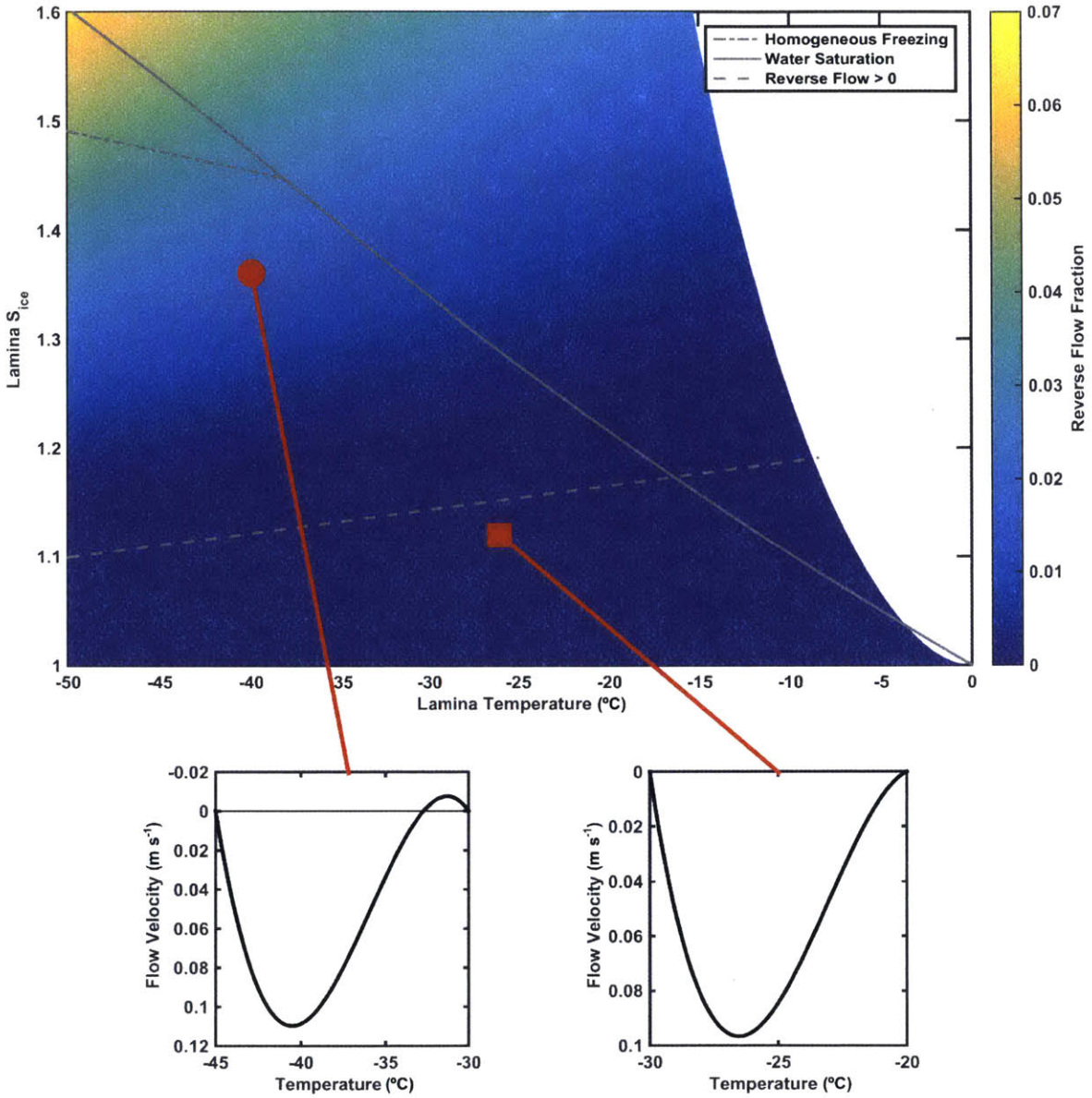

Figure B-7: Phase diagram of ice saturation ratio vs. temperature showing the thermodynamic conditions accessible by CFDC chambers. The color scale shows the ratio of (upward) reverse flow to (downward) normal flow in the chamber (with 10 SLPM sheath flow, 1 SLPM sample flow, and 1000 hPa chamber pressure) assuming a negligibly thick ice layer predicted by Rogers (1988) with the dashed grey line marking the boundary between zero and nonzero flow reversal (see Section 2.3.1 for details). The solid grey line is water saturation, and the grey dash-dot line shows the onset of homogeneous freezing of solution droplets for $J = 10^{11}$ cm^{-3} s^{-1} from Koop et al. (2000). Two flow profiles are shown as insets: the coldest temperature in each corresponds to the cold wall temperature and the warmest to the warm wall temperature. Flow reversal occurs along the warm wall in one case (left, red circle) and not in the other (right, red square).

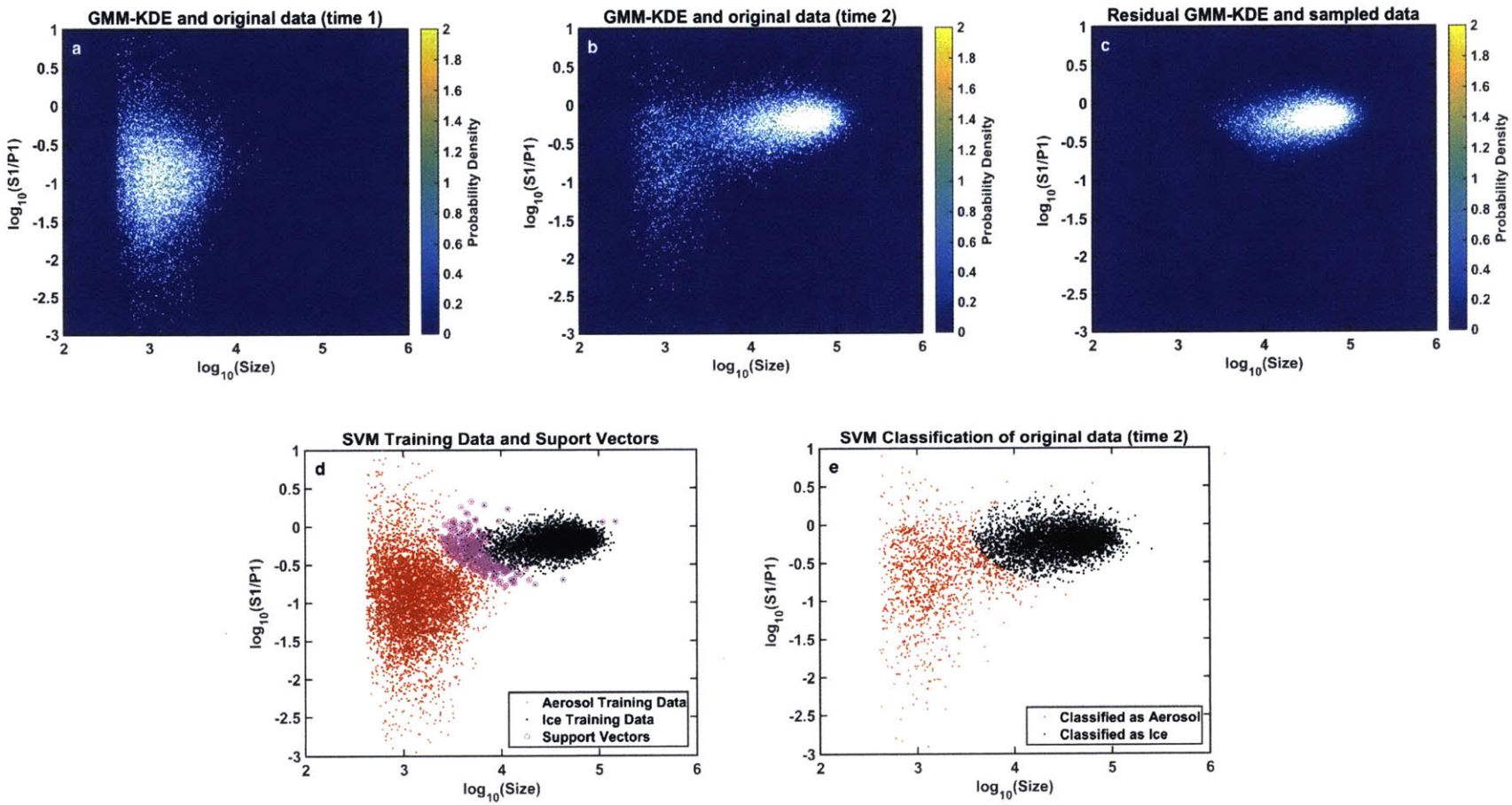

Figure B-8: Illustration of the supervised ML procedure used to classify OPC data in $\log_{10}$(S1/P1) vs. $\log_{10}$(Size) parameter space. The units of Size, S1, and P1 are all intensity counts. (a) Data and GMM-KDE for an aerosol only time interval (time 1). (b) Data and GMM-KDE for an aerosol + ice time interval (time 2). (c) Residual GMM-KDE (time 2 minus time 1) and data from weighted sampling informed by the deconvolved PDF. (d) Aerosol data, ice data and support vectors for SVM training. Cross-validated classification accuracy is 99% in this example. (e) Data from time 2 classified by SVM as aerosol and ice. See Section 2.3.2 for details.

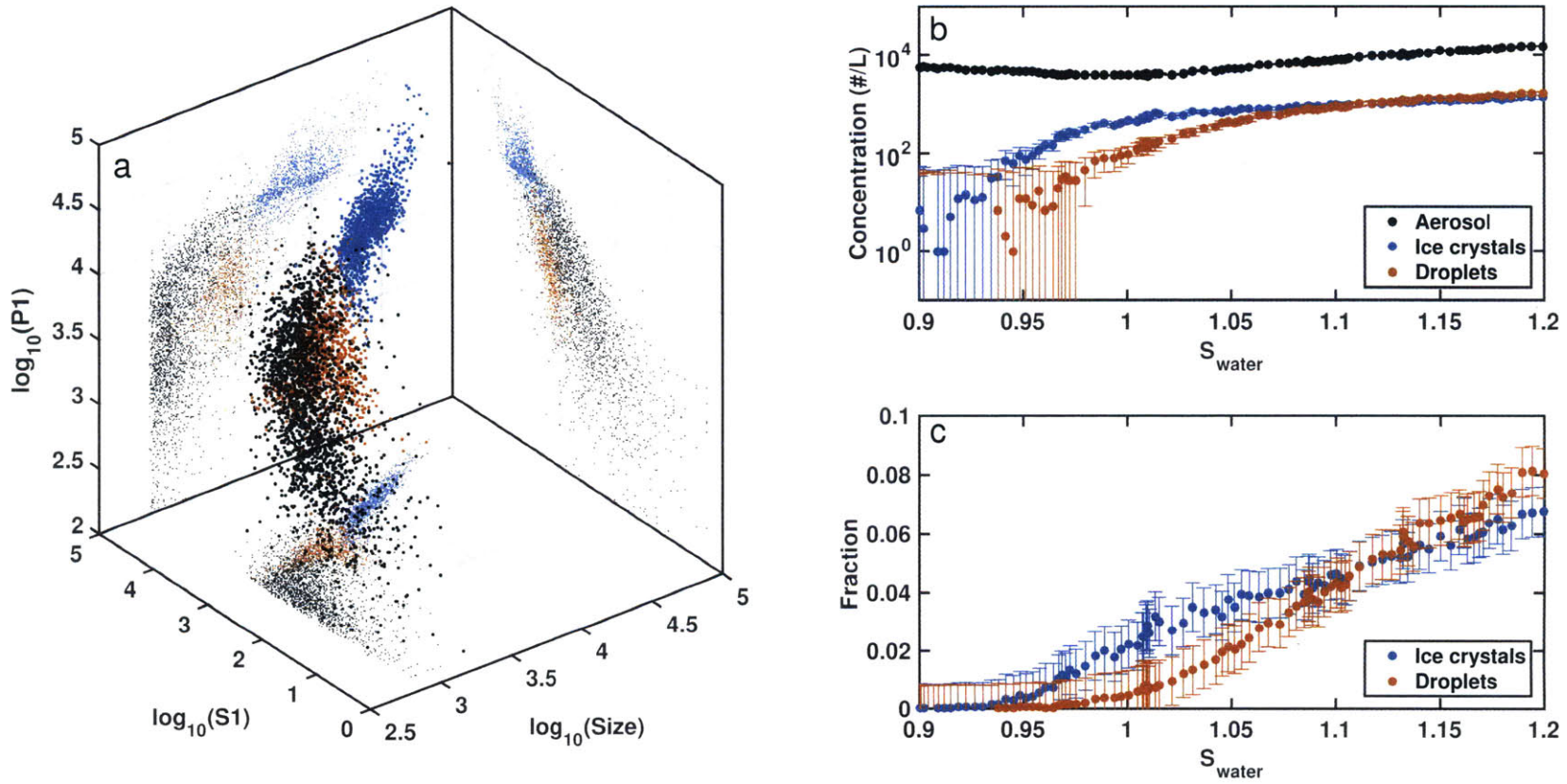

Figure B-9: Application of 3-class supervised ML on an example activation experiment where the chamber RH is increased. (a) Aerosol particles (black), ice crystals (blue), and water droplets (red) shown in $\log_{10}$(P1) vs. $\log_{10}$(S1) vs. $\log_{10}$(Size) parameter space with classification accuracy of 99%. 2D projections of the data are shown at axes limits with smaller markers. (b) Concentration of aerosol particles, ice crystals, and water droplets as a function of chamber RH. Error bars represent classification uncertainty. (c) Fraction of particles activated as ice crystals and water droplets as a function of chamber RH. Error bars represent classification uncertainty. Data points with lower error bars below zero indicate that the values are statistically indistinguishable from zero.

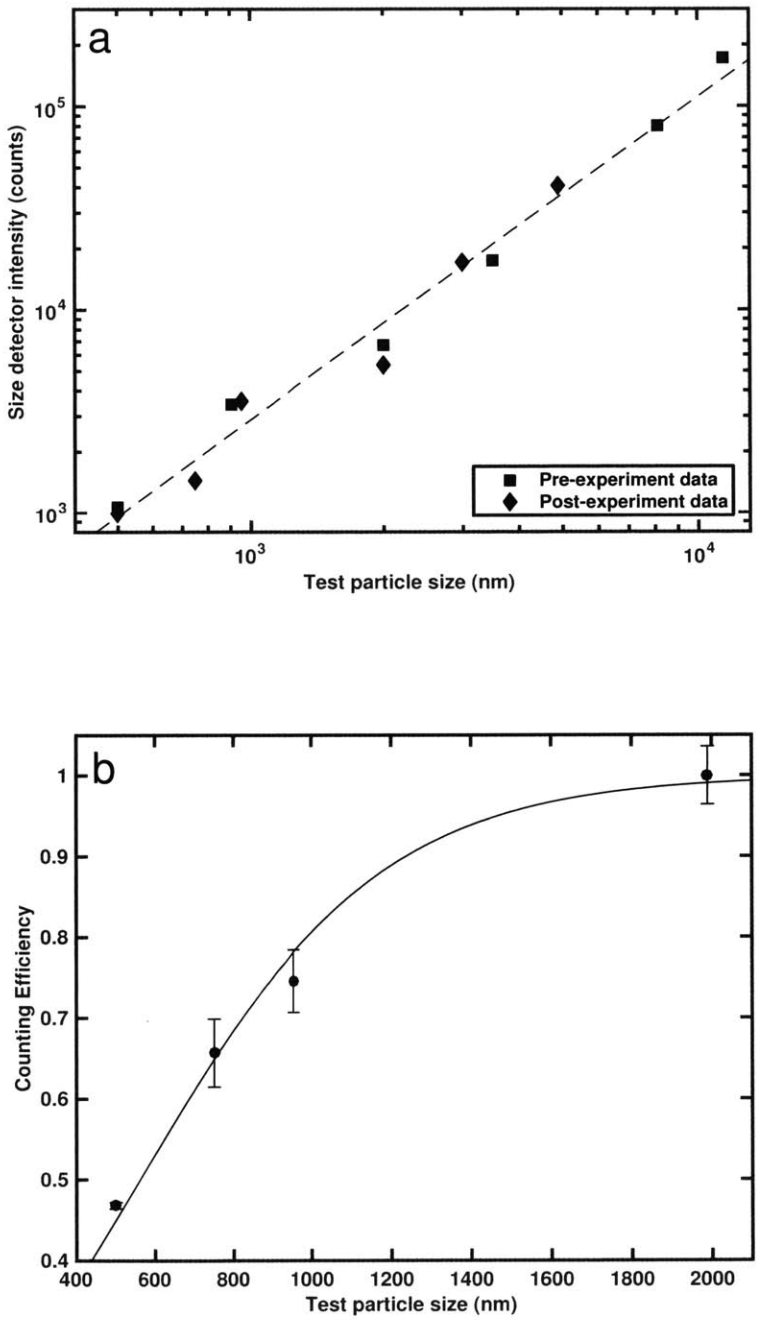

Figure B-10: Particle sizing and transmission efficiency of the SPIN detector. (a) Detector intensity counts versus test particle size before and after the freezing experiments in this study. Dashed line shows power law fit to the data. (b) Size-dependent counting efficiency of AS particles with sigmoid fit. Error bars show measurement uncertainty.

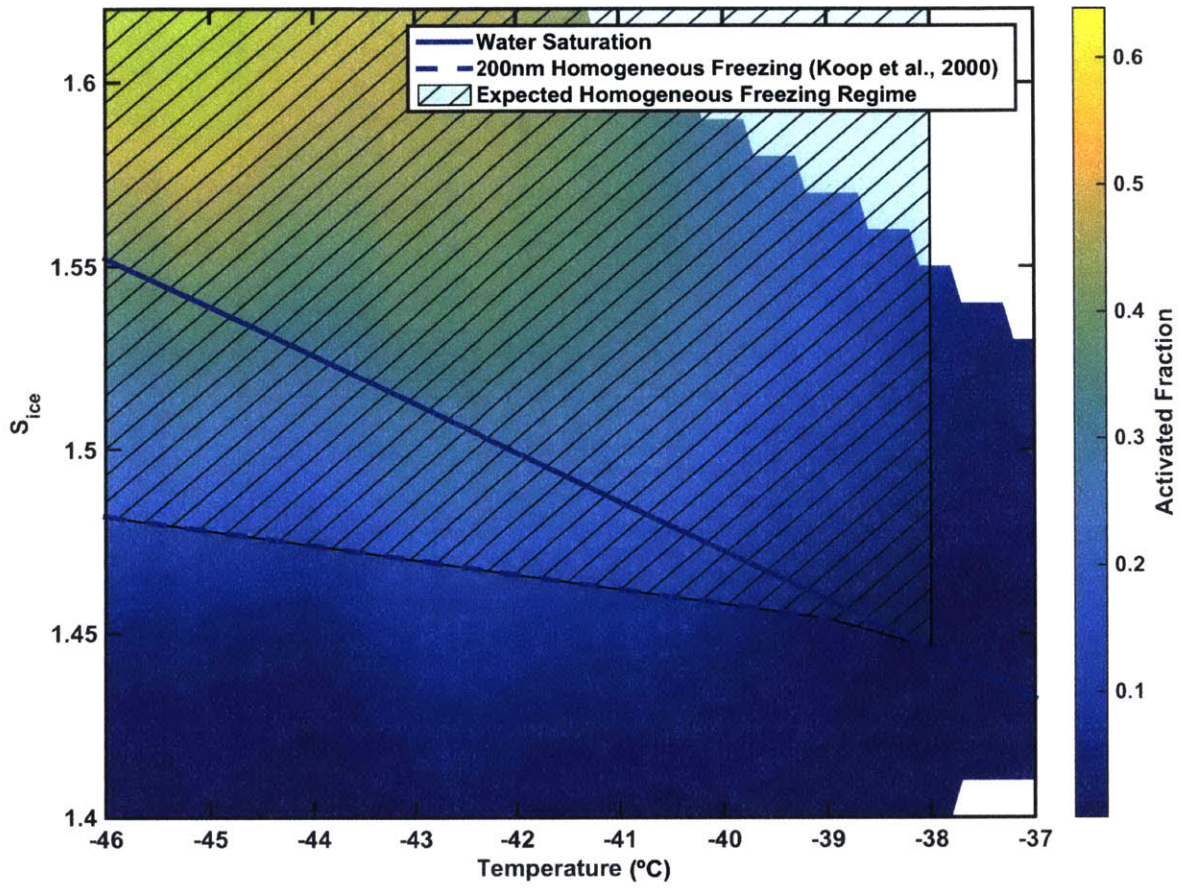

Figure B-11: Experimental homogeneous freezing results. The hatched and shaded area shows where homogeneous freezing of deliquesced haze droplets is expected to have occurred (gas phase chamber conditions below -38°C and above the $J = 10^{11}$ cm^{-3} s^{-1} line from Koop et al. (2000)). The color contours show interpolated activated fraction of ice crystals as a function of chamber conditions from 38 experiments (white areas are where no data are present). Typical aerosol number concentrations for such experiments are 100s of particles cm^{-3}. Typical uncertainties at one standard deviation for temperature are $\pm$ 1°C, for supersaturation are $\pm$ 5%, and for activated fraction are $< 1\%$.

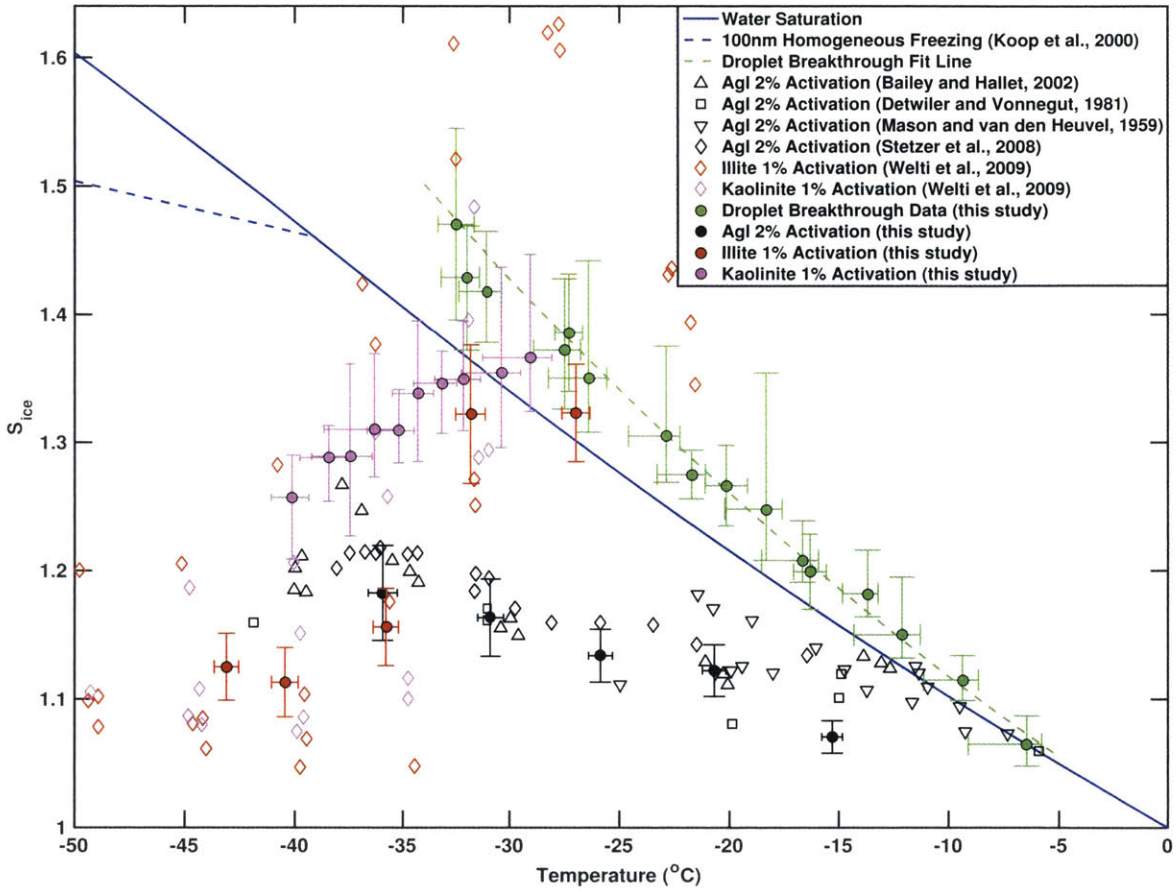

Figure B-12: Experimental heterogeneous ice nucleation results and comparison to literature with polydisperse NX illite, AgI, and 500 nm kaolinite particles. AS droplet breakthrough data and corresponding (quadratic) fit line are shown in green. Error bars represent uncertainty in lamina temperature and supersaturation conditions. The homogenous freezing line for solution droplets for $J = 10^{11}$ cm^{-3} s^{-1} from Koop et al. (2000) is also shown for reference.

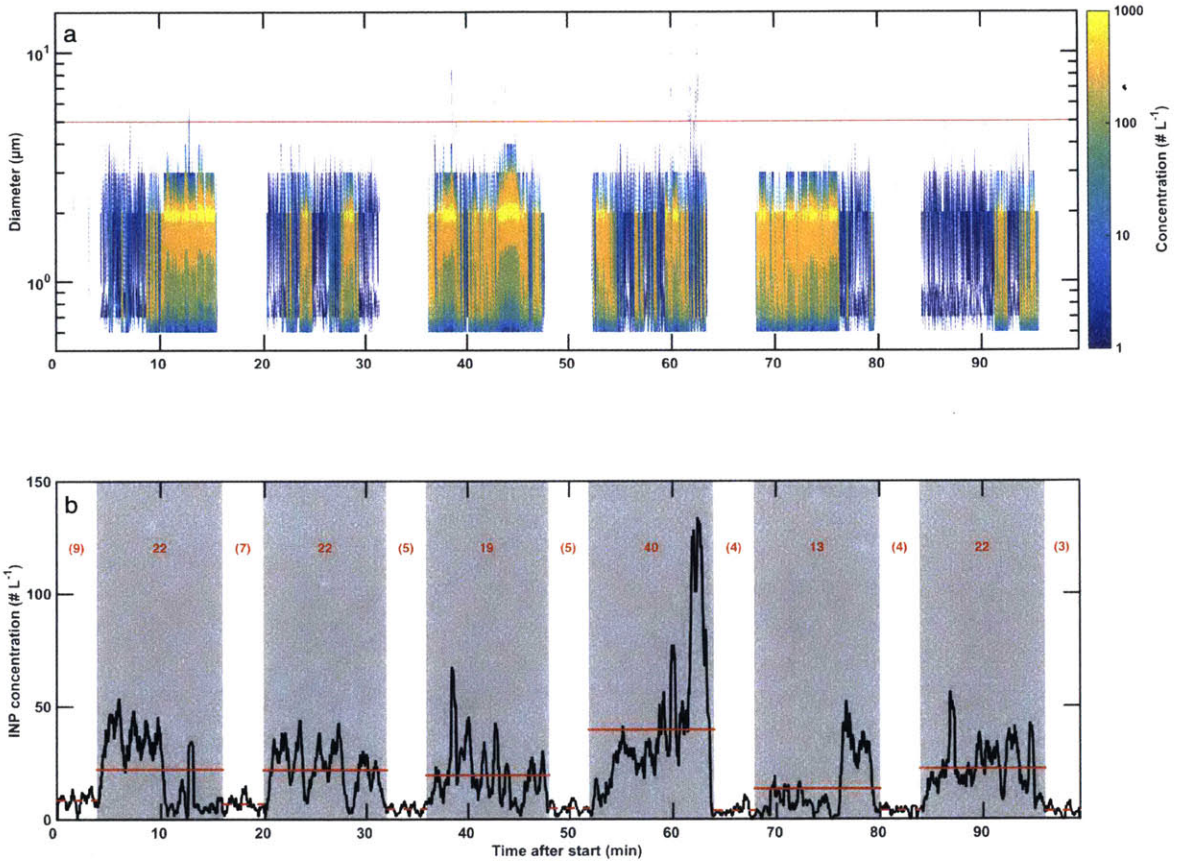

Figure B-13: Example field measurement at $\sim -30°C$ and $S_{liq} = 1.05$ (reported lamina temperature of $-30.7°C \pm 0.2°C$ and lamina S_{liq} of 1.05 ± 0.01 over the measurement period). (a) The OPC size histogram time series for this measurement. The red horizontal line shows the 5 μm size threshold for ice. (b) INP concentration time series using the 5 μm size threshold. Shaded areas show measurement periods and un-shaded areas show filter periods. Solid red horizontal lines show average INP concentrations from measurement periods (with the value specified above). Dashed red horizontal lines show average frost concentrations during filter periods (with the value specified above in parentheses).

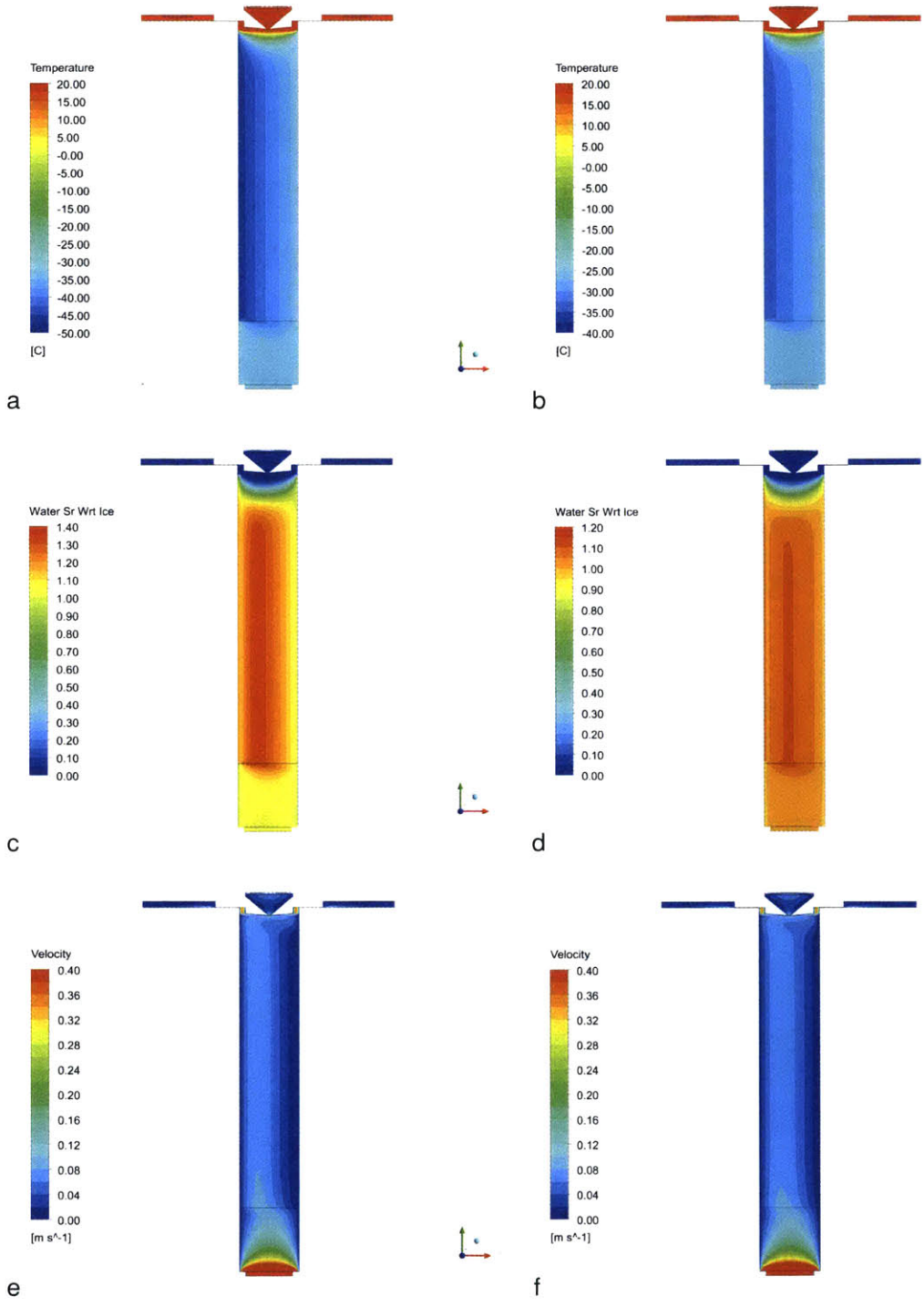

Figure B-14: Fluent simulation results for two sets of chamber conditions in a cross-sectional view. Left column shows results for nominal lamina temperature of $-40°C$ and lamina S_{ice} at 1.3. (a) Temperature (°C), (c) S_{ice}, and (e) flow velocity (m s^{-1}). Right column shows results for nominal lamina temperature of $-30°C$ and lamina S_{ice} at 1.1. (b) Temperature (°C), (d) S_{ice}, and (f) flow velocity (m s^{-1}).

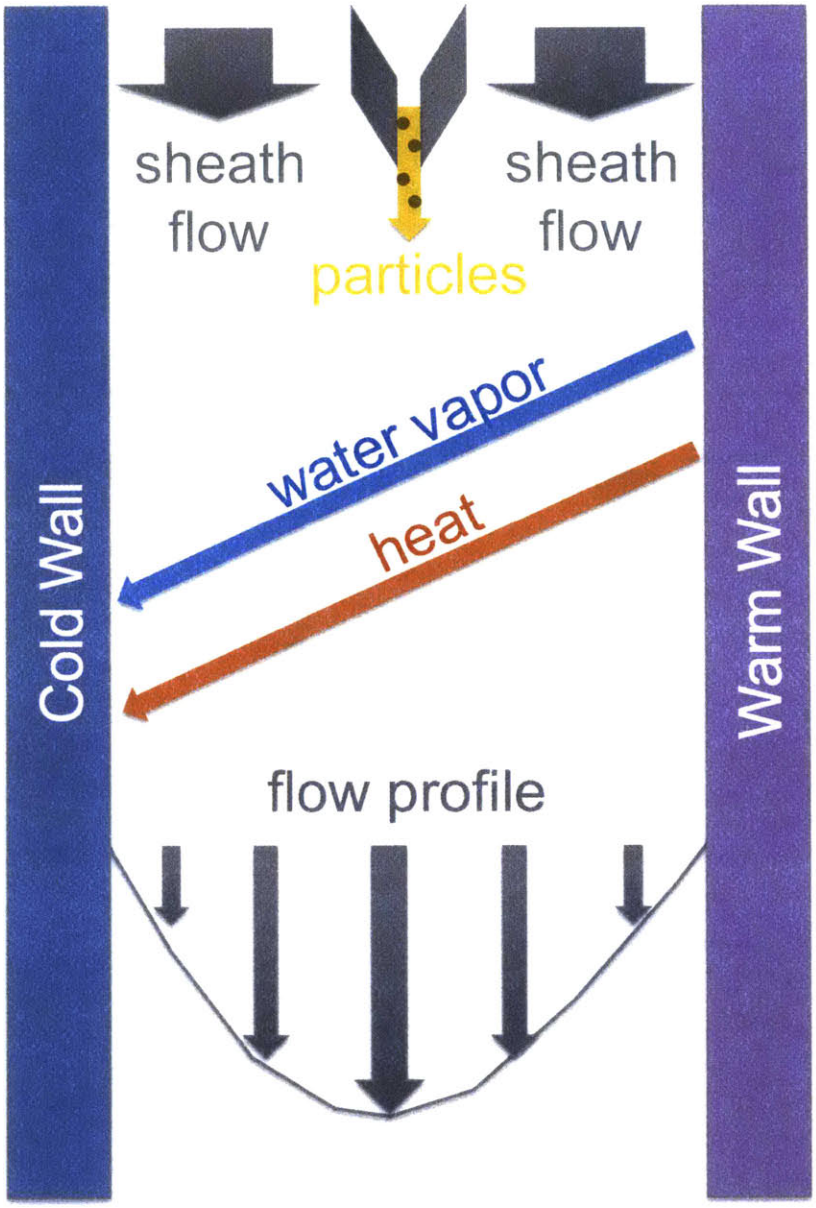

Figure B-15: Schematic representation of idealized CFDC operating conditions. Particle-laden flow is drawn between two sheath flows, and the two ice-coated walls are held at different temperatures (both below 0°C). This configuration results in water vapor and heat diffusing from the warm wall to the cold wall, setting up linear gradients of both quantities. With the nonlinear temperature dependence of the saturation vapor pressure, this setup results in supersaturated conditions with respect to ice everywhere in the chamber, with a maximum supersaturation near the center of the chamber.

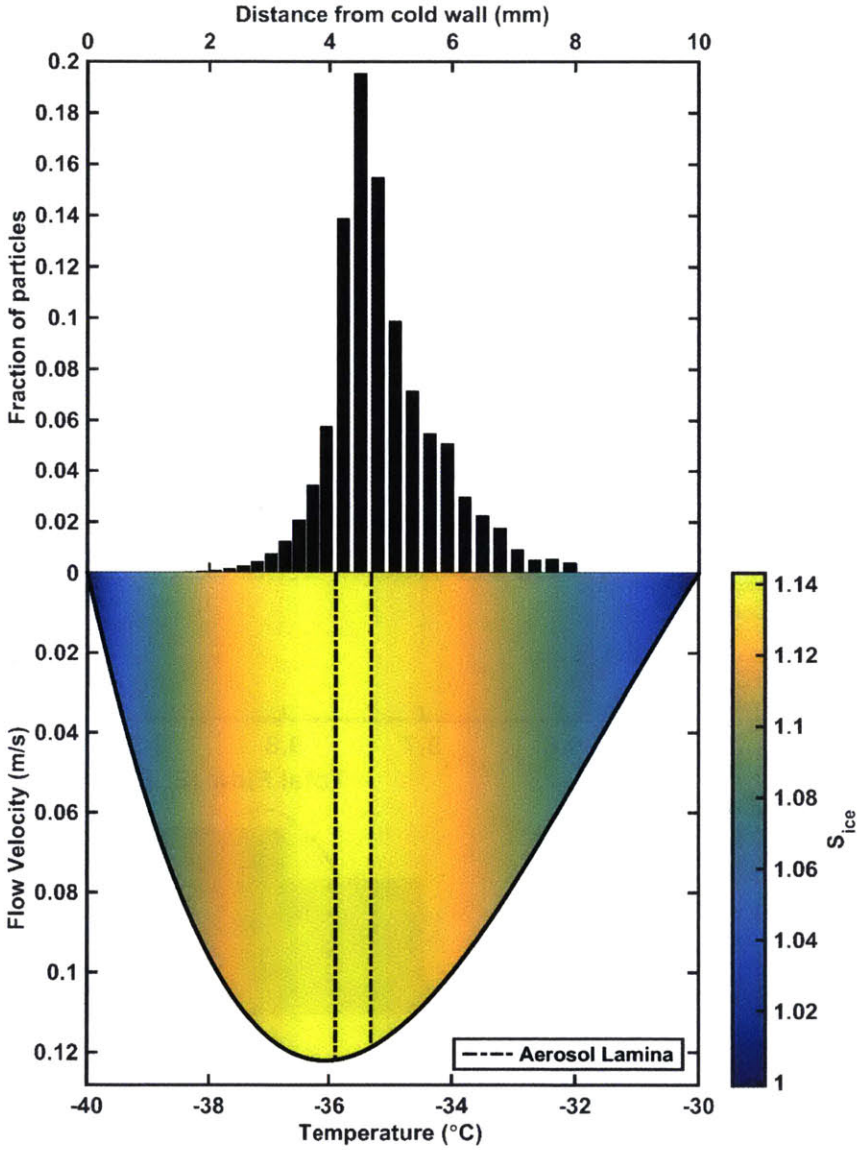

Figure B-16: (Top) Inferred particle distribution from measured aerosol pulse width and calculated chamber conditions. (Bottom) Chamber temperature, S_{ice}, and flow conditions corresponding to this inferred aerosol distribution. The dash dot line shows the location of particles in the chamber if they were constrained only to the theoretical aerosol lamina.

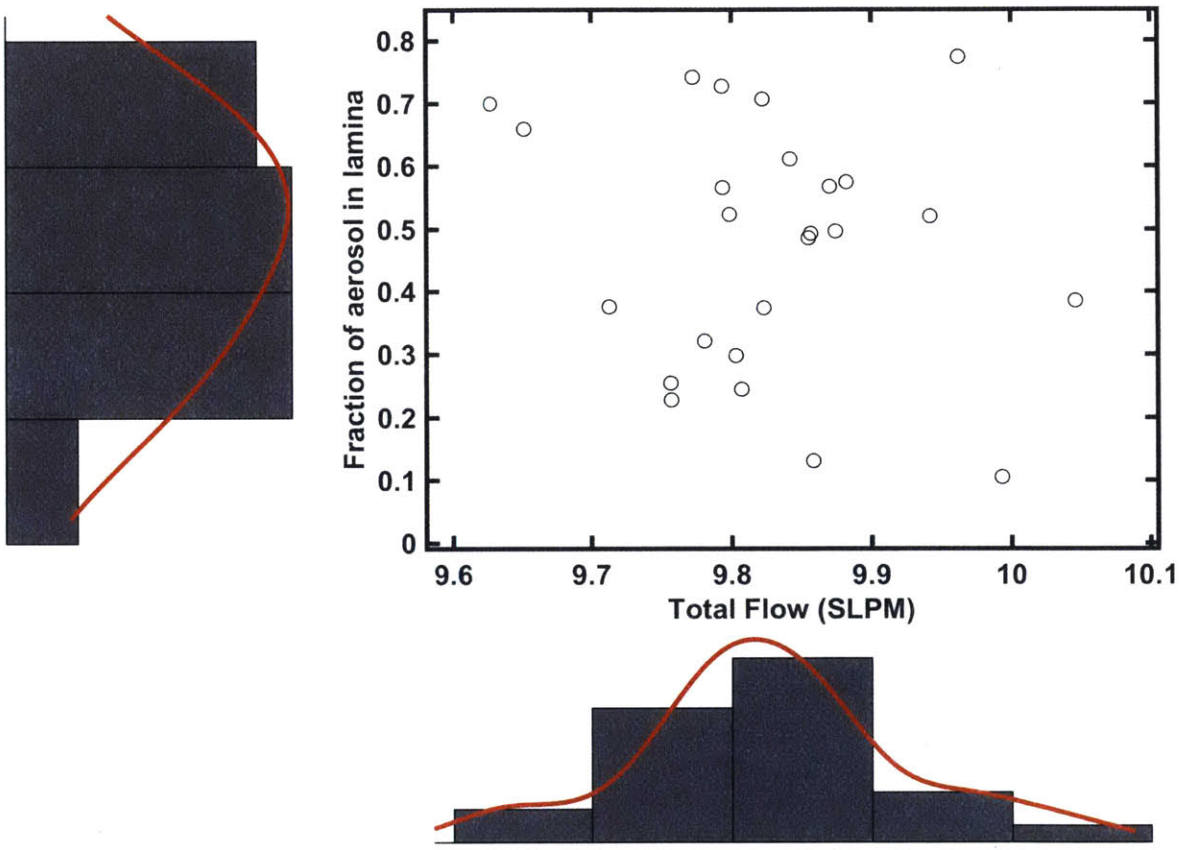

Figure B-17: Measured f_{lam} at constant conditions (room temperature, 10 SLPM total flow set point). The histograms on the left and bottom are the marginal distributions of f_{lam} and total flow, respectively, with corresponding kernel density estimates shown in red.

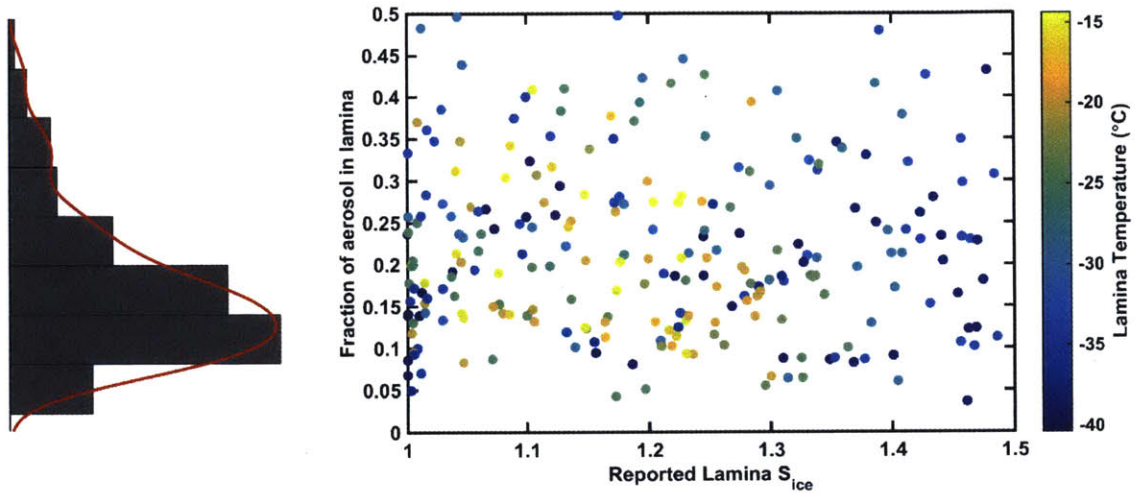

Figure B-18: Measured f_{lam} as a function of reported S_{ice} and temperature in the aerosol lamina. The histogram on the left is the marginal distribution of f_{lam} from all measurements with corresponding kernel density estimate shown in red.

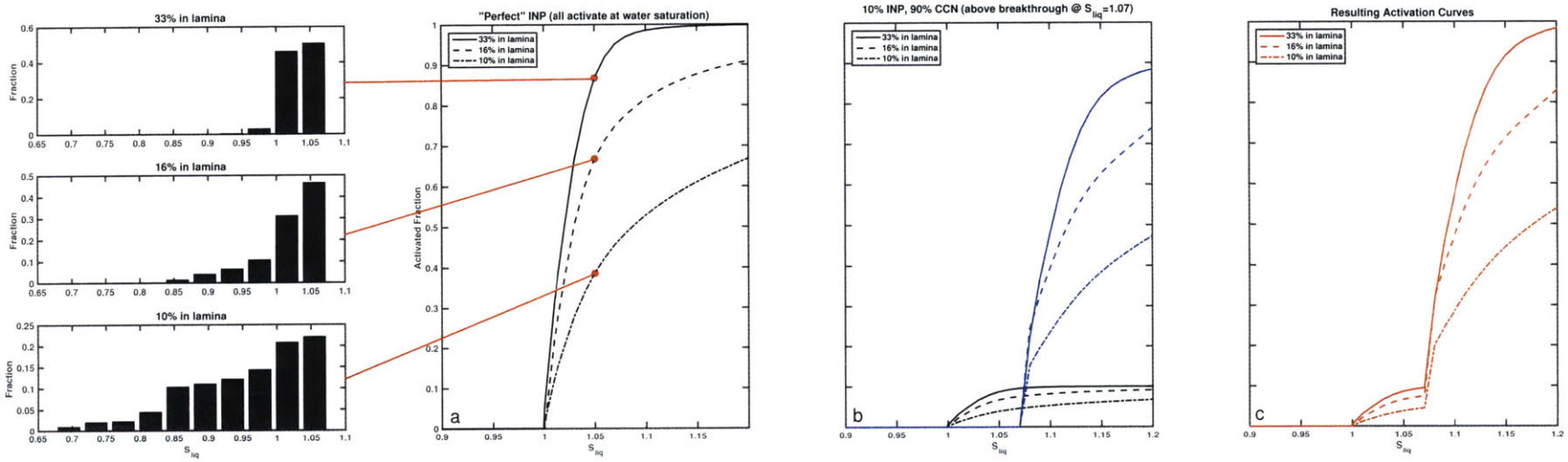

Figure B-19: (a) Idealized activation curves for INP that form ice crystals exactly at water saturation, given various f_{lam} values. The insets show the distribution of particles vs. S_{liq} when the reported $S_{liq} = 1.05$ for each of the f_{lam} values. (b) Idealized activation curves when 10% of particles in the chamber are INP that form ice crystals exactly at water saturation and the rest are CCN that survive the droplet evaporation region (Chapter 2) at a values of nominal $S_{liq} > 1.07$, given various f_{lam} values. (c) The resulting activation curve in case (b) if droplets and ice crystals are indistinguishable.

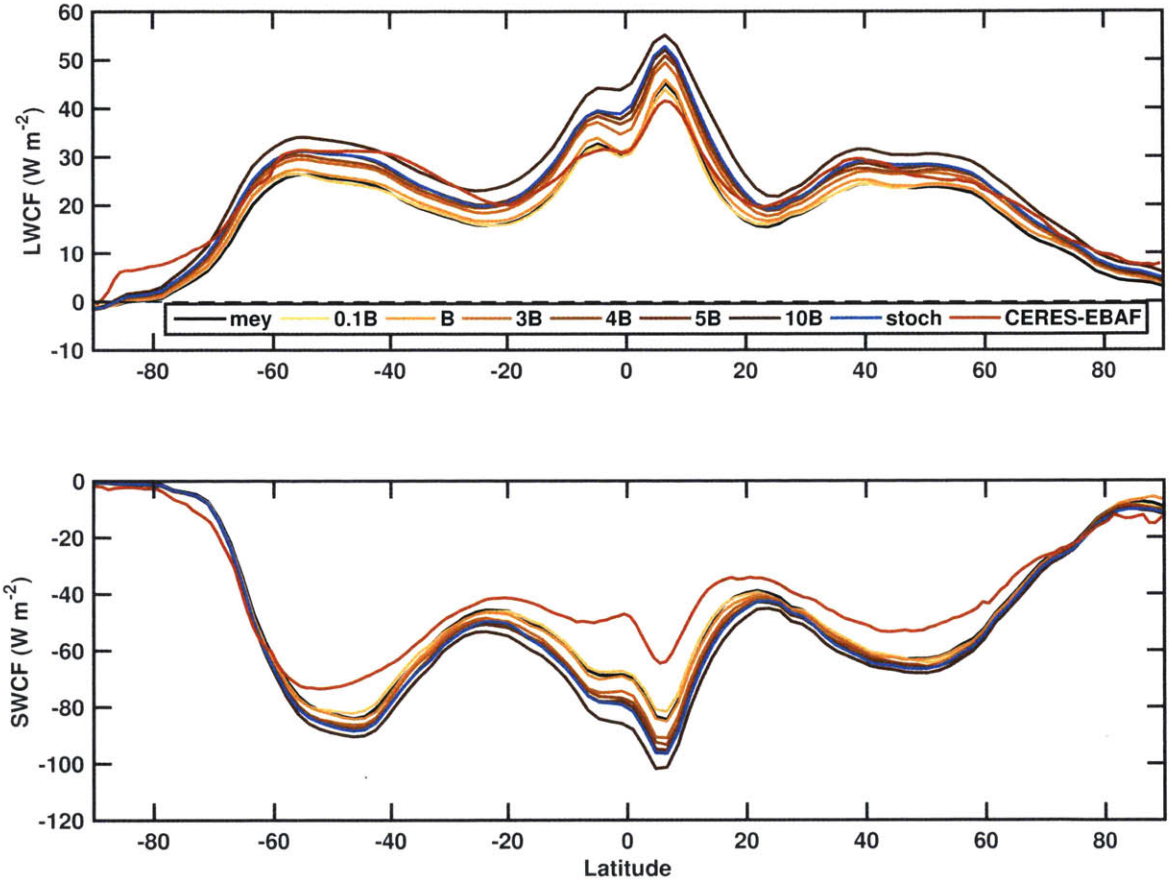

Figure B-20: Zonal averages of PD (a) $LWCF$ and (b) $SWCF$ for all cases as well as for CERES-EBAF satellite observations.

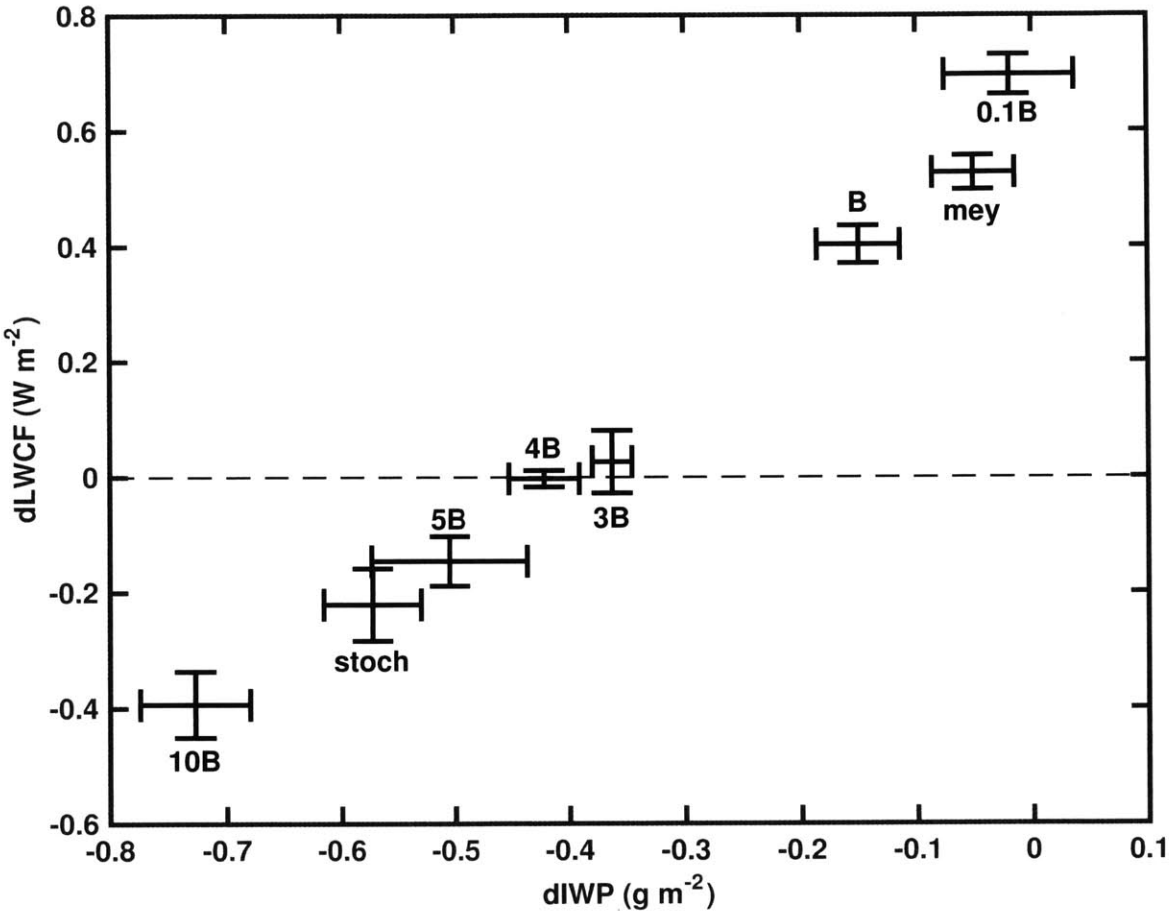

Figure B-21: Scatter plot of $dLWCF$ vs. $dIWP$ for all cases. Error bars show uncertainty estimates from bootstrapping two-year averages from the final five years of the six-year simulation (i.e. bootstrapped samples are constructed from years 2+3, 3+4, 4+5, and 5+6, and the mean and standard deviations of these samples are shown).

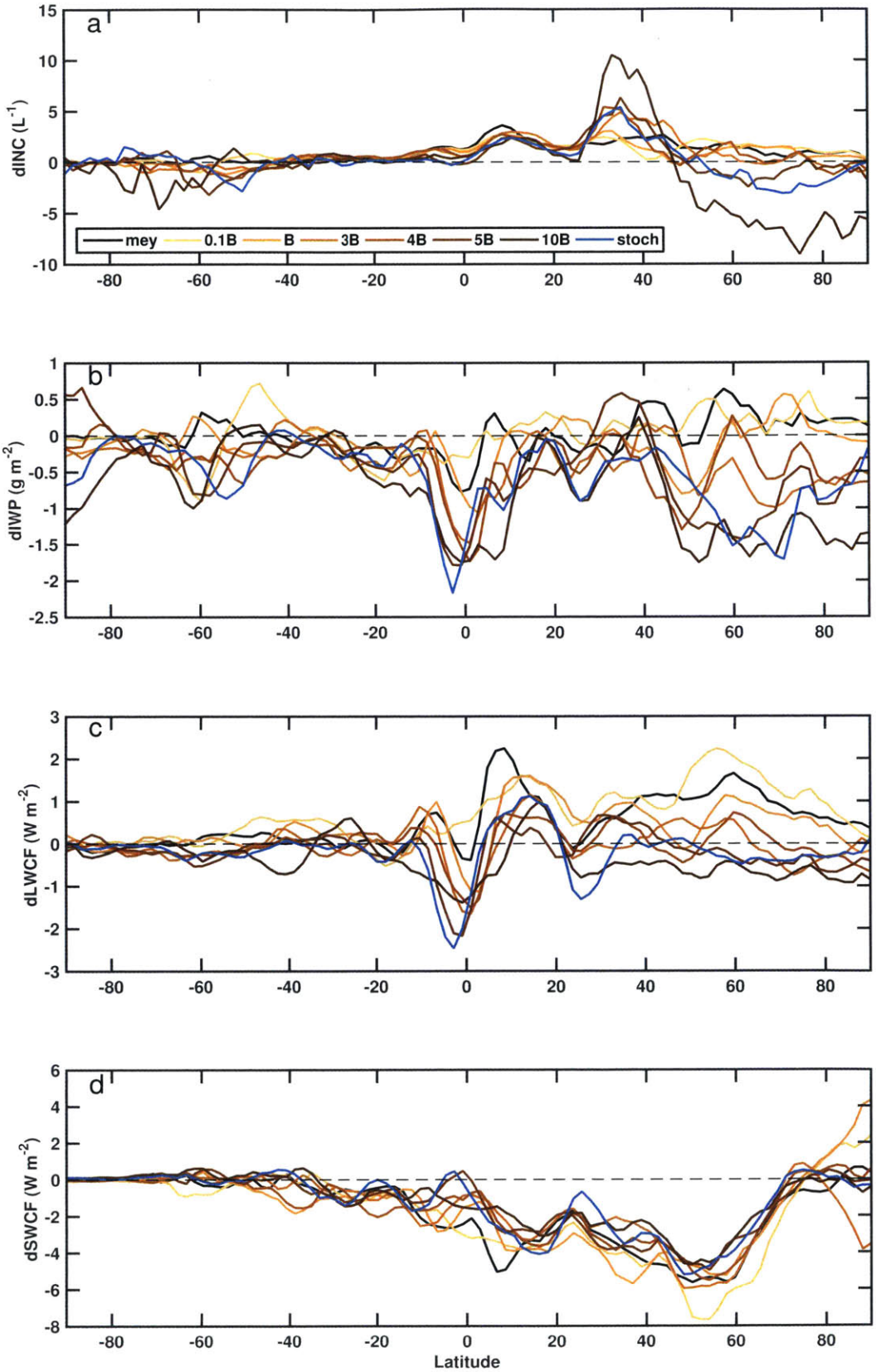

Figure B-22: Zonal averages of (a) $dINC$ (b) $dIWP$ (c) $dLWCF$ (d) $dSWCF$ for all cases.

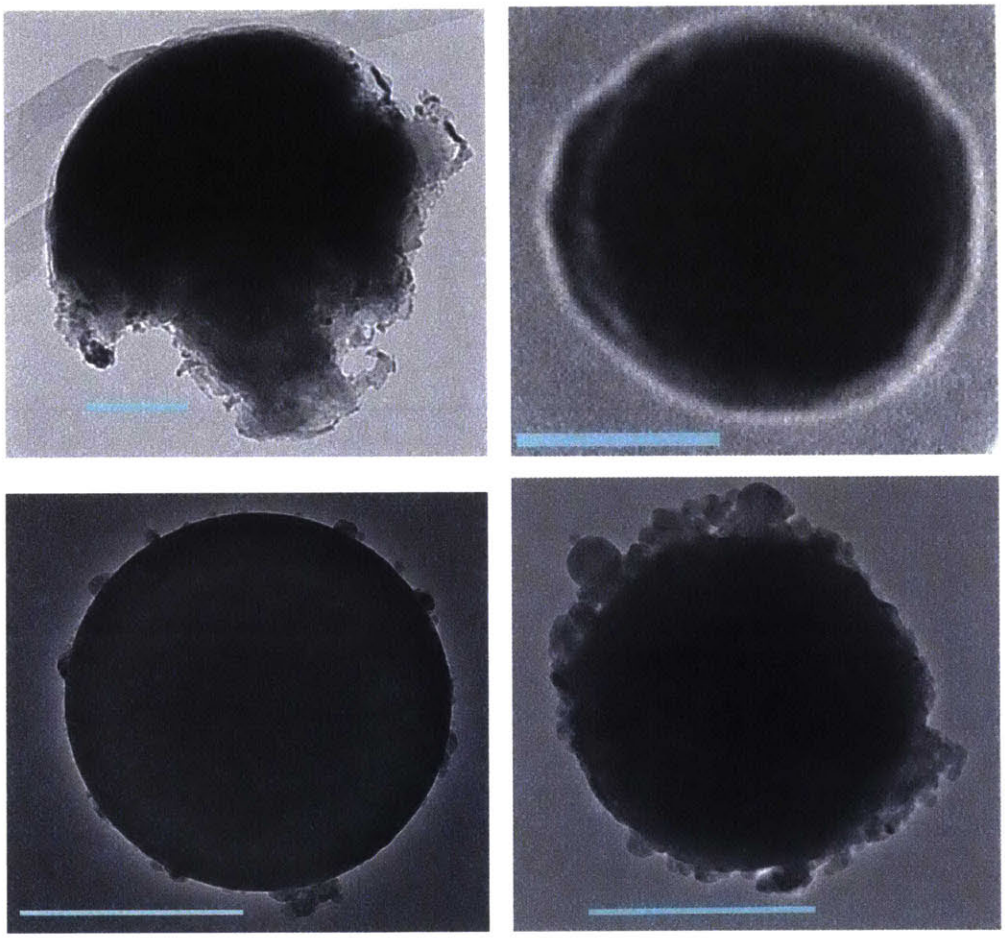

Figure B-23: (Top row): spherical mineral/metallic particles observed on EM grids collected during the MACPEX campaign (blue bar shows 500 nm for scale). (Bottom row): example fly ash particles observed using EM (blue bar shows 500 nm for scale).

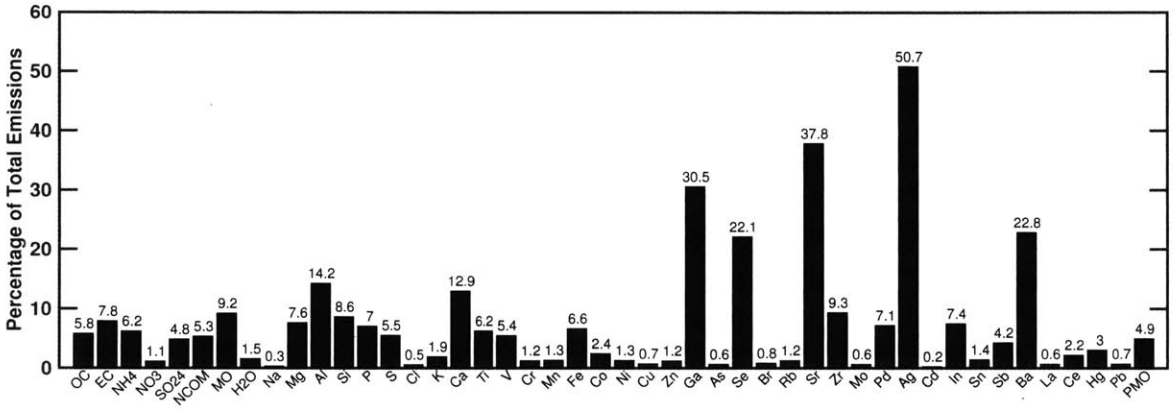

Figure B-24: Contribution of coal combustion to PM 2.5 emissions in the US using speciated emissions data from Reff et al. (2009).

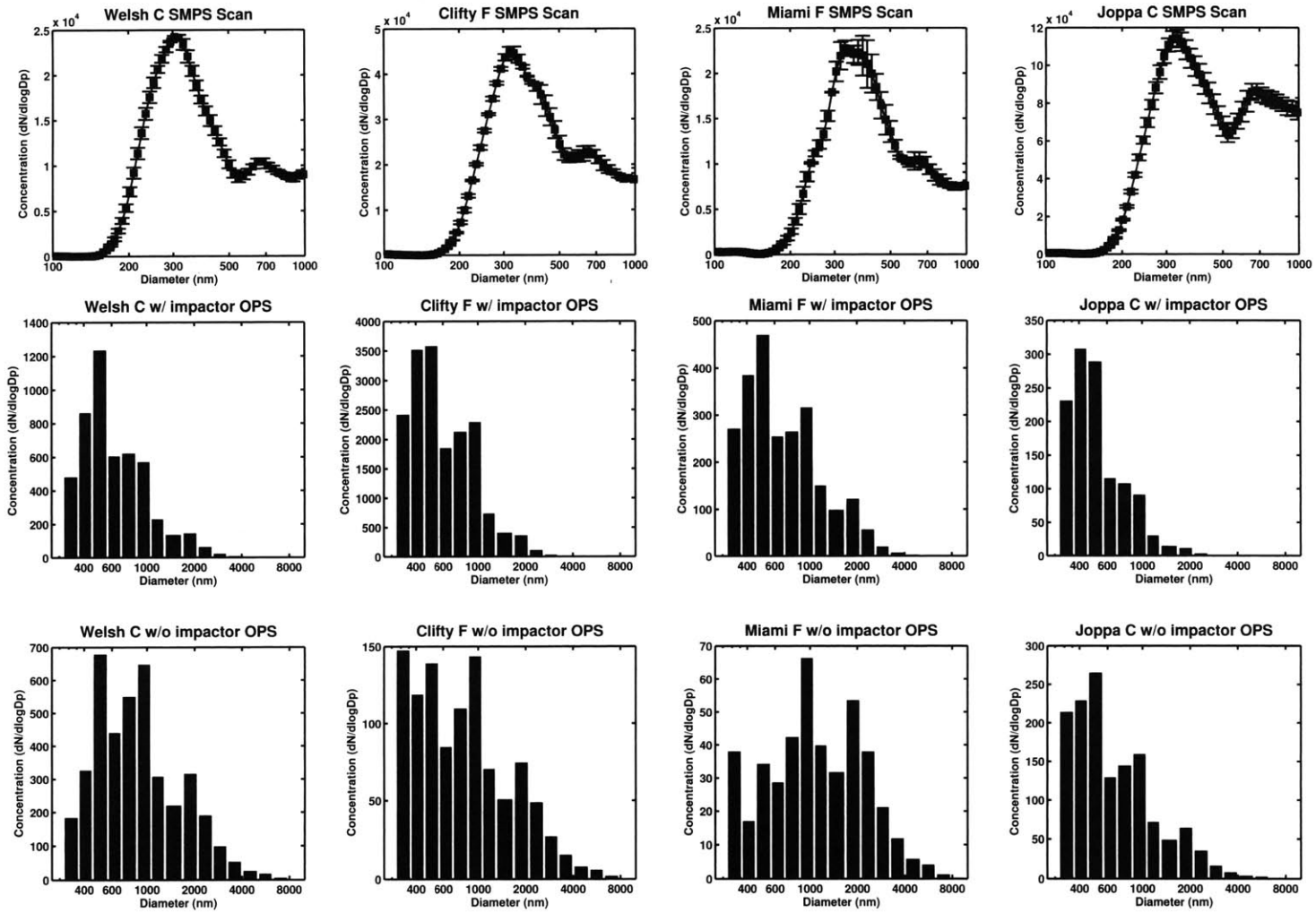

Figure B-25: Fly ash size distributions. (Top row): SMPS distributions measured with the Brechtel SEMS, which includes an upstream 650 nm traditional impactor. (Middle row): optical size distributions after impaction measured with the TSI OPS. (Bottom row): optical size distributions without impaction measured with the TSI OPS.

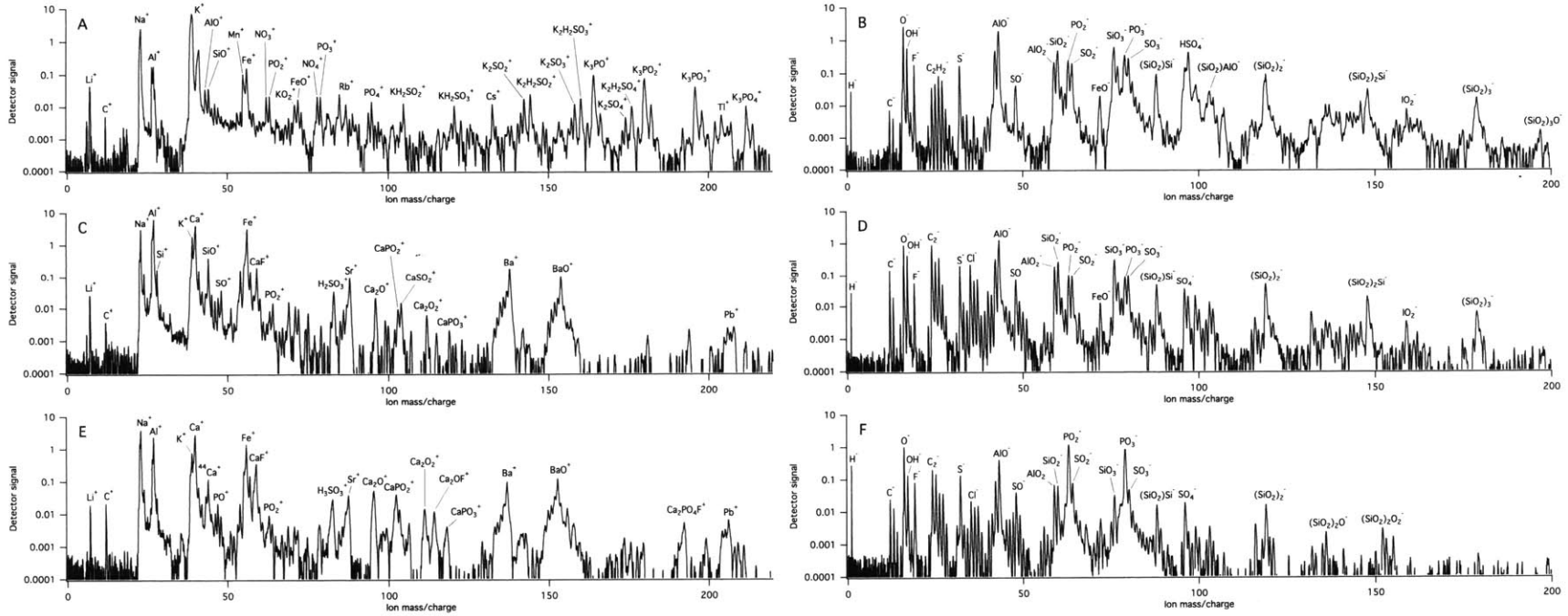

Figure B-26: Typical fly ash mass spectra collected with PALMS. (a) Miami F positive spectrum. (b) Miami F negative spectrum. (c) Clifty F positive spectrum. (d) Clifty F negative spectrum. (e) Welsh C positive spectrum. (f) Welsh C negative spectrum. The C type fly ash spectra were similar between samples, so only the Welsh C is shown.

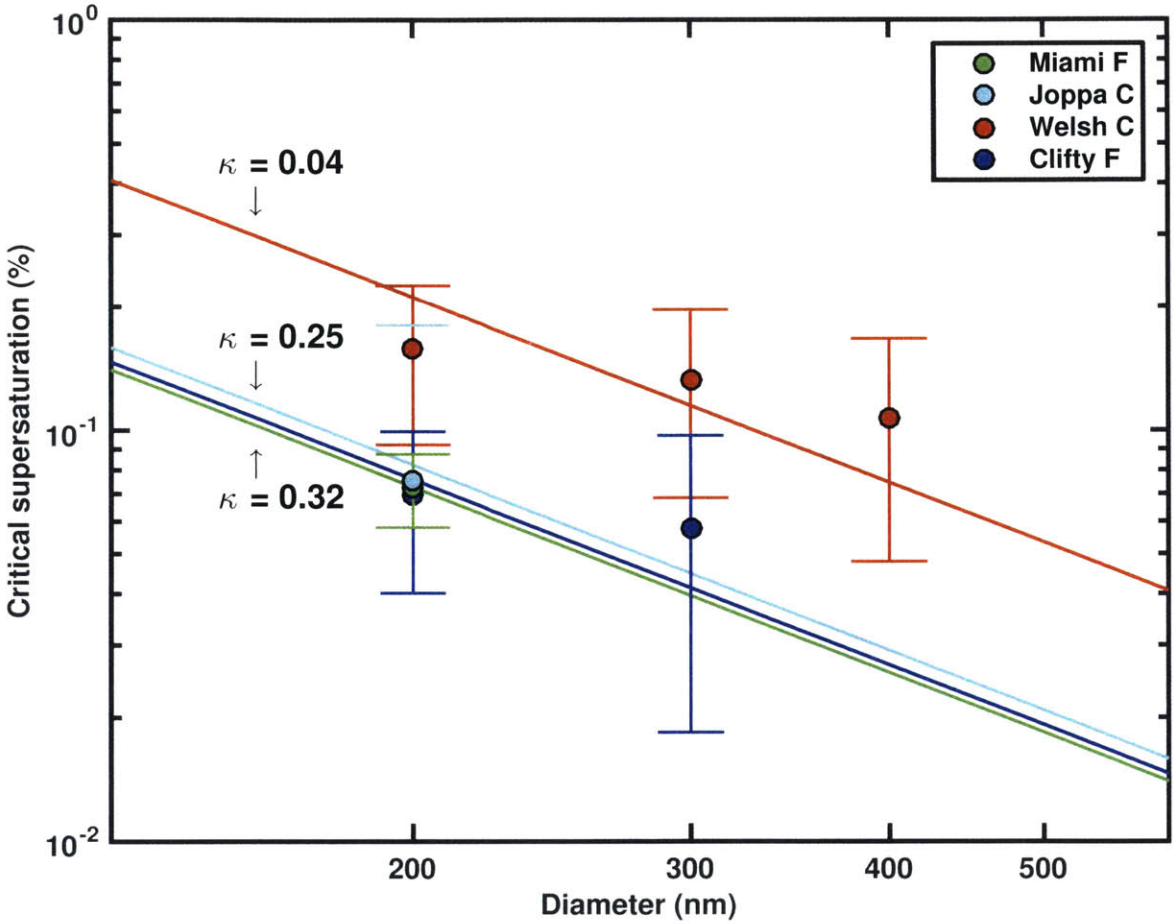

Figure B-27: Critical supersaturations (50% activation fraction) vs. mobility-selected diameter for the droplet activation experiments. Solid lines are fitted lines of constant kappa for each fly ash type, with indicated values. Error bars show the standard deviations of the measured values across experiments.

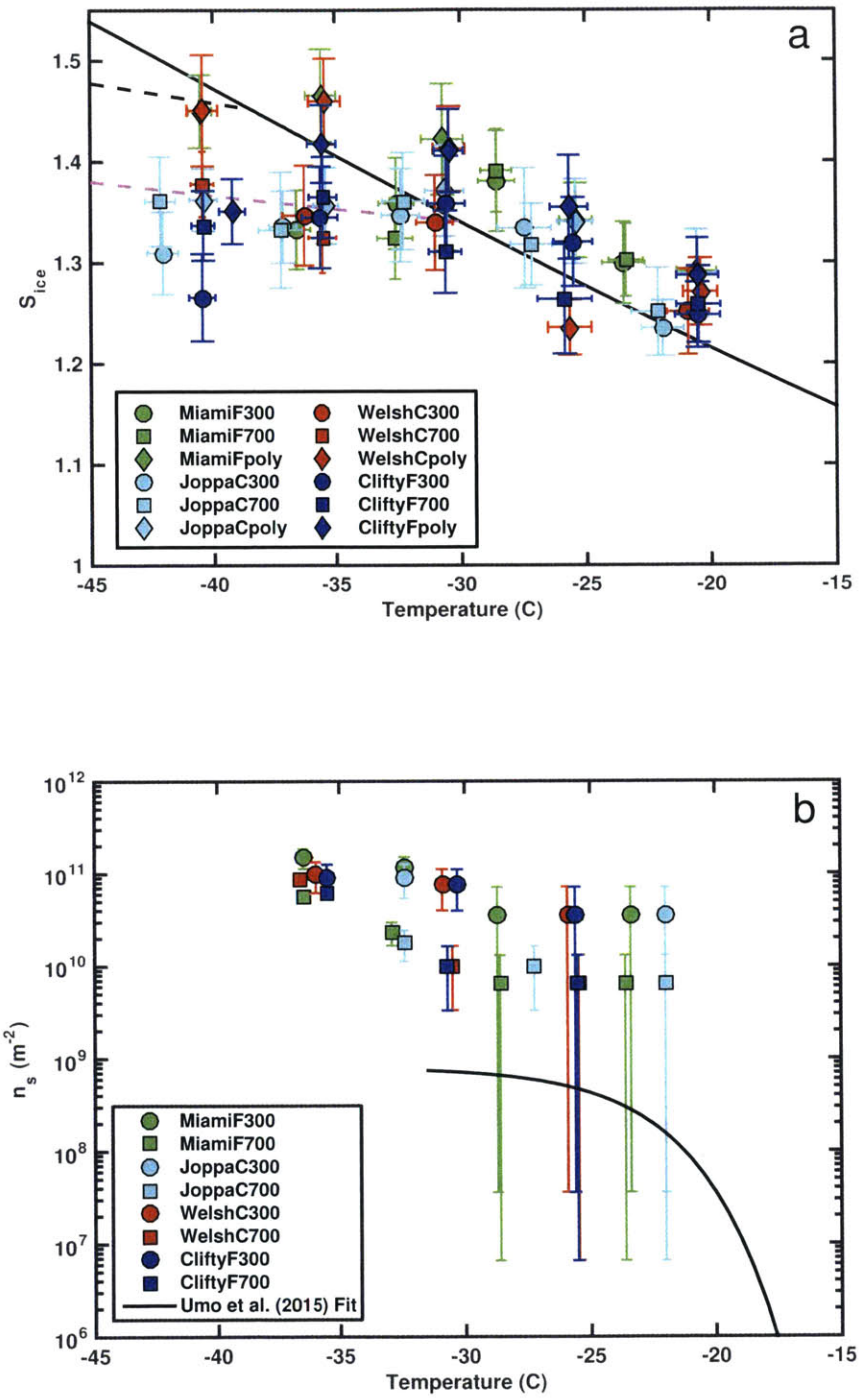

Figure B-28: (a) 1% activated ice fraction from SPIN experiments. The solid black line is the water saturation level, the dashed black line shows the homogeneous freezing level predicted by Koop et al. (2000), and the dashed magenta line is a CNT fit to the deposition freezing data based on the formulation by Detwiler and Vonnegut (1981). (b) INAS density vs. temperature for the immersion freezing data. The black line shows the empirical fit to immersion freezing data reported by Umo et al. (2015).

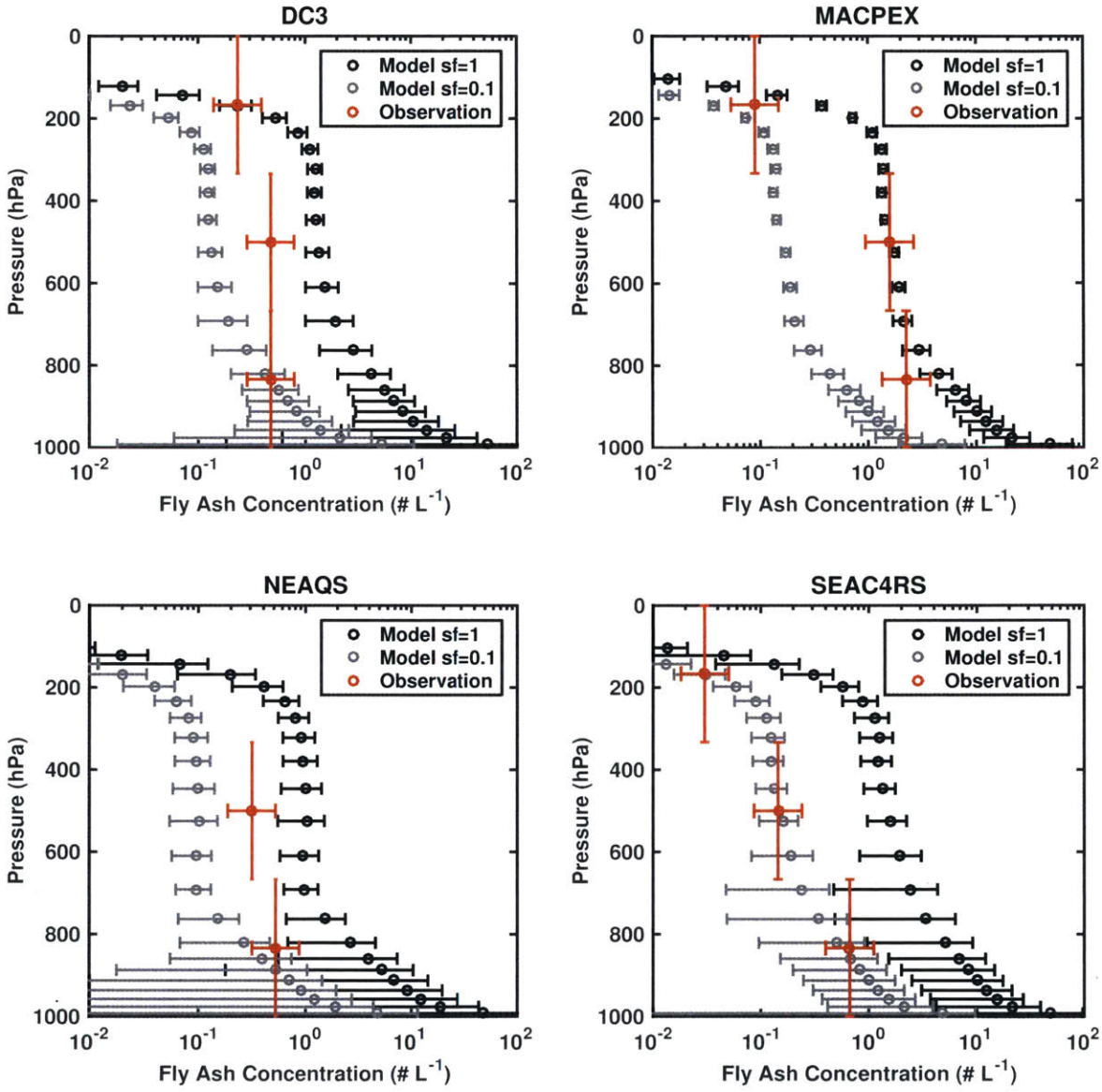

Figure B-29: Vertical profiles of fly ash concentrations from aircraft campaigns and diagnosed fly ash concentrations from collocated annual mean CAM5-MARC BC fields. Horizontal error bars on aircraft data show the range in uncertainty associated with the Bayesian estimate, and vertical error bars correspond to the 1000-700, 700-500, and 500-0 hPa pressure bins. The errors bars on the model results indicate spatial variability in concentration in the model across the latitude and longitude extent of the aircraft data.

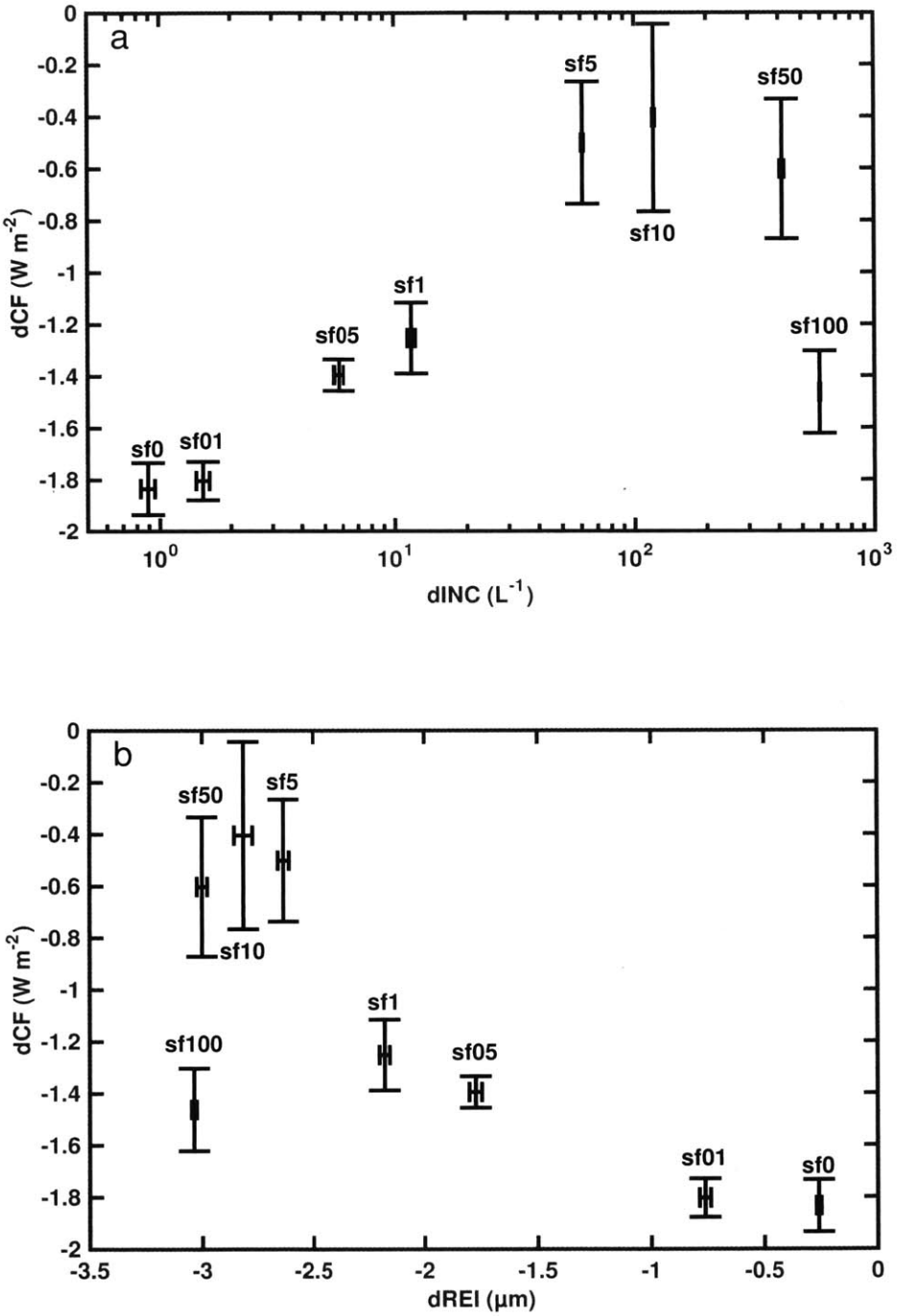

Figure B-30: dCF responses to changes in $dINC$ (a) and $dREI$ (b) for all cases. Horizontal and vertical error bars in both panels show uncertainty estimates from bootstrapping two-year averages from the final five years of the six-year simulation (i.e. bootstrapped samples are constructed from years 2+3, 3+4, 4+5, and 5+6, and the mean and standard deviations of these samples are shown).

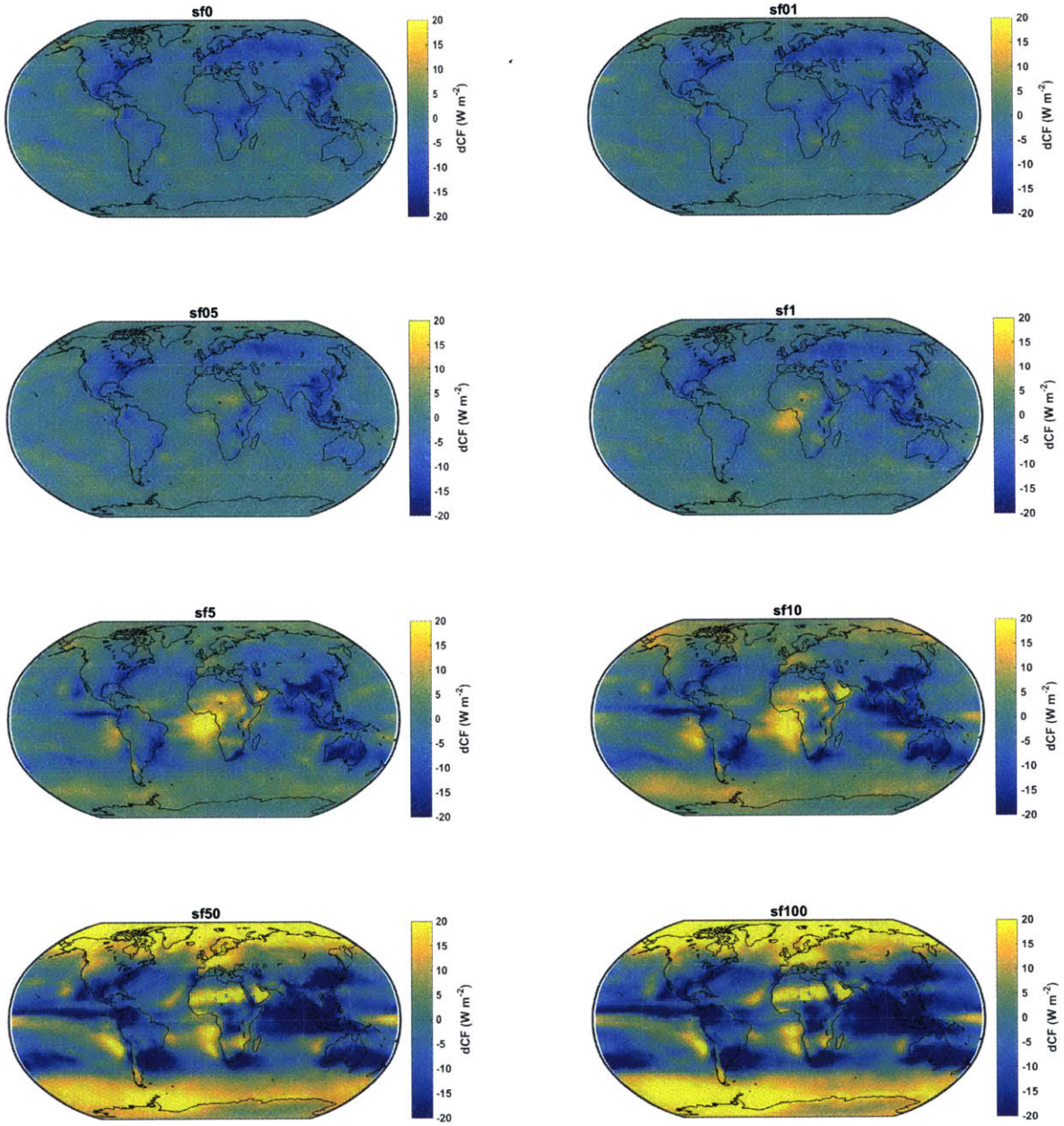

Figure B-31: Global maps of dCF for all cases.

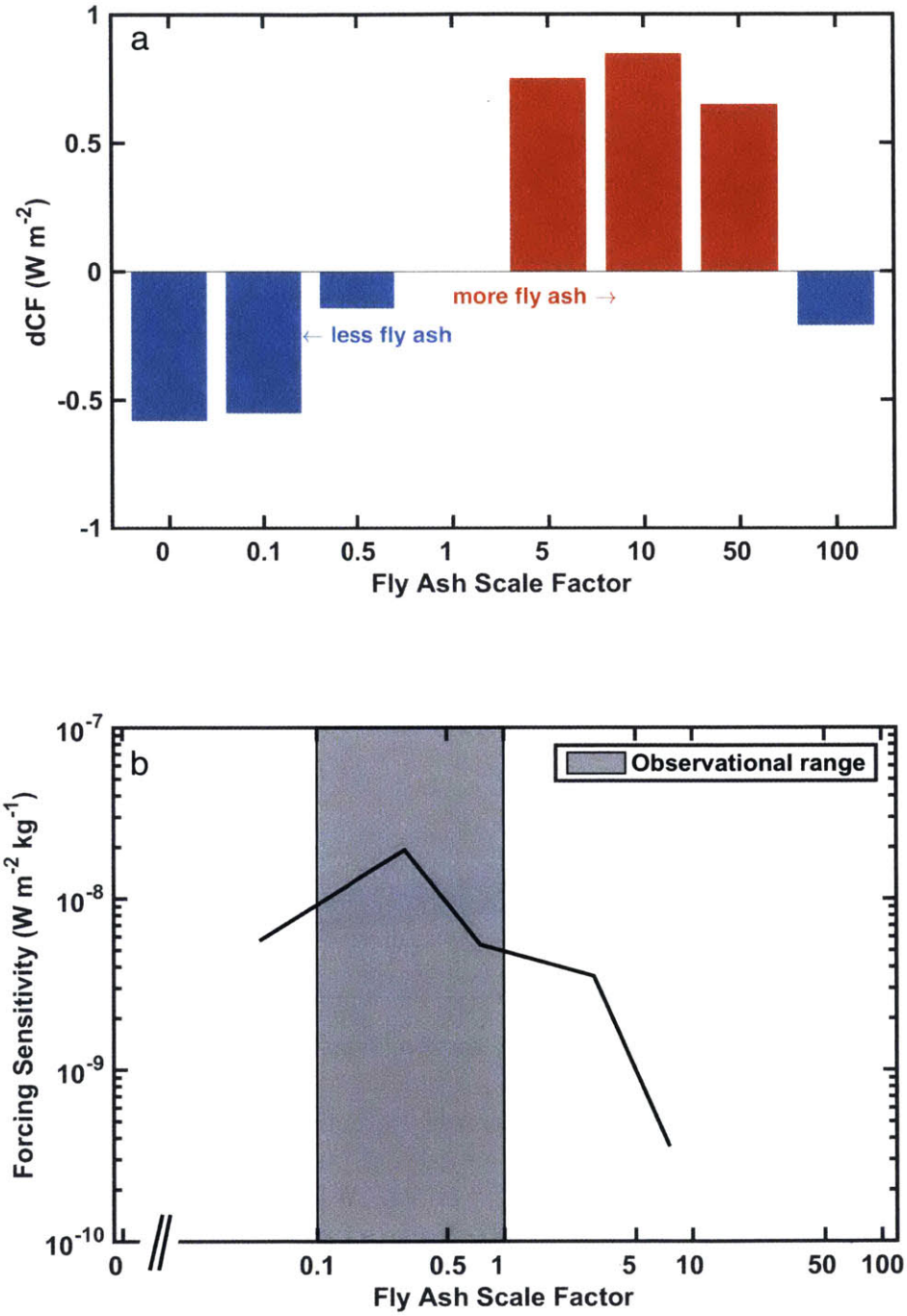

Figure B-32: (a) Cloud forcing response to amount of fly ash emissions. Red bars indicate a net warming effect compared to the $sf = 1$ case, and blue bars indicate a net cooling. (b) Sensitivity of changes in cloud forcing response to changes in fly ash emissions as a function of fly ash emissions. The grey shaded region shows emissions range constrained by field observations.

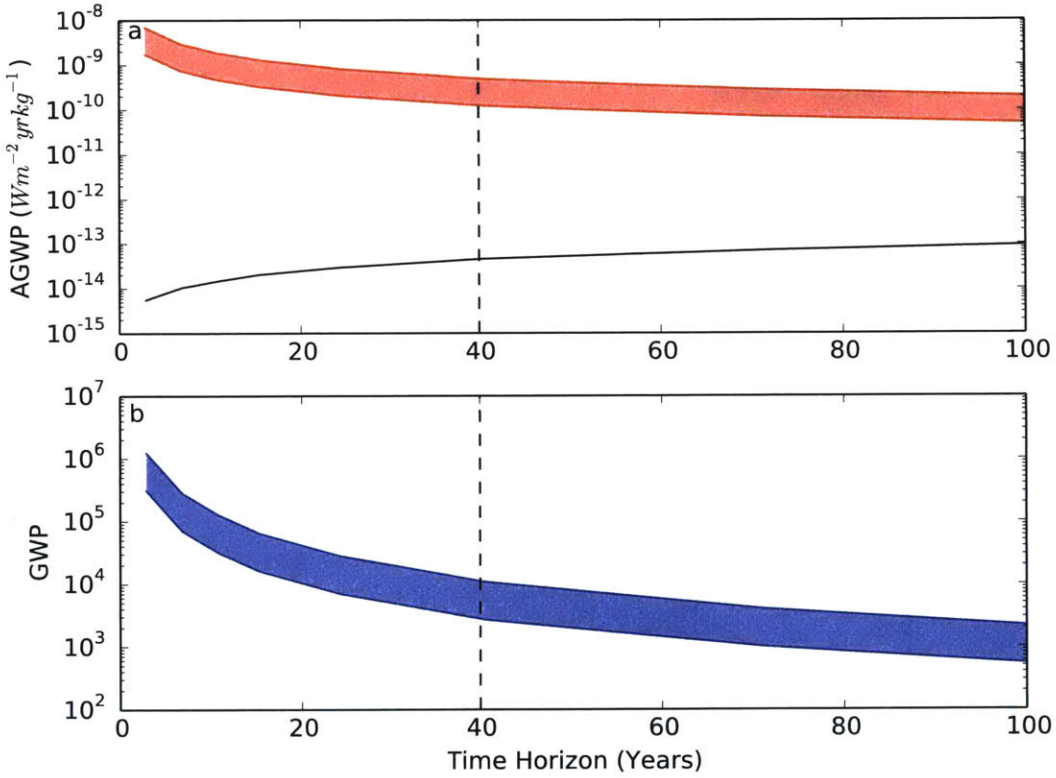

Figure B-33: (a) Absolute Global Warming Potential (AGWP) for continuous (unmitigated) fly ash emissions (red) and a one-year pulse of CO_2 (black, Stocker et al., 2013) as a function of time horizon. (b) Global Warming Potential for unmitigated fly ash emissions ($AGWP_{flyash}$ / $AGWP_{CO_2}$) as a function of time horizon. A 40 year time horizon corresponds to the average life of a power plant (EPA, 2016).

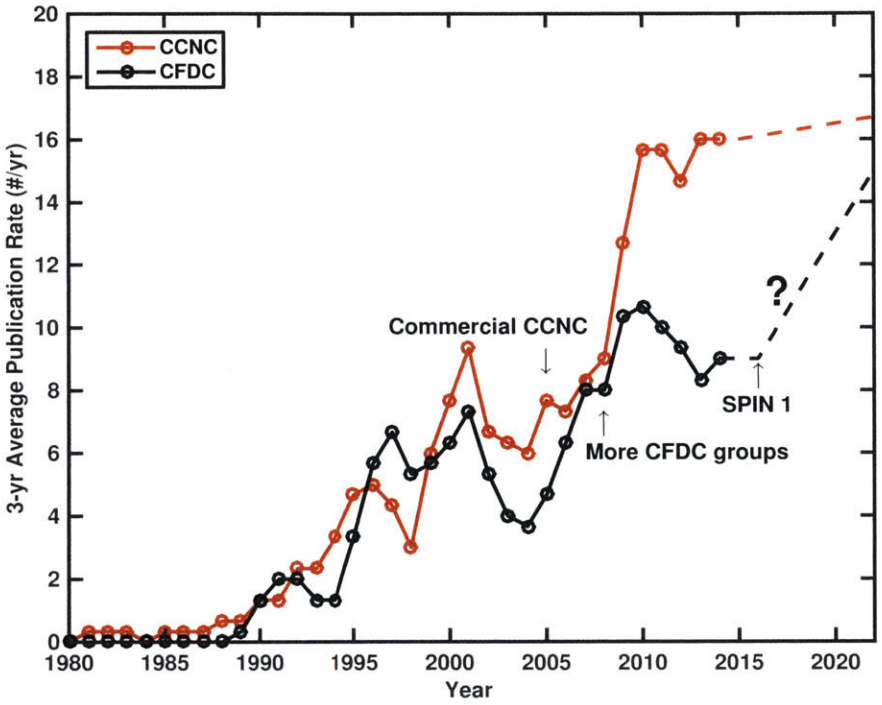

Figure B-34: Time series of 3-year average publication rate for papers with a CCNC topic (red) and with a CFDC topic (black). Arrows indicate the year of introduction of a commercial CCNC (Roberts and Nenes, 2005), the beginning of the use of CFDC-style chambers by multiple research groups (Stetzer et al., 2008), and the introduction of the first SPIN chamber (Chapter 2). See Section 5.1 for details.

Appendix C

References

Abbatt, J. P. D., Benz, S., Cziczo, D. J., Kanji, Z., Lohmann, U., and Möhler, O.: Solid Ammonium Sulfate Aerosols as Ice Nuclei: A Pathway for Cirrus Cloud Formation, Science, 313(5794), 1770-1773, doi:10.1126/science.1129726, 2006.

Ahern, H. E., Walsh, K. A., Hill, T. C. J., and Moffett, B. F.: Fluorescent pseudomonads isolated from Hebridean cloud and rain water produce biosurfactants but do not cause ice nucleation, Biogeosciences, 4, 115-124, doi:10.5194/bg-4-115-2007, 2007.

Ahmaruzzaman, M.: A review on the utilization of fly ash. Prog. Energ. Combust., 36, 327-363, doi:10.1016/j.pecs.2009.11.003, 2009.

Amato, P., Joly, M., Schaupp, C., Attard, E., Möhler, O., Morris, C. E., Brunet, Y., and Delort, A.-M.: Survival and ice nucleation activity of bacteria as aerosols in a cloud simulation chamber, Atmos. Chem. Phys., 15, 6455-6465, doi:10.5194/acp-15-6455-2015, 2015.

Archuleta, C. M., DeMott, P. J., and Kreidenweis, S. M.: Ice nucleation by surrogates for atmospheric mineral dust and mineral dust/sulfate particles at cirrus temperatures, Atmos. Chem. Phys., 5, 2617-2634, doi:10.5194/acp-5-2617-2005, 2005.

Azar, C. and Johansson, D.: On the relationship between metrics to compare greenhouse gases - the case of IGTP, GWP and SGTP, Earth Syst. Dynam. Discuss., 3(1), 113-141, doi:10.5194/esdd-3-113-2012, 2012.

Bailey, M. and Hallett, J.: Nucleation effects on the habit of vapour grown ice crystals from -18 to -42 °C, Q. J. Roy. Meteor. Soc., 128, 1461-1483, doi:10.1256/00359000260247318, 2002.

Barth, M., Cantrell, C., Brune, W., Rutledge, S., Crawford, J., Huntrieser, H., Carey, L., MacGorman, D., Weisman, M., Pickering, K., Bruning, E., Anderson, B., Apel, E., Biggerstaff, M., Campos, T., Campuzano-Jost, P., Cohen, R., Crounse, J., Day, D., Diskin, G., Flocke, F., Fried, A., Garland, C., Heikes, B., Honomichl, S., Hornbrook, R., Huey, L., Jimenez, J., Lang, T., Lichtenstern, M., Mikoviny, T., Nault, B., O'Sullivan, D., Pan, L., Peischl, J., Pollack, I., Richter, D.,

Riemer, D., Ryerson, T., Schlager, H., St. Clair, J., Walega, J., Weibring, P., Weinheimer, A., Wennberg, P., Wisthaler, A., Wooldridge, P. and Ziegler, C.: The Deep Convective Clouds and Chemistry (DC3) Field Campaign, Bull. Amer. Meteor. Soc., 96(8), 1281-1309, doi:10.1175/bams-d-13-00290.1, 2015.

Block, C. and Dams, R.: Study of fly ash emission during combustion of coal, Environmental Science & Technology, 10(10), 1011-1017, doi:10.1021/es60121a013, 1976.

Boose, Y., Sierau, B., García, M. I., Rodríguez, S., Alastuey, A., Linke, C., Schnaiter, M., Kupiszewski, P., Kanji, Z. A., and Lohmann, U.: Ice nucleating particles in the Saharan Air Layer, Atmos. Chem. Phys. Discuss., doi:10.5194/acp-2016-192, in review, 2016.

Boucher, O., Randall, D., Artaxo, P., Bretherton, C., Feingold, G., Forster, P., Kerminen, V.-M., Kondo, Y., Liao, H., Lohmann, U., Rasch, P., Satheesh, S., Sherwood, S., Stevens, B., and Zhang, X.: Clouds and aerosols, in: Climate Change 2013: The Physical Science Basis, Working Group I Contribution to the Fifth Assessment Report of the Intergovernmental Panel on Climate Change, Cambridge, United Kingdom and New York, NY, USA, 571-657, 2013.

Breiman, L.: Random Forests, Mach. Learn. 45, 5-32, doi: 10.1023/A:1010933404324, 2001.

Charlson, R. J., Schwartz, S. E., Hales, J. M., Cess, R. D., Coakley, J. A., Hansen, J. E., and Hofmann, D. J.: Climate forcing by anthropogenic aerosols, Science, 255, 423-430, doi:10.1126/science.255.5043.423, 1992.

Chen, Y. L., Kreidenweis, S. M., McInnes, L. M., Rogers, D. C., and DeMott, P. J.: Single particle analyses of ice nucleating aerosols in the upper troposphere and lower stratosphere, Geophys. Res. Lett., 25, 1391-1394, 10.1029/97gl03261, 1998.

Chen, Y., DeMott, P., Kreidenweis, S., Rogers, D. and Sherman, D.: Ice Formation by Sulfate and Sulfuric Acid Aerosol Particles under Upper-Tropospheric Conditions, J. Atmos. Sci., 57(22), 3752-3766, doi:10.1175/1520-0469(2000)057<3752:ifbsas>2.0.co;2, 2000.

Chernoff, D. I. and Bertram, A. K.: Effects of sulfate coatings on the ice nucleation properties of a biological ice nucleus and several types of minerals, J. Geophys. Res., 115, D20205, doi:10.1029/2010JD014254, 2010.

Chou, C., Stetzer, O., Weingartner, E., Juranyi, Z., Kanji, Z. A., and Lohmann, U.: Ice nuclei properties within a Saharan dust event at the Jungfraujoch in the Swiss Alps, Atmos. Chem. Phys., 11, 4725-4738, 10.5194/acp-11-4725-2011, 2011.

Chou, C., Kanji, Z. A., Stetzer, O., Tritscher, T., Chirico, R., Heringa, M. F., Weingartner, E., Prevot, A. S. H., Baltensperger, U., and Lohmann, U.: Effect of photochemical ageing on the ice nucleation properties of diesel and wood burning particles, Atmos. Chem. Phys., 13, 761-772, 10.5194/acp-13-761-2013, 2013.

Clauss, T., A. Kiselev, S. Hartmann, S. Augustin, S. Pfeifer, D. Niedermeier, H. Wex, and F. Stratmann: Application of linear polarized light for the discrimination of frozen and liquid droplets in ice nucleation experiments, Atmos. Meas. Tech., 6, 1041-1052, doi:10.5194/amt-6-1041-2013, 2013.

Connolly, P. J., Möhler, O., Field, P. R., Saathoff, H., Burgess, R., Choularton, T., and Gallagher, M.: Studies of heterogeneous freezing by three different desert dust samples, Atmos. Chem. Phys., 9, 2805-2824, doi:10.5194/acp-9-2805-2009, 2009.

Crawford, I., Möhler, O., Schnaiter, M., Saathoff, H., Liu, D., McMeeking, G., Linke, C., Flynn, M., Bower, K. N., Connolly, P. J., Gallagher, M. W., and Coe, H.: Studies of propane flame soot acting as heterogeneous ice nuclei in conjunction with single particle soot photometer measurements, Atmos. Chem. Phys., 11, 9549-9561, doi:10.5194/acp-11-9549-2011, 2011.

Cziczo, D. and Abbatt, J.: Deliquescence, efflorescence, and supercooling of ammonium sulfate aerosols at low temperature: Implications for cirrus cloud formation and aerosol phase in the atmosphere, Journal of Geophysical Research: Atmospheres, 104(D11), 13781-13790, doi:10.1029/1999jd900112, 1999.

Cziczo, D. J., Thomson D. S., Thompson T. L., DeMott P. J., and Murphy D. M.: Particle analysis by laser mass spectrometry (PALMS) studies of ice nuclei and other low number density particles, Int. J. Mass Spectrom., 258, 21-29, doi:10.1016/j.ijms.2006.05.013, 2006.

Cziczo, D. J., Froyd, K. D., Gallavardin, S. J., Moehler, O., Benz, S., Saathoff, H., and Murphy, D. M.: Deactivation of ice nuclei due to atmospherically relevant surface coatings, Environ. Res. Lett., 4, 044013, doi:10.1088/1748-9326/4/4/044013, 2009a.

Cziczo, D. J., Stetzer, O., Worringen, A., Ebert, M., Weinbruch, S., Kamphus, M., Gallavardin, S. J., Curtius, J., Borrmann, S., Froyd, K. D., Mertes, S., Moehler, O., and Lohmann, U.: Inadvertent climate modification due to anthropogenic lead, Nat. Geosci., 2, 333-336, doi:10.1038/ngeo499, 2009b.

Cziczo, D. J., Froyd, K. D., Hoose, C., Jensen, E. J., Diao, M., Zondlo, M. A., Smith, J. B., Twohy, C. H., and Murphy, D. M.: Clarifying the dominant sources and mechanisms of cirrus cloud formation, Science, 340, 1320-1324, DOI: 10.1126/science.1234145, 2013a.

Cziczo, D., Garimella, S., Raddatz, M., Hoehler, K., Schnaiter, M., Saathoff, H., Moehler, O., Abbatt, J. and Ladino, L.: Ice nucleation by surrogates of Martian mineral dust: What can we learn about Mars without leaving Earth?, J. Geophys. Res. Planets, 118(9), 1945-1954, doi:10.1002/jgre.20155, 2013b.

Damle, A., Ensor, D. and Ranade, M.: Coal Combustion Aerosol Formation Mechanisms: A Review, Aerosol Science and Technology, 1(1), 119-133, doi:10.1080/02786828208958582, 1981.

Davison, R. L., Natusch, D. F. S., Wallace, J. R., and Evans, C. A.: TRACE-ELEMENTS IN FLY ASH - DEPENDENCE OF CONCENTRATION ON PARTICLE-SIZE, Environ. Sci. Tech., 8, 1107-1113, doi:10.1021/es60098a003, 1974.

Demirdjian, B., Ferry, D., Suzanne, J., Popovicheva, O. B., Persiantseva, N. M., Kamaev, A. V., Shonija, N. K., and Zubareva, N. A.: Freezing of water adsorbed on hydrophobic and activated soot particles, Chem. Phys. Lett., 480, 247-252, 2009.

DeMott, P. J., Cziczo, D. J., Prenni, A. J., Murphy, D. M., Kreidenweis, S. M., Thomson, D. S., Borys, R., and Rogers, D. C.: Measurements of the concentration and composition of nuclei for cirrus formation, P. Natl. Acad. Sci. USA, 100, 14655-14660, 10.1073/pnas.2532677100, 2003a.

DeMott, P. J., Sassen, K., Poellot, M. R., Baumgardner, D., Rogers, D. C., Brooks, S. D., Prenni, A. J., and Kreidenweis, S. M.: African dust aerosols as atmospheric ice nuclei, Geophys. Res. Lett., 30, 10.1029/2003gl017410, 2003b.

DeMott, P.J., Prenni, A. J., Liu, X., Petters, M. D., Twohy, C. H., Richardson, M. S., Eidhammer, T., Kreidenweis, S. M., and Rogers, D. C.: Predicting global atmospheric ice nuclei distributions and their impacts on climate, P. Natl. Acad. Sci. USA, 107, 11217-11222, doi: 10.1073/pnas.0910818107, 2010.

DeMott, P. J., Prenni, A. J., McMeeking, G. R., Sullivan, R. C., Petters, M. D., Tobo, Y., Niemand, M., Möhler, O., Snider, J. R., Wang, Z., and Kreidenweis, S. M.: Integrating laboratory and field data to quantify the immersion freezing ice nucleation activity of mineral dust particles, Atmos. Chem. Phys., 15, 393-409, doi:10.5194/acp-15-393-2015, 2015.

Detwiler, A. G. and Vonnegut, B.: Humidity required for ice nucleation from the vapor onto silver iodide and lead iodide aerosols over the temperature range -6 to -67 °C, J. Appl. Meteorol., 20, 1006-1012, doi:10.1175/1520-0450(1981)020<1006:HRFINF>2.0.CO;2, 1981.

Dusek, U., Frank, G., Hildebrandt, L., Curtius, J., Schneider, J., Walter, S., Chand, D., Drewnick, F., Hings, S., Jung, D., Borrmann, S. and Andreae, M.: Size Matters More Than Chemistry for Cloud-Nucleating Ability of Aerosol Particles, Science, 312(5778), 1375-1378, doi:10.1126/science.1125261, 2006.

Dymarska, M., Murray, B., Sun, L., Eastwood, M., Knopf, D. and Bertram, A.: Deposition ice nucleation on soot at temperatures relevant for the lower troposphere, J. Geophys. Res., 111(D4), doi:10.1029/2005jd006627, 2006.

Ebert, M., Worringen, A., Benker, N., Mertes, S., Weingartner, E., and Weinbruch, S.: Chemical composition and mixing-state of ice residuals sampled within mixed phase clouds, Atmos. Chem. Phys., 11, 2805-2816, doi:10.5194/acp-11-2805-2011, 2011.

Eidhammer, T., DeMott, P. and Kreidenweis, S.: A comparison of heterogeneous ice nucleation parameterizations using a parcel model framework, J. Geophys. Res., 114(D6), doi:10.1029/2008jd011095, 2009.

EPA FACT SHEET: Clean Power Plan | Clean Power Plan | US EPA, epa.gov [online] Available from: https://www.epa.gov/cleanpowerplan/fact-sheet-clean-power-plan, 2016.

Fan, J., Leung, L. R., DeMott, P. J., Comstock, J. M., Singh, B., Rosenfeld, D., Tomlinson, J. M., White, A., Prather, K. A., Minnis, P., Ayers, J. K., and Min, Q.: Aerosol impacts on California winter clouds and precipitation during CalWater 2011: local pollution versus long-range transported dust, Atmos. Chem. Phys., 14, 81-101, doi:10.5194/acp-14-81-2014, 2014.

Fluent 16.0 User's Guide. ANSYS Inc., Cecil Township, PA, USA, 2015.

Friedman, B., Zelenyuk, A., Beranek, J., Kulkarni, G., Pekour, M., Hallar, A. G., McCubbin, I. B., Thornton, J. A., and Cziczo, D. J.: Aerosol measurements at

a high-elevation site: composition, size, and cloud condensation nuclei activity, Atmos. Chem. Phys., 13, 11839-11851, 10.5194/acp-13-11839-2013, 2013.

Froyd, K. D., Murphy, D. M., Lawson, P., Baumgardner, D., and Herman, R. L.: Aerosols that form subvisible cirrus at the tropical tropopause, Atmos. Chem. Phys., 10, 209-218, doi:10.5194/acp-10-209-2010, 2010.

Gallavardin, S., Froyd, K., Lohmann, U., Moehler, O., Murphy, D. and Cziczo, D.: Single Particle Laser Mass Spectrometry Applied to Differential Ice Nucleation Experiments at the AIDA Chamber, Aerosol Science and Technology, 42(9), 773-791, doi:10.1080/02786820802339538, 2008.

Garimella, S., Huang, Y.-W., Seewald, J. S., and Cziczo, D. J.: Cloud condensation nucleus activity comparison of dry- and wet-generated mineral dust aerosol: the significance of soluble material, Atmos. Chem. Phys., 14, 6003-6019, doi:10.5194/acp-14-6003-2014, 2014.

Garimella, S., Voigtländer, J., Kulkarni, G., Stratmann, F., and Cziczo, D. J.: Biases in field measurements of ice nuclei concentrations, AGU Fall Meeting, 2015.

Garrett, T., Radke, L. and Hobbs, P.: Aerosol Effects on Cloud Emissivity and Surface Longwave Heating in the Arctic, J. Atmos. Sci., 59(3), 769-778, doi:10.1175/1520-0469(2002)059<0769:aeocea>2.0.co;2, 2002.

Garrett, T. and Zhao, C.: Increased Arctic cloud longwave emissivity associated with pollution from mid-latitudes, Nature, 440(7085), 787-789, doi:10.1038/ nature04636, 2006.

Gettelman, A., Liu, X., Barahona, D., Lohmann, U., and Chen, C. C.: Climate Impacts of Ice Nucleation, J. Geophys. Res., 117, D20201, doi:10.1029/2012JD01 7950, 2012.

Gettelman, A., Morrison, H., Santos, S., Bogenschutz, P. and Caldwell, P.: Advanced Two-Moment Bulk Microphysics for Global Models. Part II: Global Model Solutions and Aerosol-Cloud Interactions, Journal of Climate, 28(3), 1288-1307, doi:10.1175/jcli-d-14-00103.1, 2015.

Ghan, S. J.: Technical Note: Estimating aerosol effects on cloud radiative forcing, Atmos. Chem. Phys., 13, 9971-9974, doi:10.5194/acp-13-9971-2013, 2013.

Hande, L. B., Engler, C., Hoose, C., and Tegen, I.: Seasonal variability of Saharan desert dust and ice nucleating particles over Europe, Atmos. Chem. Phys., 15, 4389-4397, doi:10.5194/acp-15-4389-2015, 2015.

Haywood, J. M., Donner, L. J., Jones, A., and Golaz, J.-C.: Global indirect radiative forcing caused by aerosols: IPCC (2007) and beyond, in Clouds in the Perturbed Climate System, edited by J. Heintzenberg and R. J. Charlson, pp. 451-467, MIT Press, Cambridge, 2009.

Hoose, C. and Möhler, O.: Heterogeneous ice nucleation on atmospheric aerosols: a review of results from laboratory experiments, Atmos. Chem. Phys., 12, 9817-9854, doi:10.5194/acp-12-9817-2012, 2012.

Hung, H., Malinowski, A., and Martin, S. T.: Ice nucleation kinetics of aerosols containing aqueous and solid ammonium sulfate particles, J. Phys. Chem. A, 106, 293-306, 2002.

Hung, H., Malinowski, A., and Martin, S. T.: Kinetics of heterogeneous ice nucleation on the surfaces of mineral dust cores inserted into aqueous ammonium sulfate

particles, J. Phys. Chem. A, 107, 1296-1306, 2003.

Jaworek, A., Krupa, A. and Czech, T.: Modern electrostatic devices and methods for exhaust gas cleaning: A brief review, Journal of Electrostatics, 65(3), 133-155, doi:10.1016/j.elstat.2006.07.012, 2007.

Jones, H. M., Flynn, M. J., DeMott, P. J., and Möhler, O.: Manchester Ice Nucleus Counter (MINC) measurements from the 2007 International workshop on Comparing Ice nucleation Measuring Systems (ICIS-2007), Atmos. Chem. Phys., 11, 53-65, doi:10.5194/acp-11-53-2011, 2011.

JRC: Emission Database for Global Atmospheric Research (EDGAR), release version 4.2, European Commission: Joint Research Centre (JRC)/Netherlands Environmental Assessment Agency (PBL)., http://edgar.jrc.ec.europa.eu, 2011.

Kanji, Z. A., and Abbatt, J. P. D.: The University of Toronto Continuous Flow Diffusion Chamber (UT-CFDC): A Simple Design for Ice Nucleation Studies, Aerosol Sci. Tech., 43, 730-738, 10.1080/02786820902889861, 2009.

Kanji, Z. A., DeMott, P. J., Möhler, O., and Abbatt, J. P. D.: Results from the University of Toronto continuous flow diffusion chamber at ICIS 2007: instrument intercomparison and ice onsets for different aerosol types, Atmos. Chem. Phys., 11, 31-41,doi:10.5194/acp-11-31-2011, 2011.

Kanji, Z. A., Welti, A., Chou, C., Stetzer, O., and Lohmann, U.: Laboratory studies of immersion and deposition mode ice nucleation of ozone aged mineral dust particles, Atmos. Chem. Phys., 13, 9097-9118, 10.5194/acp-13-9097-2013, 2013.

Kim, D., Wang, C., Ekman, A., Barth, M. and Rasch, P.: Distribution and direct radiative forcing of carbonaceous and sulfate aerosols in an interactive size-resolving aerosol-climate model, J. Geophys. Res., 113, doi:10.1029/2007jd009756, 2008.

Kim, D., Wang, C., Ekman, A., Barth, M. and Lee, D.: The responses of cloudiness to the direct radiative effect of sulfate and carbonaceous aerosols, Journal of Geophysical Research: Atmospheres, 119, 1172-1185, doi:10.1002/2013jd020529, 2014.

Knopf, D., Wang, B., Laskin, A., Moffet, R. and Gilles, M.: Heterogeneous nucleation of ice on anthropogenic organic particles collected in Mexico City, Geophys. Res. Lett., 37(11), doi:10.1029/2010gl043362, 2010.

Knopf, D., Alpert, P., Wang, B., O'Brien, R., Kelly, S., Laskin, A., Gilles, M. and Moffet, R.: Microspectroscopic imaging and characterization of individually identified ice nucleating particles from a case field study, Journal of Geophysical Research: Atmospheres, 119(17), 10,365-10,381, doi:10.1002/2014jd021866, 2014.

Koop, T., Luo, B. P., Tsias, A., and Peter, T.: Water activity as the determinant for homogeneous ice nucleation in aqueous solutions, Nature, 406, 611-614, doi:10.1038/35020537, 2000.

Koop, T. and Zobrist, B.: Parameterizations for ice nucleation in biological and atmospheric systems, Phys. Chem. Chem. Phys., 11, 10839-10850, doi:10.1039/b914289d, 2009.

Kristan, M., Leonardis, A., and Skocaj, D.: Multivariate online kernel density estimation with Gaussian kernels, Pattern Recogn., 44, 2630-2642, 10.1016/j.patcog.

2011.03.019, 2011.

Kulkarni, G., Dobbie, S., and McQuaid, J. B.: A new thermal gradient ice nucleation diffusion chamber instrument: design, development and first results using Saharan mineral dust, Atmos. Meas. Tech., 2, 221-229, doi:10.5194/amt-2-221-2009, 2009.

Kulkarni, G., and Kok, G.: Mobile Ice Nucleus Spectrometer, Pacific Northwest National Laboratory, Richland, WA, 2012.

Kyoto Protocol, United Nations, Kyoto, Japan, 1999.

Kärcher, B. and Koop, T.: The role of organic aerosols in homogeneous ice formation, Atmospheric Chemistry and Physics, 5(3), 703-714, doi:10.5194/acp-5-703-2005, 2005.

Kärcher, B., Möhler, O., DeMott, P. J., Pechtl, S., and Yu, F.: Insights into the role of soot aerosols in cirrus cloud formation, Atmos. Chem. Phys., 7, 4203-4227, doi:10.5194/acp-7-4203-2007, 2007.

Koehler, K., DeMott, P., Kreidenweis, S., Popovicheva, O., Petters, M., Carrico, C., Kireeva, E., Khokhlova, T. and Shonija, N.: Cloud condensation nuclei and ice nucleation activity of hydrophobic and hydrophilic soot particles, Phys. Chem. Chem. Phys., 11(36), 7906, doi:10.1039/b905334b, 2009.

Lamarque, J. F., Bond, T. C., Eyring, V., Granier, C., Heil, A., Klimont, Z., Lee, D., Liousse, C., Mieville, A., Owen, B., Schultz, M. G., Shindell, D., Smith, S. J., Stehfest, E., Van Aardenne, J., Cooper, O. R., Kainuma, M., Mahowald, N., McConnell, J. R., Naik, V., Riahi, K., and van Vuuren, D. P.: Historical (1850-2000) gridded anthropogenic and biomass burning emissions of reactive gases and aerosols: methodology and application, Atmos. Chem. Phys.., 10, 7017-7039, doi:10.5194/acp-10-7017-2010, 2010.

Lance, S., Medina, J., Smith, J. N., and Nenes, A.: Mapping the operation of the DMT Continuous Flow CCN counter, Aerosol Sci. Tech., 40, 242-254, doi:10.1080/02786820500543290, 2006.

Lee, S. H., Sakai, E., Daimon, M., and Bang, W. K.: Characterization of fly ash directly collected from electrostatic precipitator, Cement Concrete Res, 29, 1791-1797, doi:10.1016/s0008-8846(99)00169-6, 1999.

Liou, K. N., and Lahore, H.: Laser Sensing of Cloud Composition - Backscattered Depolarization Technique, J. Appl. Meteorol., 13, 257-263, 10.1175/1520-0450(1974)013<0257:lsocca>2.0.co;2, 1974.

Liu, X. and Penner, J.: Ice nucleation parameterization for global models, Meteorologische Zeitschrift, 14(4), 499-514, doi:10.1127/0941-2948/2005/0059, 2005.

Loeb, N., Wielicki, B., Doelling, D., Smith, G., Keyes, D., Kato, S., Manalo-Smith, N. and Wong, T.: Toward Optimal Closure of the Earth's Top-of-Atmosphere Radiation Budget, Journal of Climate, 22(3), 748-766, doi:10.1175/2008jcli2637.1, 2009.

Lohmann, U. and Feichter, J.: Global indirect aerosol effects: a review, Atmos. Chem. Phys.., 5, 715-737, 2005.

Lohmann, U., Rotstayn, L., Storelvmo, T., Jones, A., Menon, S., Quaas, J., Ekman, A. M. L., Koch, D., and Ruedy, R.: Total aerosol effect: radiative forcing or radiative flux perturbation?, Atmos. Chem. Phys., 10, 3235-3246,

doi:10.5194/acp-10-3235-2010, 2010.
Lubin, D. and Vogelmann, A.: A climatologically significant aerosol longwave indirect effect in the Arctic, Nature, 439(7075), 453-456, doi:10.1038/nature04449, 2006.
Lynch, D.: Cirrus, Oxford University Press, Cambridge., 2002.
Lüönd, F., Stetzer, O., Welti, A., and Lohmann, U.: Experimental study on the ice nucleation ability of size-selected kaolinite particles in the immersion mode, J. Geophys. Res.-Atmos., 115, 10.1029/2009jd012959, 2010.
Mason, B., and van den Heuvel, A.: The Properties and Behavior of Some Artificial Ice Nuclei, Proc. Phys. Soc., 74, 744-755, DOI: 10.1088/0370-1328/74/6/312, 1958.
McLachlan, G. and Peel, D.: Finite mixture models, Wiley, New York, 2000.
Meyers, M. P., DeMott, P. J., and Cotton, W. R.: New primary ice nucleation parameterizations in an explicit cloud model, J. Appl. Meteor., 31, 708-721, 1992.
Mohri, M., Rostamizadeh, A., and Talwalkar, A.: Foundations of Machine Learning, MIT Press, Cambridge, MA, USA, 2012.
Murphy, D. M. and Thomson, D. S.: Laser ionization mass spectroscopy of single aerosol particles, Aerosol Sci. Tech., 22, 237- 249, doi:10.1080/02786829408959743, 1995.
Murray, B.: Inhibition of ice crystallisation in highly viscous aqueous organic acid droplets, Atmospheric Chemistry and Physics, 8(17), 5423-5433, doi:10.5194/acp-8-5423-2008, 2008.
Murray, B., Wilson, T., Dobbie, S., Cui, Z., Al-Jumur, S., Möhler, O., Schnaiter, M., Wagner, R., Benz, S., Niemand, M., Saathoff, H., Ebert, V., Wagner, S. and Kärcher, B.: Heterogeneous nucleation of ice particles on glassy aerosols under cirrus conditions, Nature Geoscience, 3(4), 233-237, doi:10.1038/ngeo817, 2010.
Mussatti, D. C.: EPA air pollution cost manual, U.S. Environmental Protection Agency, Office of Air Quality Planning and Standards, Research Triangle Park, NC, 2002.
Myhre, G., Shindell, D., Bréon, F.-M., Collins, W., Fuglestvedt, J., Huang, J., Koch, D., Lamarque, J.-F., Lee, D., Mendoza, B., Nakajima, T., Robock, A., Stephens, G., Takemura, T., and Zhang, H.: Anthropogenic and Natural Radiative Forcing. In: Climate Change 2013: The Physical Science Basis. Contribution of Working Group I to the Fifth Assessment Report of the Intergovernmental Panel on Climate Change. Cambridge, United Kingdom and New York, NY, USA, 659-740, 2013.
Möhler, O., Buttner, S., Linke, C., Schnaiter, M., Saathoff, H., Stetzer, O., Wagner, R., Kramer, M., Mangold, A., Ebert, V., and Schurath, U.: Effect of sulfuric acid coating on heterogeneous ice nucleation by soot aerosol particles, J. Geophys. Res., 110(D11), doi:10.1029/2004jd005169, 2005.
Möhler, O., Field, P. R., Connolly, P., Benz, S., Saathoff, H., Schnaiter, M., Wagner, R., Cotton, R., Krämer, M., Mangold, A., and Heymsfield, A. J.: Efficiency of the deposition mode ice nucleation on mineral dust particles, Atmos. Chem. Phys., 6, 3007-3021, doi:10.5194/acp-6-3007-2006, 2006.
Neale, R. B., and Coauthors: Description of the NCAR Community Atmosphere Model (CAM5.0). NCAR Tech. Rep. NCAR/TN-486+STR, 2010.

Nichman, L., Fuchs, C., Järvinen, E., Ignatius, K., Höppel, N. F., Dias, A., Heinritzi, M., Simon, M., Tröstl, J., Wagner, A. C., Wagner, R., Williamson, C., Yan, C., Connolly, P. J., Dorsey, J. R., Duplissy, J., Ehrhart, S., Frege, C., Gordon, H., Hoyle, C. R., Kristensen, T. B., Steiner, G., McPherson Donahue, N., Flagan, R., Gallagher, M. W., Kirkby, J., Möhler, O., Saathoff, H., Schnaiter, M., Stratmann, F., and Tomé, A.: Phase transition observations and discrimination of small cloud particles by light polarization in expansion chamber experiments, Atmos. Chem. Phys., 16, 3651-3664, doi:10.5194/acp-16-3651-2016, 2016.

Nicolet, M., Stetzer, O., Lüönd, F., Möhler, O., and Lohmann, U.: Single ice crystal measurements during nucleation experiments with the depolarization detector IODE, Atmos. Chem. Phys., 10, 313-325, doi:10.5194/acp-10-313-2010, 2010.

Niemand, M., Möhler, O., Vogel, B., Vogel, H., Hoose, C., Connolly, P., Klein, H., Bingemer, H., DeMott, P., Skrotzki, J. and Leisner, T.: A Particle-Surface-Area-Based Parameterization of Immersion Freezing on Desert Dust Particles, J. Atmos. Sci., 69(10), 3077-3092, doi:10.1175/jas-d-11-0249.1, 2012.

Olsen, K.: The clean development mechanism's contribution to sustainable development: a review of the literature, Climatic Change, 84(1), 59-73, doi:10.1007/s10584-007-9267-y, 2007.

Paris Agreement, United Nations, Paris, France, 2015.

Parzen, E., On Estimation of a Probability Density Function and Mode, Ann. Math. Stat., 33, 1065-1076, doi:10.1214/aoms/1177704472, 1962.

Peltier, R. E., Sullivan, A. P., Weber, R. J., Brock, C. A., Wollny, A. G., Holloway, J. S., de Gouw, J. A., and Warneke, C.: Fine aerosol bulk composition measured on WP-3D research aircraft in vicinity of the Northeastern United States - results from NEAQS, Atmos. Chem. Phys., 7, 3231-3247, doi:10.5194/acp-7-3231-2007, 2007.

Peters, G., Aamaas, B., Berntsen, T. and Fuglestvedt, J.: The integrated global temperature change potential (iGTP) and relationships between emission metrics, Environ. Res. Lett., 6(4), 044021, doi:10.1088/1748-9326/6/4/044021, 2011.

Petters, M. D., and Kreidenweis, S. M.: A single parameter representation of hygroscopic growth and cloud condensation nucleus activity, Atmos. Chem. Phys., 7, 1961-1971, 2007.

Prather, M.: Lifetimes of atmospheric species: Integrating environmental impacts, Geophys. Res. Lett., 29(22), 20-1-20-3, doi:10.1029/2002gl016299, 2002.

Prenni, A., Wise, M., Brooks, S. and Tolbert, M.: Ice nucleation in sulfuric acid and ammonium sulfate particles, Journal of Geophysical Research: Atmospheres, 106(D3), 3037-3044, doi:10.1029/2000jd900454, 2001.

Prenni, A. J., Petters, M. D., Faulhaber, A., Carrico, C. M., Ziemann, P. J., Kreidenweis, S. M., and DeMott, P. J.: Heterogeneous ice nucleation measurements of secondary organic aerosol generated from ozonolysis of alkenes, Geophys. Res. Lett., 36, D21303, doi:10.1029/2008GL036957, 2009.

Pruppacher, H. R. and Klett, J. D.: Microphysics of Clouds and Precipitation, Atmospheric and oceanographic sciences library, Kluwer Academic Publishers, Dordrecht, The Netherlands, 2nd ed., 1997.

Reff, A., Bhave, P. V., Simon, H., Pace, T. G., Pouliot, G. A., Mobley, J. D., and Houyoux, M.: Emissions Inventory of PM2.5 Trace Elements across the United States, Environ. Sci. Tech., 43, 5790-5796, doi:10.1021/es802930x, 2009.

Reilly, J., Paltsev, S., Monier, E., Chen, H., Sokolov, A., Huang, J., Ejaz, Q., Scott, J., Morris, J., and Schlosser, A.: Energy and Climate Outlook: Perspectives from 2015, MIT Joint Program on the Science and Policy of Global Change, Cambridge, MA, 2015.

Richardson, M., 2009: Making real time measurements of ice nuclei concentrations at upper tropospheric temperatures: Extending the capabilities of the continuous flow diffusion chamber, Dissertation thesis, 268 pp, Colorado State Univ., Fort Collins.

Roberts, G. C., and Nenes, A.: A continuous-flow streamwise thermal-gradient CCN chamber for atmospheric measurements, Aerosol Sci. Tech., 39, 206-221, doi: 10.1080/027868290913988, 2005.

Rogers, D. C.: Development of a continuous flow thermal gradient diffusion chamber for ice nucleation studies, Atmos. Res., 22, 149-181, doi:10.1016/0169-8095(88)90005-1, 1988.

Rogers D. C., DeMott P. J., Kreidenweis S. M., and Chen Y. L.: A continuous-flow diffusion chamber for airborne measurements of ice nuclei. J. Atmos. Ocean Tech. 18, 725-741, doi: 10.1175/1520-0426(2001)018<0725:ACFDCF>2.0.CO;2, 2001.

Rosenblatt, M.: Remarks on Some Nonparametric Estimates of a Density Function, Ann. Math. Stat., 27, 832-837, doi:10.1214/aoms/1177728190, 1956.

Saito, A., Murakami, M., and Tanaka, T.: Automated Continuous-Flow Thermal-Diffusion-Chamber Type Ice Nucleus Counter, SOLA, 7, 29-32, doi: 10.2151/sola.2011-008, 2011.

Salam, A., Lesins, G., and Lohmann, U.: Laboratory study of heterogeneous ice nucleation in deposition mode of montmorillonite mineral dust particles aged with ammonia, sulfur dioxide, and ozone at polluted atmospheric concentrations, Air Qual. Atmos. Health, 1, 135-142, 10.1007/ s11869-008-0019-6, 2008.

Seinfeld, J. H. and Pandis, S. N.: Atmospheric chemistry and physics: from air pollution to climate change, Wiley, Hoboken, N.J., 2nd ed., 2006.

Smith, K.: Acute Pulmonary and Systemic Effects of Inhaled Coal Fly Ash in Rats: Comparison to Ambient Environmental Particles, Toxicological Sciences, 93(2), 390-399, doi:10.1093/toxsci/kfl062, 2006.

Smith, R. D., Campbell, J. A., and Nielson, K. K.: CHARACTERIZATION AND FORMATION OF SUB-MICRON PARTICLES IN COAL-FIRED PLANTS, Atmos. Environ., 13, 607-617, doi:10.1016/0004-6981(79)90189-6, 1979.

Stetzer, O., Baschek, B., Lüönd, F., and Lohmann, U.: The Zurich Ice Nucleation Chamber (ZINC) - A new instrument to investigate atmospheric ice formation, Aerosol Sci. Technol., 42, 64-74, 10.1080/02786820701787944, 2008.

Stocker, T.F., Qin, D., Plattner, G.-K., Tignor, M., Allen, S.K., Boschung, J., Nauels, A., Xia, Y., Bex V., and Midgley, P.M. eds.: Climate Change 2013: The Physical Science Basis, Working Group I Contribution to the Fifth Assessment Report of the Intergovernmental Panel on Climate Change. Summary for Policymakers (IPCC, 2013), Cambridge, United Kingdom and New York, NY, USA, 2013.

Storelvmo, T., Hoose, C., and Eriksson, P.: Global modeling of mixed-phase clouds: The albedo and lifetime effects of aerosols, J. Geophys. Res., 116, D05207, doi:10.1029/2010JD014724, 2011.

Storelvmo, T., Kristjansson, J., Muri, H., Pfeffer, M., Barahona, D. and Nenes, A.: Cirrus Cloud Seeding has Potential to Cool climate, Geophys. Res. Lett., 40, 178-182, doi:10.1002/grl.50122, 2013.

Sutter, C. and Parreño, J.: Does the current Clean Development Mechanism (CDM) deliver its sustainable development claim? An analysis of officially registered CDM projects, Climatic Change, 84(1), 75-90, doi:10.1007/s10584-007-9269-9, 2007.

Tan, I. and Storelvmo, T.: Sensitivity Study on the Influence of Cloud Microphysical Parameters on Mixed-Phase Cloud Thermodynamic Phase Partitioning in CAM5, J. Atmos. Sci., 73(2), 709-728, doi:10.1175/jas-d-15-0152.1, 2016.

Tao, W.-K., Chen, J.-P., Li, Z., Wang, C., and Zhang, C.: Impact of aerosols on convective clouds and precipitation, Rev. Geophys., 50, RG2001, doi:10.1029/2011RG000369, 2012.

Thomson, E. S., Wilen, L. A., and Wettlaufer, J. S.: Light scattering from an isotropic layer between uniaxial crystals, Journal of Physics: Condensed Matter, 21, 195407 (10pp), doi: 10.1088/0953-8984/21/19/195407, 2009.

Thompson Reuters,: Web of Science, webofknowledge.com [online] Available from: https://www.webofknowledge.com/ (Accessed 15 June 2016), 2016.

Tishkova, V., Demirdjian, B., Ferry, D., and Johnson, M.: Neutron diffraction study of water freezing on aircraft engine combustor soot, Phys. Chem. Chem. Phys., 13, 20729-20735, 2011.

Tobo, Y., Prenni, A. J., DeMott, P. J., Huffman, J. A., McCluskey, C. S., Tian, G., Pöhlker, C., Pöschl, U., and Kreidenweis, S. M.: Biological aerosol particles as a key determinant of ice nuclei populations in a forest ecosystem, J. Geophys. Res.-Atmos., 118, 10100-10110, doi:10.1002/jgrd.50801, 2013.

Toon, O., Maring, H., Dibb, J., Ferrare, R., Jacob, D., Jensen, E., Luo, Z., Mace, G., Pan, L., Pfister, L., Rosenlof, K., Redemann, J., Reid, J., Singh, H., Thompson, A., Yokelson, R., Minnis, P., Chen, G., Jucks, K. and Pszenny, A.: Planning, implementation and scientific goals of the Studies of Emissions and Atmospheric Composition, Clouds and Climate Coupling by Regional Surveys (SEAC4RS) field mission, Journal of Geophysical Research: Atmospheres, doi:10.1002/2015jd024297, 2016.

Umo, N. S., Murray, B. J., Baeza-Romero, M. T., Jones, J. M., Lea-Langton, A. R., Malkin, T. L., O'Sullivan, D., Neve, L., Plane, J. M. C., and Williams, A.: Ice nucleation by combustion ash particles at conditions relevant to mixed-phase clouds, Atmos. Chem. Phys., 15, 5195-5210, doi:10.5194/acp-15-5195-2015, 2015.

Wang, B., Laskin, A., Roedel, T., Gilles, M., Moffet, R., Tivanski, A. and Knopf, D.: Heterogeneous ice nucleation and water uptake by field-collected atmospheric particles below 273 K, Journal of Geophysical Research: Atmospheres, 117(D21), doi:10.1029/2012jd017446, 2012.

Wara, M.: Measuring the Clean Development Mechanism's performance and potential. UCLA Law Rev., 55, 1759-1803, 2008.

Welti, A., Lüönd, F., Stetzer, O., and Lohmann, U.: Influence of particle size on the ice nucleating ability of mineral dusts, Atmos. Chem. Phys., 9, 6705-6715, doi:10.5194/acp-9-6705-2009, 2009.

Welti, A., Kanji, Z. A., Lüönd, F., Stetzer, O., Lohmann, U.: Exploring the Mechanisms of Ice Nucleation on Kaolinite: From Deposition Nucleation to Condensation Freezing, J. Atmos. Sci., 71, 16-36, doi: 10.1175/JAS-D-12-0252.1, 2014.

Wettlaufer, J. S., Dash, J. G., and Untersteiner, N., eds.: Ice Physics and the Natural Environment, vol. 56 of NATO ASI Series I, SPRINGER-VERLAG, Heidelberg, 1999.

Xie, S., Liu, X., Zhao, C., and Zhang, Y.: Sensitivity of CAM5-Simulated Arctic Clouds and Radiation to Ice Nucleation Parameterization, J. Climate, 26, 5981-5999, doi: 10.1175/JCLI-D-12-00517.1, 2013.

Xing, J., Pleim, J., Mathur, R., Pouliot, G., Hogrefe, C., Gan, C. M., and Wei, C.: Historical gaseous and primary aerosol emissions in the United States from 1990 to 2010, Atmos. Chem. Phys., 13, 7531-7549, doi:10.5194/acp-13-7531-2013, 2013.

Zawadowicz, M. A., Froyd, K. D., Murphy, D. M., and Cziczo, D. J.: Single Particle Mass Spectrometery (SPMS) of primary biological atmospheric aerosol particles, in prep, 2016.

Zimmermann, F., Ebert, M., Worringen, A., Schütz, L. and Weinbruch, S.: Environmental scanning electron microscopy (ESEM) as a new technique to determine the ice nucleation capability of individual atmospheric aerosol particles, Atmospheric Environment, 41(37), 8219-8227, doi:10.1016/j.atmosenv.2007.06.023, 2007.

Zimmermann, F., Weinbruch, S., Schütz, L., Hofmann, H., Ebert, M., Kandler, K., and Worringen, A.: Ice nucleation properties of the most abundant mineral dust phases, J. Geophys. Res., 113, D23204, doi:10.1029/2008JD010655, 2008.

Zobrist, B., Marcolli, C., Koop, T., Luo, B., Murphy, D., Lohmann, U., Zardini, A., Krieger, U., Corti, T., Cziczo, D., Fueglistaler, S., Hudson, P., Thomson, D. and Peter, T.: Oxalic acid as a heterogeneous ice nucleus in the upper troposphere and its indirect aerosol effect, Atmospheric Chemistry and Physics, 6(10), 3115-3129, doi:10.5194/acp-6-3115-2006, 2006.

Zobrist, B., Marcolli, C., Pedernera, D. A., and Koop, T.: Do atmospheric aerosols form glasses?, Atmos. Chem. Phys., 8, 5221-5244, doi:10.5194/acp-8-5221-2008, 2008.

Zuberi, B., Bertram, A., Cassa, C., Molina, L. and Molina, M.: Heterogeneous nucleation of ice in (NH4)2SO4-H2O particles with mineral dust immersions, Geophys. Res. Lett., 29(10), 142-1-142-4, doi:10.1029/2001gl014289, 2002.